DEVELOPMENT AND APPLICATION OF THE BOUNDARY SINGULARITY METHOD TO THE PROBLEMS OF HYDRODYNAMIC AND VISCOUS INTERACTION

A Dissertation

Presented to

The Graduate Faculty of The University of Akron

In Partial Fulfillment

of the Requirements for the Degree

Doctor of Philosophy

Maxim Mikhaylenko

December, 2015

DEVELOPMENT AND APPLICATION OF THE BOUNDARY SINGULARITY METHOD TO THE PROBLEMS OF HYDRODYNAMIC AND VISCOUS INTERACTION

Maxim Mikhaylenko

Dissertation

Approved:

_____
Advisor
Dr. Alex Povitsky

_____
Committee Member
Dr. Abhilash Chandy

_____
Committee Member
Dr. Nicholas G. Garafolo

_____
Committee Member
Dr. Darrell H. Reneker

_____
Committee Member
Dr. Gerald W. Young

_____
Committee Member
Dr. Ernian Pan

Accepted:

_____
Department Chair
Dr.Sergio Felicelli

_____
Interim Dean of the College
Dr. Rex Ramsier

_____
Interim Dean of the Graduate School
Dr. Chand Midha

_____
Date

ABSTRACT

In the past decades, the Finite Element (FEM) and the Boundary Singularity (BSM) Methods have proven their efficiency in solving electromagnetic and thermal problems. In fluid mechanics, BSM is a special case of BEM based on known fundamental solutions of the Stokes equation called Stokeslets. Potentially, the method has advantages over traditional finite-volume and finite-difference mesh-based methods for low-Reynolds number flows ($Re < 1$). Unlike Finite Difference and Finite Volume Methods, BSM only requires placement of fundamental solutions (singularities) at the boundaries of the considered geometry. However, in its' present state the use of BSM is hindered by solution oscillations and instabilities, due to high condition numbers of computational matrices and Stokeslet placement particularities that we attempted to resolve in the present research.

Application of proposed methods allows solving problems of a Stokes flow about ensembles of particles, "droplet – fiber" systems and flows in micro-channels using moderate number of singularities. Methods of geometric allocations of Stokeslets to achieve convergence with moderate number of Stokeslets are proposed, implemented and tested.

Optimized allocation of Stokeslets and collocation points is suggested for pairs and clusters of particles forming variable surface curvature including rapid variation of

curvature and presence of inflection points. In the present Dissertation local normal and combined Stokeslets allocation methods to solve Stokes flow problems for clusters of particles.

Another extension to the Stokeslet allocation schemes has been developed to evaluate Stokes flow field about single droplets and the "peanut-shape" clusters of merging droplets settling on relatively long cylindrical fibers. Three test problems are solved to demonstrate capability of BSM and proposed schemes of allocation of singularities.

Coupling of BSM and Finite Volume Methods was developed and applied to the solution of multiple scale quasi-steady problems of viscous deformation of 3-D droplets and 2-D tracks in a rectangular channel under air stream impinging at various angles.

At last, BSM simulation of a Stokes flow about micro-scale 3-D parabolic ripples and droplets was performed and the corresponding droplet viscous deformations were computed. The computational results are compared to the results of presented experimental visualization of viscous deformation of polydimethylsiloxane (PDMS) droplets and tracks in a scaled up replica of the air-liquid reaction zone. The mentioned simulations and experiments represent simplified model viscous deformation of molten mesophase pitch surface perturbation under the impinging hot air jet in the stagnation zone of the so-called Nanofiber-by-Gas Jet (NGJ) slit nozzle.

Keywords: Boundary singularity method, Stokes equations, microfluidics, Stokeslet, allocation of Stokeslets, matrix condition number, quasi-steady approach, viscous deformations, meltblowing, Nanofiber-by-Gas Jet, combined BSM and Finite Volume Method, production of submicron and nanofibers.

ACKNOWLEDGEMENTS

First of all, I would like to acknowledge my sincere gratitude to my adviser Dr. Alex Povitsky for his help and support during my Doctorate study and research program at The University of Akron. I appreciate and will always remember those numerous discussions of actual CFD problems we had. It is hard for me to overestimate importance of this experience for my future professional career.

I express my gratitude to Dr. Darrel H. Reneker and Dr. Barry Rosenbaum for an exceptional opportunity to participate in the NGJ research project, as well as for their invaluable advices and support in the experimental work and during our endless search of newer engineering solutions for challenging problems we faced.

I would like to thank my committee members, Dr. Abhilash Chandy, Dr. Gerald W. Young, Dr. Nicholas Garafolo and Dr. Ernian Pan for their helpful comments during my work on the dissertation. I appreciate invaluable knowledge I have gained attending their classes and being their assistant.

I am very grateful to Dr.Sergio Felicelli and Dr.Craig Menzemer for giving me opportunity to present my research at various conferences and workshops.

I want to say special “thank you” to Mike Swansiger whom I enjoyed working with on the NGJ project, who actively supported our interesting discussions and helped me with the experiments. I am grateful to him and his family for their continuous support, genuine kindness and understanding.

I would also like to thank my parents and my brother for their support.

Finally, I want to express my true love, respect and appreciation to my wife Anastasia who has been next to me all these years and supported me with her love and prayers. You and our son are always in my heart. The thoughts of you always inspired and helped me to overcome the toughest times of doubts and failures in the past. I would have not made it without your help.

TABLE OF CONTENTS

Page

LIST OF TABLES

Table Page

LIST OF FIGURES

CHAPTER I

INTRODUCTION

Present research is dedicated to: (i) the development of algorithms of placement of singularities for the Boundary Singularity Method and their comparison to the basic ones (Zhao, Povitsky [1,2,3,4,5], Gu et al [6], Chen, Gu [7]); (ii) determination of Stokes force, pressure and velocities of steady-state Stokes flows about merging particles and their clusters, "droplet – fiber" and other micro-scale multiphase flow systems and (iii) validation and application of the developed algorithms to important practical problems (fibrous filtration, particulate flows, multiphase flows and deformations of viscous media surfaces exposed to incoming high speed jet in which case Stokes flow is used to describe flow field in the vicinity of impact and droplet/track deposition line).

A Stokes flow model describes fluid moving at low Reynolds numbers ($Re < 1$), so that convection terms in the governing Navier-Stokes equations are neglected. Condition $Re < 1$ corresponds to either slow motion, or small characteristic length or large viscosity or combination of these factors.

1.1. Boundary element methods in practical micro- and nanoscale flow problems

There are numerous practical applications of Stokes flows that require computing of flow field such as micromechanical engineering (nano- and micro- filtration of multiphase mixtures [8, 9], penetration of fluid drops in porous media and their hydrodynamic interaction [10, 11, 12, 13]), biomedical engineering (precise medicine filtration and injection, vascular flows development of media capturing viruses, bacteria and cells, protein folding, vascular and capillary blood flow [14, 15]) and aerospace engineering (micro-channel heat exchangers development), to name a few. A distinct advantage of the Boundary Singularity Method (BSM) considered in this work and compared to finite-element (FEM) and finite-volume (FVM) methods is that BSM requires meshing only the boundary surface and not the entire 3-D domain. Therefore, BSM is easily applicable to flow about particles and their pairs and clusters of arbitrarily and changing shape.

1.2. Method of Fundamental Solutions and allocation of singularities review

Being one of the Boundary Element Methods (BEM) [10, 16], Method of Fundamental Solution (MFS) (also known and named hereinafter as the Boundary Singularity Method (BSM)) has demonstrated good accuracy using moderate number of fundamental solutions, so-called Stokeslets, at the boundary for Stokes flows about spherical particles [1-4, 9, 17]. The physical meaning of Stokeslets is a reaction on a unit

point force applied in a particular point at a surface. Then the sum of Stokeslets represents a total drag about whole surface. Most of BEM are based on the integral representations of governing equations and requiring a continuous surface distribution of singularities and the computation of the singular single-layer and double-layer integrals. Unlike those BEM, BSM involves only a point-wise distribution of singularities and thus simplifies the computer implementation and decreases the cost of computations.

The authors of the papers cited above obtained optimal allocation of singularities primarily for spherical particles. The problem with BSM method is appearance of near-singular matrices with large condition number (the ratio of maximum-to-minimum eigenvalues) in cases when either Stokeslets are located too close to observation points or Stokeslets are located too close to each other [4]. Therefore Stokeslets can neither coincide with collocation points nor placed near the geometric center of spherical particle. The optimal radius of spherical surface at which Stokeslets are located has been determined in prior studies as a fraction of radius of spherical particle.

Prior MFS studies are focused on techniques to extend its applicability, to reduce number of singularities required to achieve convergence and to avoid near-singular matrices. The developed approaches include slender-body approach [11, 12, 18, 19, 20, 21], method of images [22, 23, 24, 25, 26, 27], method of regularized Stokeslets [28, 29, 30, 31], and method of allocation of Stokeslets outside of computational domain (also known as method of submerged Stokeslets [1-3, 8, 17, 32]). In the current study, the meethod of submerged Stokeslets has been extended to particles with variable curvature radii associated with geometric properties of fused particles.

1.2.1 Slender-body approach

One of techniques allocating MFS singularities is based on slender-body approach [12, 18 and 19]. The necessary condition for validity of this approach is that one dimension (size of body) should be much larger than other dimensions ($\epsilon = \frac{l}{b} \leq 0.005$), where l is a body length and b is the maximum characteristic length in other directions [20]. In frame of the slender body approach, Stokeslets are placed along the axis of a slender body. This method has been adopted for basic shapes like cylinders, helices, spheroids and other axisymmetric bodies (Clarke et al. [11], Cortez and Nicholas [21], Nitsche and Parthasarathi [30]), complex flagella swimming models, closed filaments and combined bodies (Johnson and Brokaw [20], Cortez and Nicholas [21]), flexible fibers and filaments (Tornberg and Shelley [12]), and various slender axisymmetric particles (Batchelor [18]), to name a few. The slender-body approach separates collocation points and singularities and thus offers straightforward approach to allocation of singularities. However, this technique is limited to axisymmetric slender bodies and is not applicable to pairs and clusters of particles where the above slenderness condition is not satisfied.

1.2.2 Method of Regularized Stokeslets

To remove singularities associated with close proximity of Stokeslets and collocation points, the method of regularized Stokeslets (MRS) is used for Stokes flow problems

including flow about translating spheres (Cortez et al. [29]) and more complex shapes like cilia- and flagella- driven flows (Lobaton and Bayen [31] and Smith et al. [33]). MRS has been introduced by Cortez et al. [29, 34] and has been updated and improved by Lin [35] and Gonzalez [36]. MRS is based on exact solution of Stokes equations for velocity in response to local force expressed by regularized delta functions. The Method of Regularized Stokeslets becomes another version of MFS specifically focused on elimination of singularities [16]. In MRS the Green's function singularity is removed [37] by distortion of original Green's function (Stokeslet).

According to Zhao [5], BSM with Stokeslets cause significant pressure oscillations in the obtained numerical solution, when the Stokeslets and collocation points are located at the same spherical surface. Zhao emphasizes that regularized Stokeslets help avoiding singular solution at the boundary surface and remove pressure oscillations, making it one of the perspective methods that will be used to solve problems mentioned above. This statement will also to be verified in the present work.

1.2.3 Method of Submerged Stokeslets

In the current study, the focus was made on different schemes of optimal placement of Stokeslets distributed under considered boundary. The proposed schemes are to produce accurate Stokes flow solution using moderate number of Stokeslets. Method of Submerged Stokeslets does not create singular matrix even if two particles collide or close to each other. Present research proposes novel schemes of Stokeslets'

allocation to particles of arbitrarily shapes formed as a result of merging of two or more spherical particles, particles interacting with fibers, as well as viscous and liquid droplets deformed in the flow. The goal is to achieve solution convergence using moderate number of Stokeslets for Stokes flow about generic shapes of ensembles of particles and other surfaces in hydrodynamic interaction. For liquid or gas droplets or solid particles that are frozen liquid droplets, the spherical convex shape has minimum surface for a given volume [38]. While single particles typically have convex surface, their newly formed pairs and clusters have combined convex and concave surfaces separated by inflexion points (see Figures 2-3 and 2-6). The convex spherical part of surface is inherited from single spherical particles, while the concave part of surface is formed where particles are merged. The proposed combined approach to allocation of Stokeslets accounts for intermittent convex and concave parts of surface of cluster or pair of particles.

1.2.4 Basic Stokeslet allocation methods in BSM

In existing allocation methods, Stokeslets are placed at submerged surface Γ_S similar in shape to physical particle surface Γ but of smaller geometric scale (see Chapter II). There are two Stokeslet allocation techniques widely used in frame of the method of submerged Stokeslets, namely, similar shape uniform and non-uniform methods (Zhao and Povitsky [1-5], Young, Chen [32,39], and Aboelkassem and Staples [8]). In frame of the uniform allocation scheme the surface Γ_S is divided to elementary surface cells of equal area and

Stokeslets are placed at the centers of these cells. A non-uniform Stokeslet allocation scheme assumes equal number of Stokeslets at each lateral cross-section, which leads to more dense concentration of Stokeslets in the cross-sections with a smaller radius such as necks and poles.

Young et al. [40, 41 and 42] applied BSM to 2-D and 3-D problems of Stokes flow about spheres and inside cavities with various shape forms. Their numerical experiments revealed range of distances between Stokeslets and collocation points that produced acceptable convergence. Thus, for a Stokes flow about sphere they chose normalized Stokeslets allocation depth of $D \approx 0.167$ under the spherical surface of the unity radius and the number of Stokeslets varied from 20 to 40 Stokeslets for the flows in circular cavity to more than 266 Stokeslets for the flow about complex shape. Kolodziej and Klekiel [43] used MFS to obtain parameters of Stokes flows through ducts of arbitrarily cross-section. For a duct with square cross-section, they placed Stokeslets outside of flow domain at a distance of 10% of the square length.

Many studies adopt uniform Stokeslet allocation scheme including Zhao and Povitsky [1-5] for Stokes flows about sets of spheres, Young et al. [44, 39, 45, 46, 47] for a lid driven cavity flow, Aboelkassem and Staples [8] for Stokes flows in curved ducts and Young et al. [32] for Stokes flow inside free-form cavities and about spherical particles. Zhao and Povitsky [1-5] applied uniform Stokeslet distribution scheme for a Stokes flow past a sphere and about ensembles of spherical particles for no-slip and partial-slip boundary conditions. They have determined that the optimal Stokeslet allocation is at spherical surface Γ_S with its normalized radius $\overline{a} = 0.7$ that corresponds to

Stokeslets' allocation depth D = 0.3 (Figure 2-1). This submergence depth has been used for both uniform and non-uniform Stokeslet allocation schemes.

Apart of the solution of a Stokes flow problems, allocation of boundary singularities is discussed by Goldberg and Cheng [48] and applied to the heat transfer problem inside two merging spheres. They placed singularities over an imaginary sphere of a greater radius than the boundary surface. Tsai and Young [17] applied non-uniform Stokeslet allocation scheme to a peanut-shaped model solving 3-D Helmholtz problems.

Tsai et al. [49] used the non-uniform Stokeslet allocation scheme to place Stokeslets (referred to as source points) to solve unsteady problem of motion of peanut-shaped particle in a viscous media. They used a combined temporal-spatial discretization scheme, i.e. they placed source points at the same spatial locations as collocation points but at different time levels that allows for the non-zero distance between Stokeslets and collocation points.

1.3 BSM application to particulate flows and fibrous filtration problems

Determination of the flow parameters about ensembles of micro-scale droplets during their hydrodynamic interaction, as well as with cylindrical fibers and study of the drag force depending on orientation of “droplet - fiber” systems, is one of the core problems considered in present research.

For Stokes flows about pairs and clusters of particles with convex and concave surfaces, BSM still has stability constraints and requirements for substantial computational resources due to a large condition number of computational matrix associated with BSM (see Chapter II). The number of Stokeslets affects condition number of a computational matrix and, consequently, the convergence rate. If the number of Stokeslets and collocation points increases, the computational matrix may become ill-posed because the corresponding vectors connecting neighboring Stokeslets and collocation points become near-parallel [3]. This issue becomes even more critical in the vicinity of inflexion points for complex convex-concave shapes.

This calls for allocation of Stokeslets at more broadly defined surfaces Γ_S that are not necessarily geometrically similar to particle's physical surface Γ, at which collocation points are placed (Figure 2-1). The study is aiming at development of Stokeslets-allocating methodology applicable to arbitrarily shaped bodies typical for particles' interaction problems in order to reduce the size of linear system and to obtain acceptable accuracy of the solution using moderate number of Stokeslets. This allows for significant savings in computational time of the BSM applied to a Stokes flow problems where precise determination of Stokes force and other flow parameters are critical. If successful, the proposed schemes can be applied to arbitrary-shaped surfaces modeling freeform droplets and particles. The problem of finding Stokes force, velocity and stresses for such surfaces with known empirical formulas is cumbersome as soon as finding volume of an arbitrary-shaped surface is quite complicated [50], especially for ensembles of interacting surfaces.

1.4 BSM application to a “gas – liquid” interaction problem in the NGJ process

Besides fibrous filtration and hydrodynamic interaction of particles, the practical applicability of BSM is demonstrated through solving of the microfluidics problems typical for the Nanofiber-by-Gas Jet (NGJ) process. NGJ is a nanofiber production process that was developed and patented at The University of Akron back in 2002. Similar to meltblowing [51,52], the physical principle of the process is aerodynamic interaction of pre-heated gas jet with a liquefied polymer surface. However, meltblowing implies injection of the polymer in strands where at the outlet it is coaxially surrounded and attenuated by gas jet. Instead, the NGJ process in rectangular nozzle is based on development of the disturbances on a free pitch surface under high temperature gas jet and fiber-forming stretching by means of drag force exerted at the surface of molten polymer surface ripples (Figure 1-1).

Although NGJ method has been proven efficient in producing micro- and nanofibers from various polymers, interaction between processes taking place is quite complicated to develop the computer model for design optimization. The physics of the process incorporates multiphase turbulent flow with simultaneous effect of air-pitch-solid interaction, turbulent flow in the channel, rheological liquid flow with non-Newtonian properties relating viscosity, shear stress and dynamic tensile modulus.

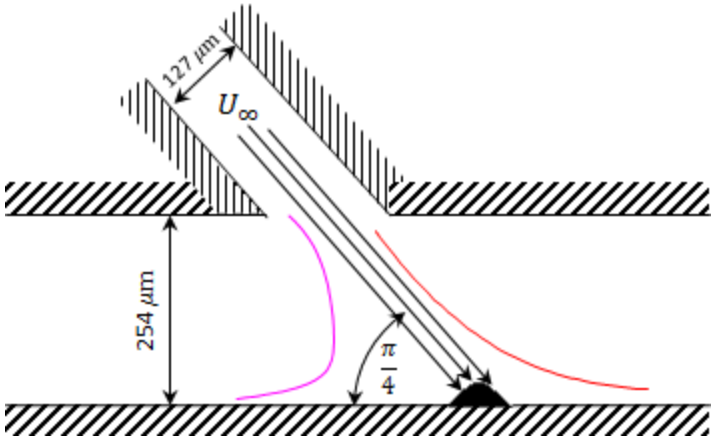

Figure 1-1 Schematic of the air flow impinging the molten pitch ripple.

Because of the micro-scale nozzle dimensions and intense nanofiber and molten pitch particles scattering, NGJ and meltblowing processes are quite complicated for visualization and PIV-imaging inside (Figure 1-2). Meanwhile, there is a demand [52] in understanding of physics of multiphase flows occurring in the contact zone, where high-velocity air jet contacts with molten resin, mesophase pitch in particular.

As shown at Figure 1-1, the angle at which air jet impinges the lower channel wall is $\beta = 45^o$. This corresponds to experimental nozzle air jet channel assembly. However, numerous experimental nozzle runs have shown that specified air jet channel inclination is not optimal, because it produces contaminating pitch particles besides fiber due to aero-acoustic effects inside. It was also shown experimentally using concentric nozzle that grazing air jet contacting with disturbed pitch film at smaller angles of impingement has higher nanofiber production rate than "loosening" jet at larger angles that causes "spitting out" pitch particles. Therefore, present study includes numerical simulation and experimental research of viscous deformation effects for the pitch surface perturbation in a low-Reynolds flow region for different β.

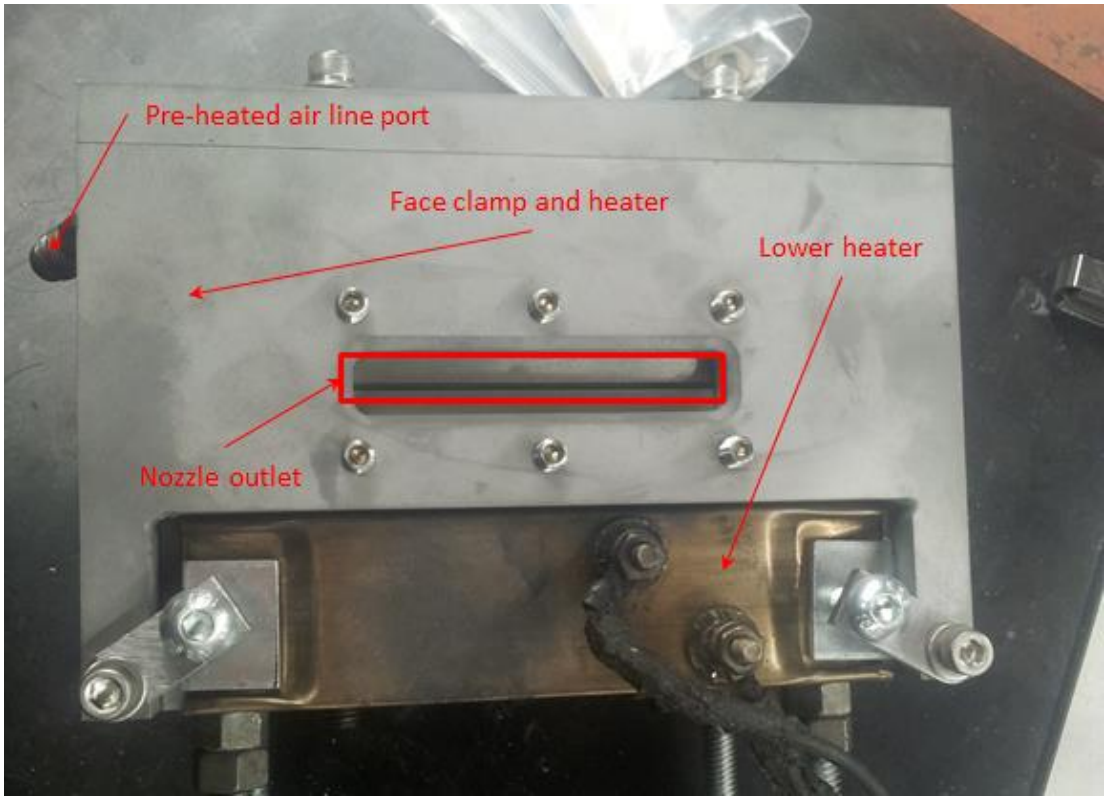

Figure 1-2 Photograph of the rectangular NGJ nozzle (details are omitted due as an intellectual property of the UARF and the College of Polymer Science and Polymer Engineering)

Recent experiments on NGJ development were conducted with participation of author of the present work at Sydney L. Olson Research Center of the University of Akron under advisory of Prof. Darrell H.Reneker (College of Polymer Science and Polymer Engineering) and management of Dr. Barry Rosenbaum (UARF). The experiments with the new NGJ nozzle (Figure 1-2) operated with the GraphTech carbon mesophase pitch show importance of the balance between air flow and melted pitch flow characteristics. It is predicted that at smaller angles between impinging air stream and the pitch flow direction, the process is more sustainable. That is pitch pressure tends to grow at larger angles (Figure 1-1), and the volume fraction of fiber with respect to

contaminating pitch particles occasionally produced together with fiber, is lower. The appropriate process modeling, numerical simulations of the flow of impinging air jet at the disturbed pitch surface in stagnation region at different angles and determination of flowfield, stress components the flow are necessary to predict deformations of viscous pitch nanofiber embryos. In present PhD dissertation, the effect of impinging air jet orientation angle versus deformation of a liquid pitch droplet/track in a rectangular channel is studied.

1.5 Objectives of the present work

The present work is aimed at improvement of computational efficiency and increasing accuracy of BSM in terms of drag (Stokes) force and velocity solving Stokes flow problems for convex-concave 3-D models of merging particles, bubbles and droplets, their interaction with the cylindrical fibers, as well as for the problems of viscous liquid surface deformations. For this purpose, advanced schemes of allocation of Stokeslets with their comparison to a commonly used allocation schemes are developed. The proposed schemes are applied to practical problems of microfluidics with faster and more accurate prediction of Stokes flow parameters for:

a) particles and droplets of arbitrary shape (Chapter II);
b) hydrodynamic interaction, droplets merging into pairs and clusters (Chapter II);
c) hydrodynamic interaction of droplets settling on fibers (Chapter III).

The author is also attempting to obtain computationally efficient and accurate prediction of multiple-scale fluid flow about liquid surfaces in a microscale channel using FV – BSM approach. The algorithm of the problem scale transition with the domain overlap for respective FV and BSM application will be discussed in Chapter IV.

1.6 Organization of the present work

The dissertation is composed as follows. Chapter II formulates BSM for a Stokes flow problem and validates BSM methodology using known solution for the flow about pairs and clusters of merging particles. The proposed Stokeslet allocation schemes for arbitrarily-shaped bodies are introduced and applied to Cassinian and modified Cassinian ovals introduced as representatives of pairs and clusters of particles.

Chapter III describes another alternative Stokeslet allocation scheme, which was developed particularly for the problems of Stokes flows about “droplet - fiber” systems and the resulting velocity vector field and the drag force evolution depending on system orientation with respect to a flow direction are presented.

Chapter IV introduces experimental apparatus for study of viscous deformation of droplets and tracks in a rectangular channel. The scale up of real NGJ process nozzle reaction zone justification is discussed and deformation visualization results are presented in order to compare them with subsequent numerical simulation for the respective air flow orientation angles.

There are very few examples of coupling of Finite Volume and Boundary Element Methods for multiscale problems. Kassab et al in [53] and Li and Kassab in [54] used BEM/FVM coupling to address the problem of heat transfer in 3-D cooled film turbine blades. In Chapter V, a multiple scale FVM-BSM quasi-steady approach is proposed for simulation of Stokes flow about deformable surfaces of viscous 2-D semi-circular and parabolic tracks is validated and used. In this Chapter surface stresses and resulting viscous deformations of the liquid surface modeling PDMS and mesophase pitch ripple under impinging air uniform crossflow in vicinity of stagnation line inside NGJ nozzle are predicted. First, validation of MRS has been performed applying it to the test case problem of a Stokes flow in a rectangular channel with semi-circle protrusion. Pressure and shear stress along the channel bottom wall with protrusion are compared to the results obtained by Cortez [34] and the ones computed with the FV method. Then MRS is incorporated into a BSM code to solve iterative quasi-steady problem of viscous deformations of the surface in a Stokes flow region. The initial velocity vector field at the boundaries of the considered $1056\mu m \times 256\mu m$ fluid flow domain is imported from the resulting velocity vector field for the whole channel obtained in ANSYS Fluent.

Chapter VI represents 3-D extension of Chapter V and discusses solution of multiple scale problem of viscous deformation of 3-D parabolic droplet under air jet discharged into the channel at orientation angles equal to 30 and 45 degrees.

Finally, conclusions and directions of the proposed future research are presented in Chapter VII.

CHAPTER II

DEVELOPMENT OF THE BOUNDARY SINGULARITY METHOD FOR THE PROBLEMS OF HYDRODYNAMIC INTERACTION BETWEEN PARTICLES AND THEIR CLUSTERS

2.1 Formulation of the problem and common Stokeslet allocation schemes

The model of a viscous flow with *Re<1* is represented by the system of simplified vector momentum equation (Stokes equations) and a continuity equation, which can be written as follows:

$$\begin{cases} \nabla \cdot \vec{u} = 0 \\ -\nabla p + \mu \nabla^2 \vec{u} = 0, \end{cases} \tag{2-1}$$

where $\vec{u}(x,y,z)$ and $p(x,y,z)$ are the 3-D velocity vector and pressure respectively. The general solution of above system of equations for velocity can be presented using sums of Green's functions corresponding to *N* elementary flow singularities (Stokeslets):

$$u_j{}^{(k)} = \frac{1}{8\pi\mu} \sum_{i=1}^{N} \left(\frac{F_i{}^{(k)}}{|\widetilde{r_{ij}}|} + \frac{F_i{}^{(m)} \widetilde{r_{ij}}^{(k)} \widetilde{r_{ij}}^{(m)}}{|\widetilde{r_{ij}}|^3} \right) \tag{2-2}$$

where $\widetilde{r_{ij}} = \vec{r_j} - \vec{a_i}$ are vectors connecting collocation points and Stokeslets. Here subscripts *j* are associated with collocation points, and subscripts *i* denote Stokeslets, index *k=1,2,3* denote components of velocity. Einstein summation rule is applied to

index m=1,2,3 that denote components of Stokeslets vectors. The above system can be expressed in the matrix form:

$$U = M\vec{F} \tag{2-3}$$

where $\vec{U}$ is a velocity vector at collocation points, $\vec{F}$ is a Stokes force vector with $3N$ unknowns, and M is the $3N \times 3N$ matrix of system (2-2). The Stokeslets' strength vector is $\vec{F} = \{{F_1}^1, {F_1}^2, {F_1}^3, \dots, {F_N}^1, {F_N}^2, {F_N}^3\}$. To reduce round-off errors, distances $\widetilde{r_{ij}}$ in (2-2) are normalized by characteristic radius that is defined as the ratio of a particle volume to its surface area and is equal to radius of sphere for a spherical particle.

For convenience of posting boundary conditions, a Stokes flow problem is considered for a particle that moves with the velocity U_∞ through a stationary fluid. For no-slip boundary conditions, the velocity components are equal to U_∞ at rigid boundaries, where collocation points are located while far-field boundary conditions are omitted. Numerical solution of above linear system (2-3) was performed using the MATLAB backslash linear algebraic operation, *F=U\M*. For a square matrix (2-3) a general triangular factorization is computed by Gaussian elimination with partial pivoting implemented in MATLAB's backslash operator [55]. In the future research the system (2-3) can be replaced with its simplified version that nulls small contributions of Stokeslets and collocation points located at a distance from each other (see Equation (2-2)). This would allow using more efficient algorithms available in MATLAB's backslash operator for banded linear systems [55].

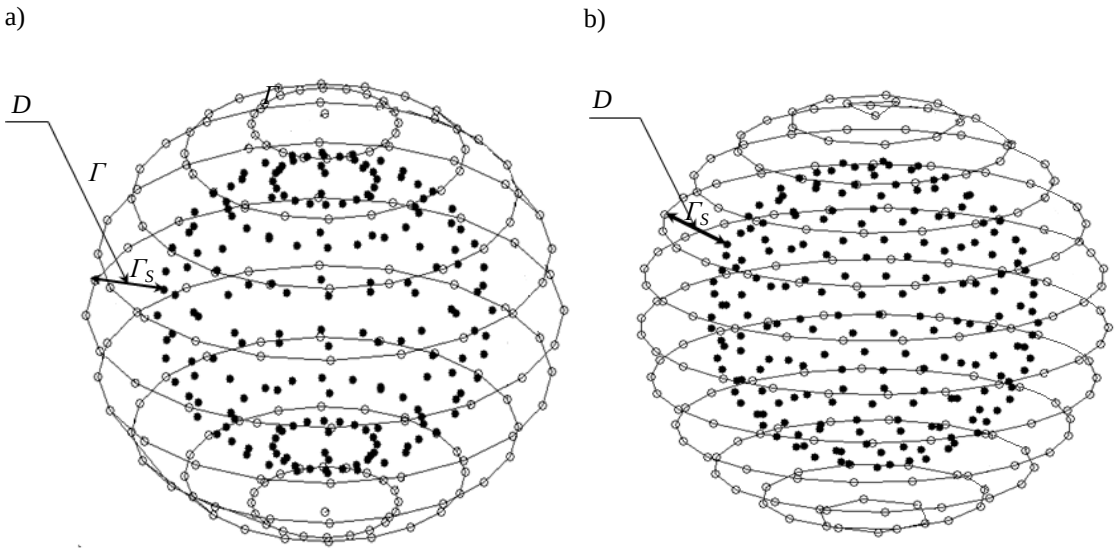

Figure 2-1 Stokeslet allocation schemes for Stokes flow about spherical particle: a) non-uniform (196 Stokeslets) and b) uniform (194 Stokeslets). Particle has surface Γ; Stokeslets are allocated at spherical surface Γ_S.

After system (2-3) is solved, velocity can be determined at any point of the flow field using the right-hand side of (2-2) with values of radius-vectors corresponding to a point location. The resulting pressure is computed by:

$$p_j = \frac{1}{4\pi}\sum_{i=1}^{N}\frac{F_i^{(m)}\cdot\widetilde{r_{ij}}^{(m)}}{|\widetilde{r_{ij}}|^3} \tag{2-4}$$

Validation of BSM matrix equation (2-3) is conducted using the flow about spherical particle, for which analytical solution is known [56] and presented in Appendix A.

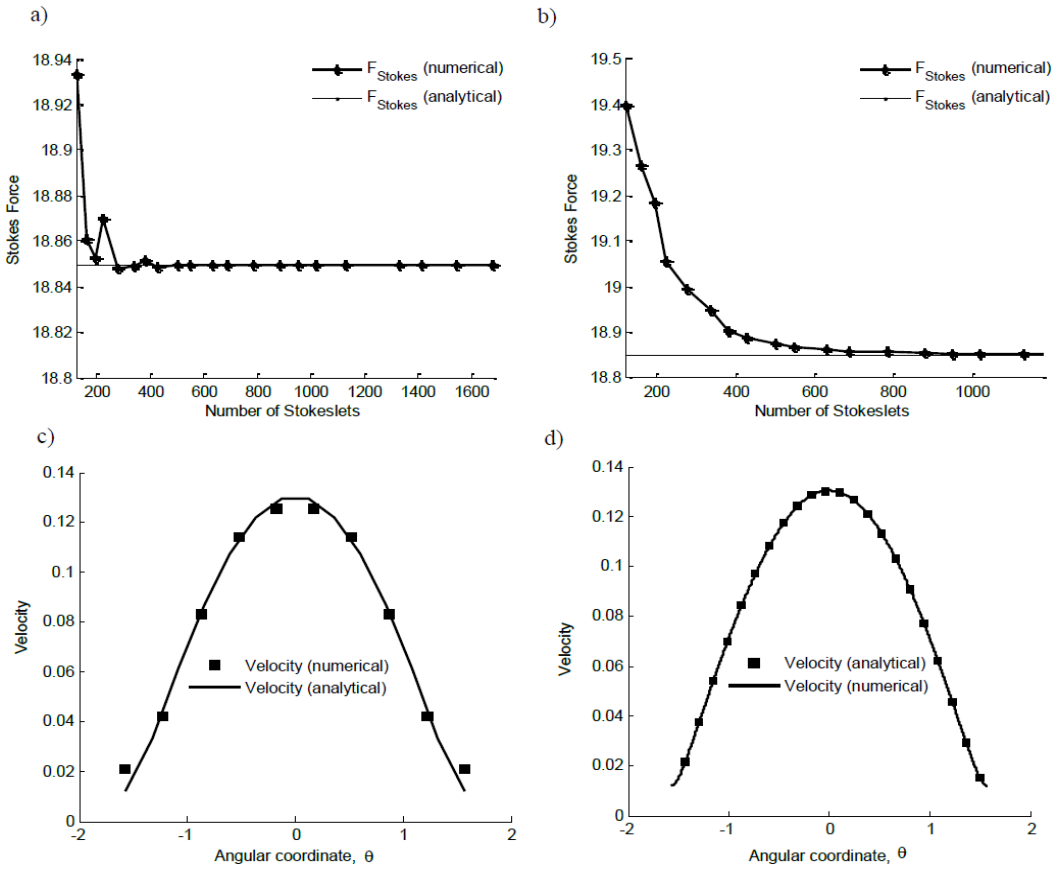

Figure 2-2 Validation of numerical solution for Stokes flow about sphere: (a-b) convergence in terms of Stokes force a) non-uniform Stokeslet allocation scheme, b) uniform scheme; flow velocity magnitude at distance *0.1R* from the sphere surface: c) non-uniform Stokeslet allocation scheme (324 Stokeslets) and d) uniform scheme (339 Stokeslets).

Compared variables include Stokes force, velocity field and pressure at the particle surface. The method of submerged Stokeslets [1-3, 43, 48, 40, 57, 58] was applied to allocate Stokeslets inside the sphere (Figure 2-1) to avoid ill-conditioned matrix *M*. The depth of Stokeslet allocation is a difference between radius of the physical particle surface Γ, *R*, and radius of spherical surface Γ_S, *a*, at which Stokeslets are located. The normalized Stokeslet submergence depth, *D*, is defined as follows:

$$D = \frac{R-a}{R} = 1 - \overline{a}, \tag{2-5}$$

To evaluate convergence to analytical solution in terms of Stokes force (see Equation (A-1) in Appendix A) and tangential velocity (A-3), numerical results (Figure 2-2) are obtained for non-uniform and uniform Stokeslet distribution schemes.

Non-uniform scheme (Figure 2-2a) has an equal number of Stokeslets (and collocation points) at each cross-section of the sphere. Non-uniform distribution of Stokeslets gives satisfactory convergence (0.1% of the absolute error in terms of Stokes force) using 625 Stokeslets, while uniform distribution scheme (Figure 2-2b) gives the same accuracy using 262 Stokeslets.

Spherical particle is a convenient geometric shape to validate BSM using exact analytical solution and known methods of allocation of Stokeslets. However, for arbitrarily shaped particles, one has to account for the variable radius of curvature and the presence of inflection points to allocate Stokeslets in an optimal way. In the next sections it will be shown that Stokeslet allocation at submerged similar shape surface Γ_S can be replaced by more efficient local normal and combined schemes for Stokes flow problems about arbitrarily shaped particles.

2.2 Proposed Stokeslet allocation schemes

Proposed schemes of Stokeslets allocation based on geometric features of arbitrary-shaped bodies are introduced in this section. The suggested advanced allocation

schemes are designated to fend off solution instabilities for the regions near inflection points of convex – concave shapes and achieve faster Stokes force and velocity convergence.

2.2.1 Local normal Stokeslet allocation scheme

In a general case of asymmetrical arbitrarily shaped particle, the Stokeslet allocation algorithm at local normal lines (Figure 2-3a) places Stokeslets at surface formed by points S belonging to segments of lines locally normal to the surface and connecting the collocation points $(A_1, A_2, \dots, A_N)$ with the dividing line $(B_1, B_2, \dots, B_N)$. The dividing line splits the particle's axial cross-section into two areas of equal size. For an arbitrarily-shaped body this reference dividing line is curvilinear (see Figure 2-3a), while for an axisymmetric particle this line coincides with its symmetry axis.

Local normal lines are passing through the centers $(O_1, O_2, \dots, O_N)$ of the circles tangent to particle surface, whose radii are the local radii of curvature of the surface. The surface Γ_S is formed by points $(S_1, S_2, \dots, S_N)$ in such a way that:

$$D = \frac{A_1S_1}{A_1B_1} = \frac{A_2S_2}{A_2B_2} = \cdots = \frac{A_NS_N}{A_NB_N} = const. \tag{2-6}$$

Using above proportion, the normalized distance from a Stokeslet to the surface along the radius of curvature remains the same for all Stokeslets located at Γ_S. The local distance from the particle surface to the centerline along the local radius of curvature is used for scaling. Note that the local radius of curvature might not be an appropriate scale if a point

A_2 (see Figure 2-3a and Figure 2-3c) is near-inflexion point, where the curvature radius tends to infinity.

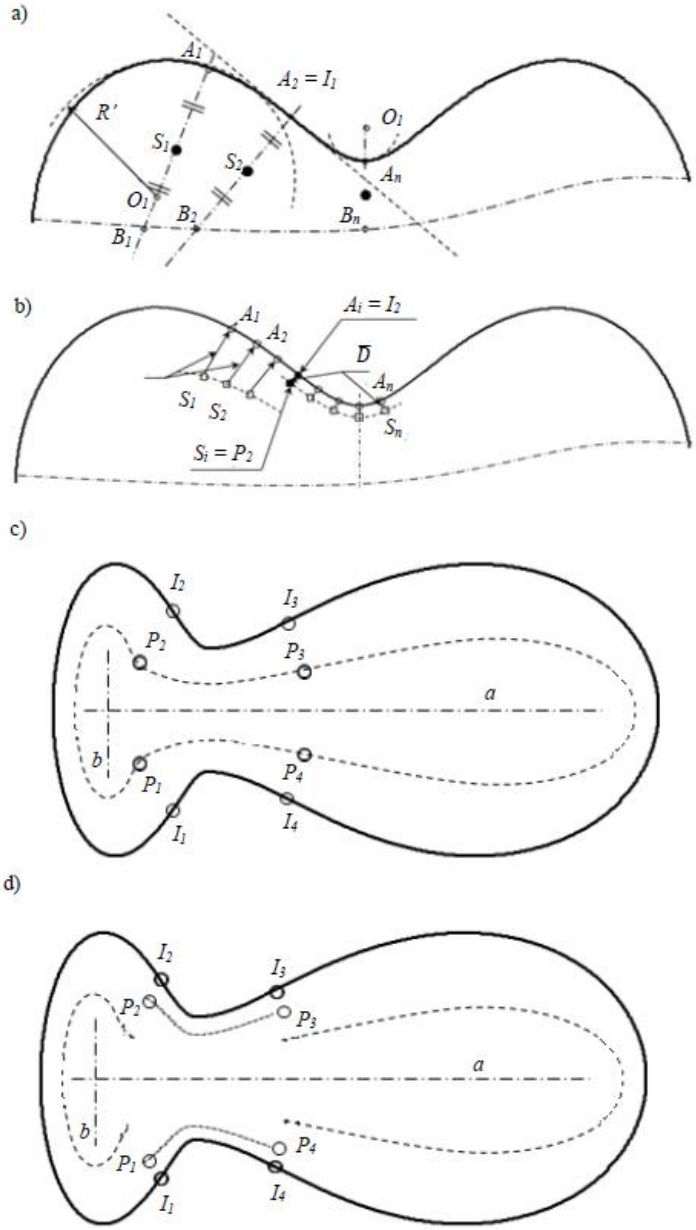

Figure 2-3 Proposed Stokeslets' allocation schemes for 3-D arbitrarily shaped particles: a) local normal scheme, b) locus of images of inflection points P1,..,P4 obtained using local normal scheme, c) combined Stokeslets' allocation scheme, and d) change in location of Stokeslets near inflection points using combined allocation scheme.

Using this method, Stokeslets are located between points A and B (as opposed to centers of curvature, *O*) to ensure that they are submerged under the surface. For example, point O_n (Figure 2-3a) is located outside the particle in the flowfield because of concave local property of the surface, that would create a singularity point in the flowfield if a Stokeslet is placed at point O_n. In frame of BSM, the Stokeslets should be allocated outside the flowfield. After surface Γ_S for allocation of Stokeslets is formed as described above, Stokeslets are distributed at the Γ_S uniformly.

Figure 2-3b shows the 2-D longitudinal section of an arbitrarily shaped particle and location of Stokeslets (dashed line) at a relative distance of $D = 0.5$, submerged under the surface. Here $I_1, .., I_4$ are inflexion points and $P_1, \dots, P_4$ are corresponding points at Stokeslets' allocation surface. Using the local normal method, Stokeslets are located at a flatter surface compared to the original shape (compare dashed and solid curves in Figure 2-3b).

For an arbitrarily concave-convex particle, the application of the local normal method along one axis might lead to self-intersecting Stokeslets' allocation surface, that place Stokeslets at a close proximity to each other. It is recommended to divide the body in sections separated by the line passing through the inflexion points (line $\overline{P_1 P_2}$ formed by inflexion points, see Figure 2-3b) and apply the local normal scheme for each section using the longest possible reference dividing line (for example, lines *a* and *b* in Figure 2-3b and d).

2.2.2 Combined Stokeslet allocation scheme

The main obstacle of application of BSM to merging particles is its' numerical instability caused by the presence of the inflexion points and their adjacent areas with large curvature radii. Proposed combined Stokeslet allocation scheme (Figure 2-3c) achieves convergence with fewer number of Stokeslets and smaller condition number of the BSM computational matrix. It uses local normal scheme at convex areas whereas a different Stokeslets allocation scheme is used in concave regions to ensure superior solution convergence caused by reduced matrix condition number. For concave areas and inflexion points the similar shape uniform Stokeslets' allocation scheme is adopted. For simplicity, switching between local normal and similar shape allocation schemes is applied exactly at inflection points; more gradual switching will be investigated in the future research.

Algorithms of Stokeslets' allocation pass through surface collocation points $A_1,\ldots,A_n$ (Figure 2-3a-c) and find corresponding locations of Stokeslets by the Equation (2-6) with needed corrections as outlined in this section. Particular optimal values of submergence depth, BSM matrix condition numbers and needed number of Stokeslets for the proposed methods are presented in Tables 2-1 and 2-2 and discussed in Section 2.3 after representative particles shapes are introduced in the next Section.

2.3 Representative shapes of merging particles

In this Section, a Cassini oval (also known as Cassinian) and its variants are introduced as typical representative shapes of merging particles, and applications of proposed Stokeslet allocation methods are demonstrated for these shapes.

2.3.1 Peanut-shaped Cassinian oval

As an example, peanut-shaped merging particles model is described by Cassini oval in [17,49,59]. Cassinian ovals are used for modeling of interaction of two viscous particles or bubbles as an extension of modeling of the spherical particles motion at pre-merging state [1, 3, 28, 60, 61].

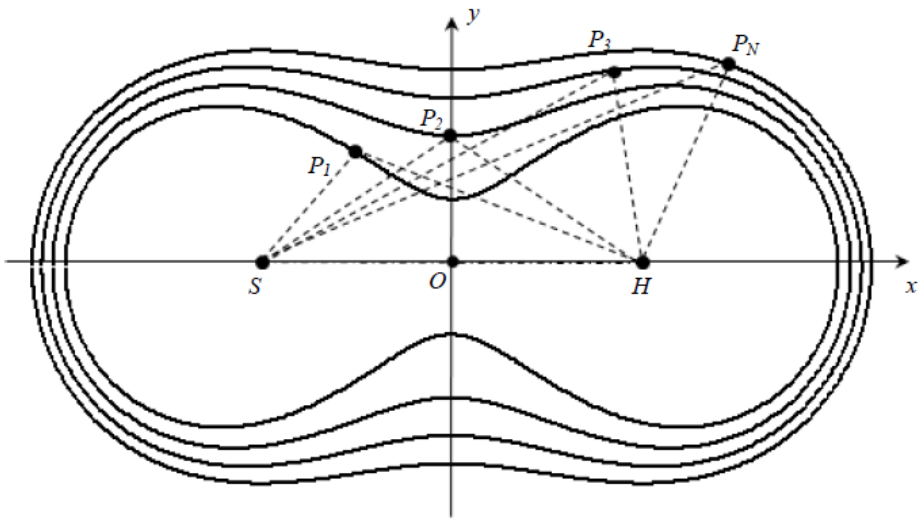

Figure 2-4 Set-up of Cassini (Cassinian) ovals.

Cassinian oval [62, 63] is a quadratic curve (see Figure 2-4), which is defined as a family of points satisfying condition (2-7).

$$SP_1 \cdot HP_1 = SP_2 . HP_2 = \cdots = SP_N \cdot HP_N = const \tag{2-7}$$

To satisfy (2-7), points P_i having coordinates (x, y) are located in such a way that $((x - c)^2 + y^2) \cdot ((x + c)^2 + y^2) = d^4$, where values of coefficients d and c define the particular shape of the oval:

$$r(\theta) = c\sqrt{cos2\theta \pm \sqrt{\left(\frac{d}{c}\right)^4 - sin^2 2\theta}},\ 0 \le \theta \le 2\pi$$
$$x(r,\theta) = r(\theta)\cos(\theta), \quad y(r,\theta) = r(\theta)\sin(\theta), \tag{2-8}$$

where x and y are 2-D Cartesian coordinates of Cassini oval related to polar coordinates, r and θ. Variation of coefficients c and d allows for obtaining different modifications of Cassini oval. The 3-D model particle shape is obtained by rotating the 2-D Cassinian oval (2-9) about its' longitudinal axis x (Figure 2-4). Hereafter, the 3-D particles having their longitudinal cross-sections as Cassinian ovals will be called Cassinian ovals for brevity.

2.3.2 Barrel-shaped modified Cassinian oval

A cluster of adhering particles, for example, the 3-D dendrite particle deposits in fibrous filtration [10], can be presented by a barrel-shaped modified Cassinian oval introduced in the current study:

$$r(\theta) = \pm c\sqrt{e + cos2\theta \pm \sqrt{\left(\frac{d}{c}\right)^4 - sin^2 2\theta},\ 0 \le \theta \le 2\pi} \tag{2-9}$$

where $e > 0$ is a modification coefficient defining size and geometric shape.

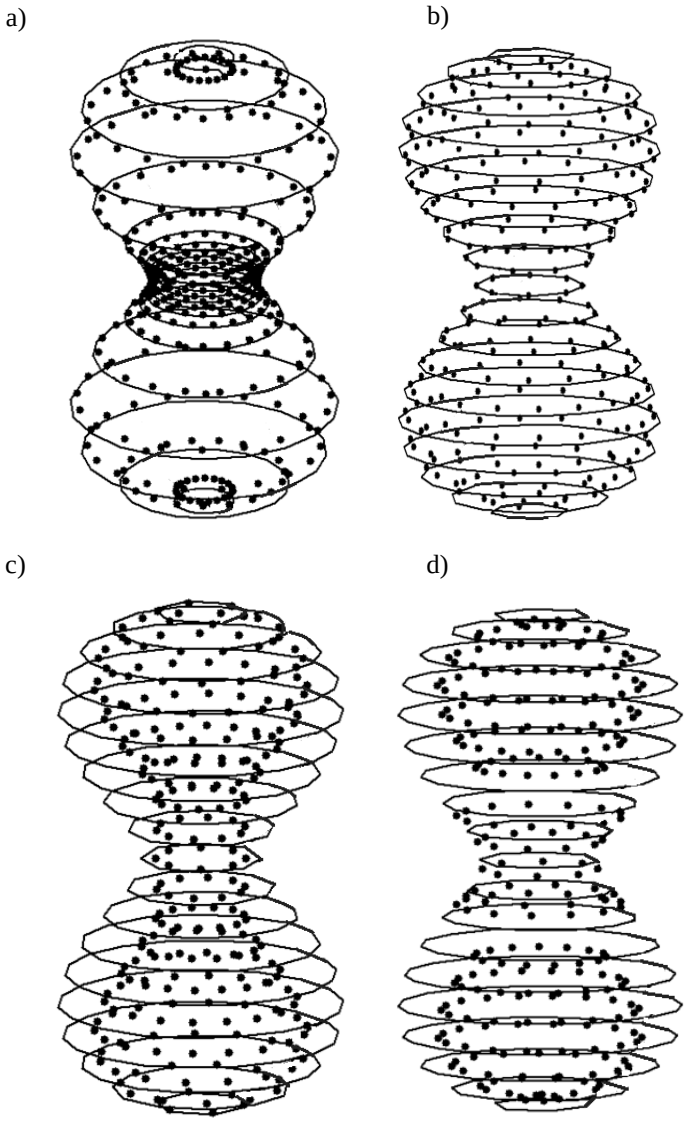

Figure 2-5 Stokeslets' allocation schemes for peanut-shaped (regular) Cassinian: a) non-uniform allocation (256 Stokeslets), b) uniform allocation (252 Stokeslets), c) local normal allocation scheme (258 Stokeslets), and d) combined allocation scheme (258 Stokeslets).

This type of modified Cassinian oval (2-9) has 8 inflexion points, near-flat surface regions with large curvature radii and areas with rapid change in curvature (Figure 2-6b). In formulas (2-8) and (2-9) the following values of parameters are adopted [48]: $c = 1$ and $d^4 = 1.1$.

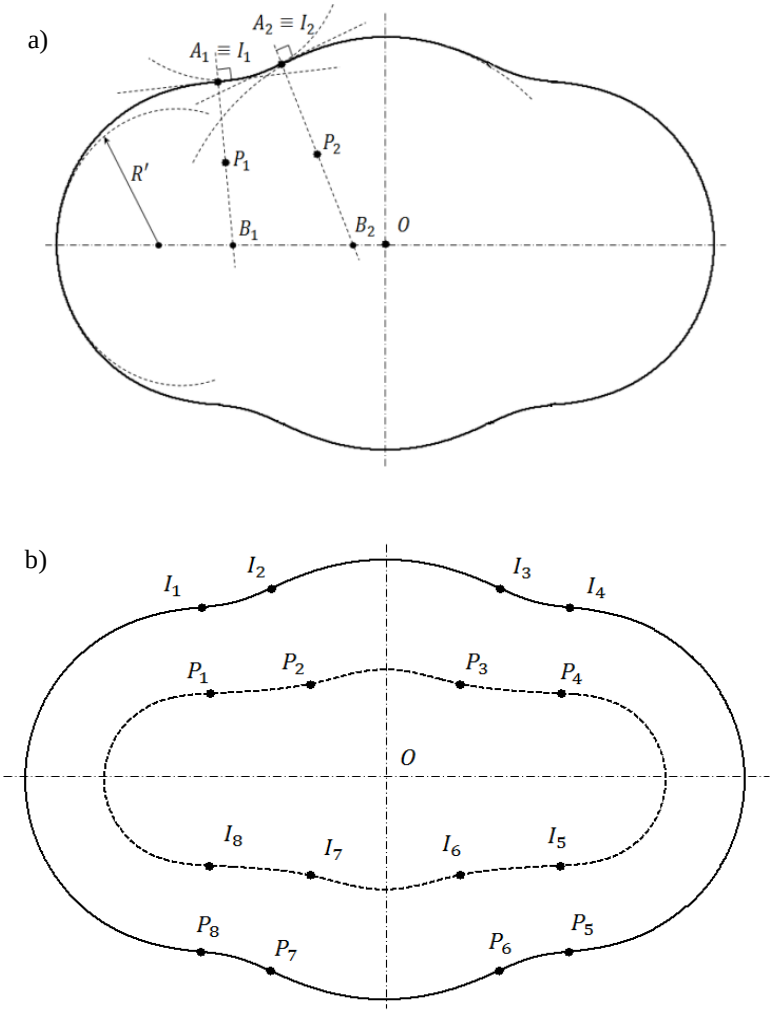

Figure 2-6 Local normal Stokeslet allocation for barrel-shaped (modified) Cassinian: a) representative geometric points for local normal method, b) resulting Stokeslet allocation curve (dashed line).

To describe non-equal pair of merging particles (Figure 2-3c, d), for example, water droplets captured by fiber [64], the stretched Cassinian oval is proposed as follows. In Equation (2-8) coordinate x is multiplied by the constant f_+ for positive x and by the constant f_- for negative x. The value of y remains the same as for original Cassinian.

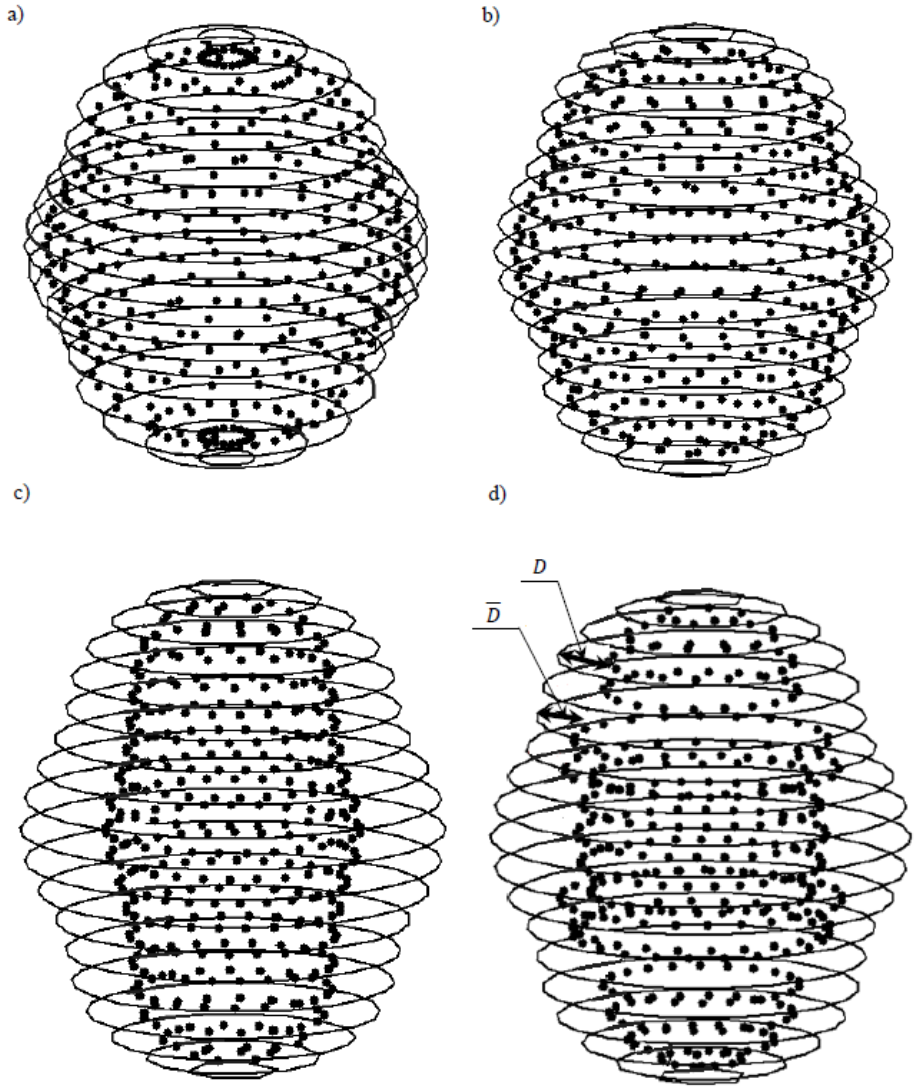

Figure 2-7 Stokeslets' allocation for barrel-shaped Cassinian: a) non-uniform allocation (361 Stokeslets), b) uniform allocation (384 Stokeslets), c) local normal allocation (387 Stokeslets), and d) combined allocation (387 Stokeslets).

Consequently, the volume of the stretched Cassinian remains the same as that for the original Cassinian (2-8) as soon as $(f_+ + f_-)/2 = 1$.

Uniform and non-uniform allocations of Stokeslets at submerged similar shape surface Γ_S are considered first. Non-uniform Stokeslet allocation scheme (Figures 2-5a and 2-7a) has an equal number of Stokeslets at each cross-section, which leads to more dense concentration of Stokeslets in the "neck" concave region as well as near the poles of the peanut-shaped merging pair of particles [17, 49].

In the next Section the BSM performance for this allocation is investigated and found to be least efficient for Cassinian convex-concave surfaces. Uniform Stokeslet allocation scheme (Figures 2-5b and 2-7b) has a homogeneous distribution of Stokeslets over submerged similar shape surface Γ_S. This helps to avoid unnecessary concentration of Stokeslets near the poles and "neck" regions and thus to reduce condition number of the matrix *M* (see Tables 1-2). As will be discussed in next Section, this method is more efficient compare to non-uniform allocation in terms of required number of Stokeslets, however, proposed below local normal and combined methods have superior performance.

The construction of Stokeslets' allocation surface by proposed methods for barrel shape is outlined in Figure 2-6. In Figure 2-6a, local curvature circles and points of intersection of local radii of curvature with the particle axis, B_1 and B_2, are constructed for a convex surface point A_1 and concave point A_2. The corresponding Stokeslet allocation surface points are determined by Equation (2-6). The optimal value of parameter *D* is shown in Tables 2-1 and 2-2 and discussed in the next Section. The

inflexion points I_1, ..., I_8 and corresponding locations of StokesletsP_1,…, P_8 are shown in Figure 2-6b.

The proposed combined scheme for regular and modified Cassinians (Figures 2-5d, 2-6c-d and 2-7d) is aimed at further reduction of condition number of the matrix *M* (see Tables 2-1 and 2-2). In Figure 2-6c, d the submergence depth is *D* for convex areas P_8P_1, P_2P_3, P_4P_5 and P_6P_7 and $\overline{D}$ for concave areas P_1P_2, P_3P_4, P_5P_6 and P_7P_8. The Stokeslet allocation surface is depicted in Figure 2-6c, d. The abrupt change in depth of Stokeslets' locations at inflection points is shown in Figure 2-6d.

The number of Stokeslets for the cases presented in Figure 2-6 is slightly different for various allocation schemes. For non-uniform Stokeslets' allocation scheme the number of Stokeslets is equal to N^2, where N is the number of cross-sections, while the uniform Stokeslets' allocation scheme places a different number of Stokeslets at each cross-section. Local normal (Figures 2-5c, 2-6a and 2-7c) and combined allocation (Figures 2-5d, 2-6c and 2-7d) schemes also produce different number of Stokeslets if one places Stokeslets uniformly at the constructed surface.

2.4 BSM results and evaluation of numerical efficiency for Stokeslets' allocation schemes

For the proposed Stokeslets' allocation schemes the BSM solutions were obtained and their convergence and computational efficiency are discussed in this Section. For the considered peanut-shaped and barrel-shaped Cassinians coefficients were selected in the previous section. A Stokes flow is oriented along the longitudinal axis of the Cassinians.

Values of μ and U_∞ are taken equal to unity. The convergence in terms of Stokes force as a function of the number of Stokeslets for peanut-shaped pair of merged particles is presented in Figure 2-8. Similarly, the Stokes force convergence for barrel-shaped cluster of merging particles is shown in Figure 2-9.

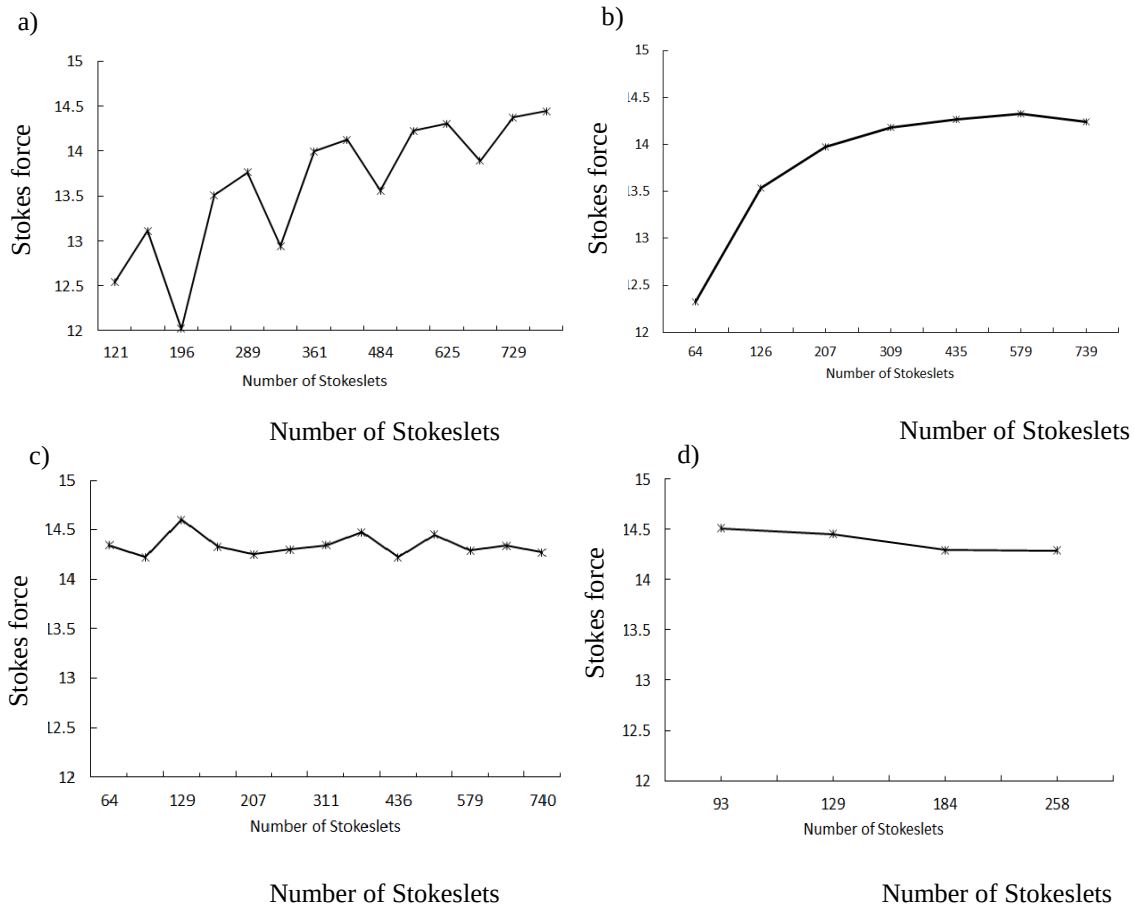

Figure 2-8 Stokes force convergence with the number of Stokeslets for various Stokeslet allocation schemes applied to peanut-shaped surface: a) non-uniform Stokeslet allocation scheme, $D = 0.05$, b) uniform allocation scheme, $D = 0.05$, c) local normal allocation scheme, $D = 0.22$, and d) combined allocation scheme, $\overline{D} = 0.08$, $D = 0.28$.

In Figures 2-8 and 2-9 and in Tables 2-1 and 2-2 the converged value of the Stokes force is 14.31 for the peanut-shaped Cassinian and 21.99 for the barrel-shaped Cassinian.

The Stokeslets' allocation depth is two decimals precise. The allocation depth, *D*, presented in Tables 2-1 and 2-2 corresponds to the minimum number of Stokeslets that is required to achieve convergence to above listed values of the Stokes force. The combined scheme (Figs.3.1c-d, 4.3c-d) has two parameters gathered in Tables 2-1 and 2-2: the Stokeslets' allocation depth for convex regions, *D*, and the Stokeslet allocation depth for concave regions including inflexion points, $\overline{D}$.

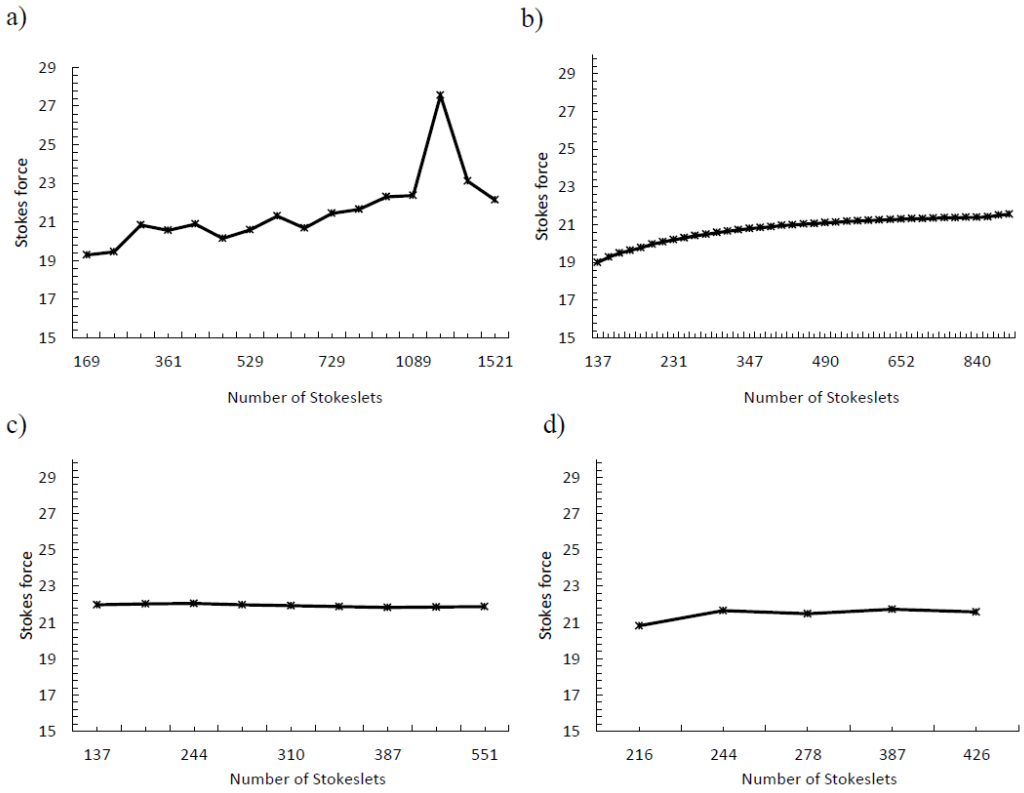

Figure 2-9 Stokes force convergence for longitudinally-oriented barrel-shaped cluster model: a) non-uniform Stokeslet allocation scheme, *D=0.05*, b) uniform allocation scheme, *D=0.05*, c) local normal scheme, *D = 0.4*, and d) combined scheme, $\overline{D} = 0.28$ and *D = 0.4*.

The BSM solutions were obtained using MATLAB (version 2013) backslash linear algebraic solver. An AMD Athlon quad-core processor of 2.8GHz each core and 8GB of RAM was used for computations and measurements of CPU time in Tables 2-1 and 2-2.

Table 2-1 BSM results for peanut-shaped Cassinian: comparison of performance of Stokeslets' allocation methods.

	Non-uniform	Uniform	Local normal	Combined
Stable Stokeslets' allocation depth range, D and $\overline{D}$:	D=0.03÷0.05	D=0.03÷0.05	D=0.20÷0.37	$\overline{D}$ =0.07÷0.29, D=0.05÷0.29
Optimum Stokeslet allocation depth	0.05	0.05	0.22	$\overline{D}$=0.08 D = 0.28
Minimum number of Stokeslets	625	579	404	258
Matrix condition number	1.5774e+20	3.4446e+18	2.2163e+016	7.2723e+012
CPU time, sec	31.31	28.46	18.55	5.61

Table 2-2 BSM results for barrel-shaped Cassinian: comparison of performance of Stokeslets' allocation methods.

	Non-uniform	Uniform	Local normal	Combined
Stable Stokeslets' allocation depth range, D and $\overline{\mathrm{D}}$	0.03÷0.05	0.03÷0.05	0.22÷0.7	$\overline{\mathrm{D}}$ =0.07÷0.35, D=0.05÷0.45
Optimum Stokeslet allocation depth	0.03	0.03	0.4	$\overline{\mathrm{D}}$=0.28 D = 0.4
Minimum number of Stokeslets	1521	867	387	295
Matrix condition number	2.6675e+21	4.1772e+017	4.0797e+013	5.6594e+012
CPU time, sec	224.89	86.21	11.58	7.69

In Tables 2-1 and 2-2, the condition numbers of the computational matrix M for considered Stokeslet allocation schemes are given for regular and modified Cassinians, respectively. The condition numbers of matrix *M* are given for the corresponding optimal number of Stokeslets and allocation depth for each Stokeslet allocation scheme. Uniform and non-uniform allocation methods have condition numbers of matrix *M* up to 10^{20}. The proposed allocation methods have smaller condition numbers $10^{11} - 10^{12}$ that is to their advantage. Tables 2-1 and 2-2 show that for the local normal and combined schemes submergence depth range, which corresponds to stable BSM solution, is significantly larger compared to known uniform and non-uniform Stokeslets' allocation schemes.

To form Tables 2-1 and 2-2, the allocation depth D (D and $\overline{D}$ for combined scheme) varies from zero to unity with the step of 0.01. For each depth, the minimum number of Stokeslets is obtained to have the relative error in terms of the Stokes force smaller than or equal to 0.1%. The absolute minimum in needed number of Stokeslets for each Stokeslets' allocation method and corresponding allocation depth is shown in Tables 2-1 and 2-2. For each Stokeslets' allocation method, the submergence depth range, which corresponds to stable BSM solution, is recorded in Tables 2-1 and 2-2.

For the regular Cassinian, D and $\overline{D}$ ranges are about the same (Table 2-1) allowing for accurate Stokes force and velocity solutions, while for the modified barrel-shaped Cassinian D range is larger than that for $\overline{D}$ (Table 2-2).

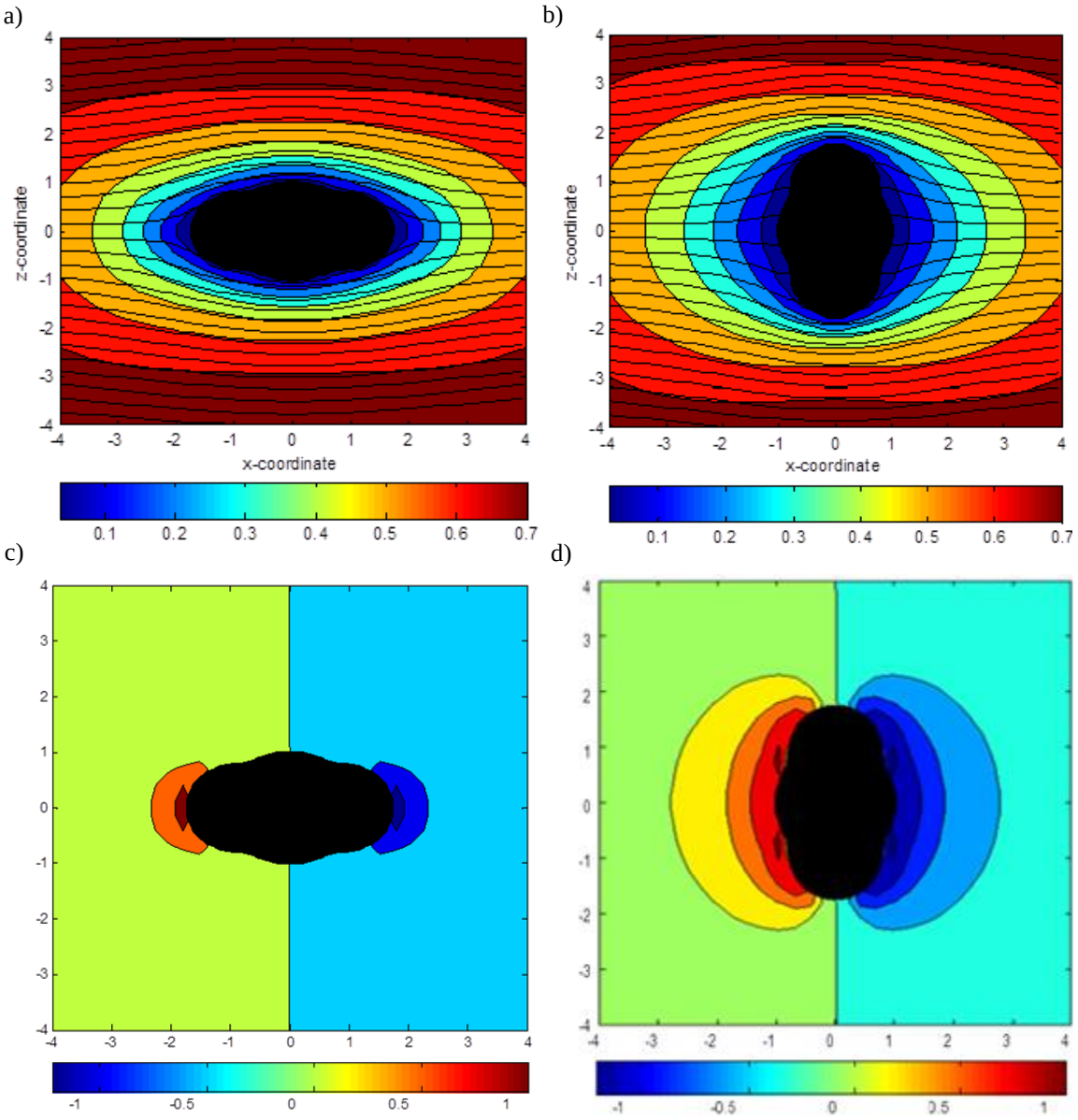

Figure 2-10 Pressure and velocity vector flow field about barrel-shaped Cassinian: a, c) longitudinally-oriented cluster, b, d) transversally-oriented cluster; a, b) velocity field and c, d) pressure field.

To maintain matrix condition number and solution stability, in combined method Stokeslets are placed close to the surface in narrow and concave regions including inflexion points. Out of the four Stokeslet allocation schemes considered, the combined

scheme delivers converged BSM solution using the minimum number of Stokeslets. This is due to the fact that at inflexion points and in concave regions Stokeslets' surface is formed differently than that for convex areas. In the proximity of inflexion points with infinite curvature radius (Figures 2-3c, 2-6c), $\widetilde{r_{ij}}$ vectors (see Equation 2-2) between neighboring Stokeslets and the corresponding collocation points are near-parallel, which leads to near-equal rows in the computational matrix *M* that makes *M* close to a singular matrix. The proposed combined allocation scheme was developed to improve the situation. The value of $\overline{D}$ is as small as in the similar shape uniform Stokeslet distribution scheme. As a result, the difference between radius-vectors connecting Stokeslets and collocation points for neighboring points at near-inflexion regions (see Figures 2-5d, 2-6c and 2-7d) becomes substantial to maintain smaller condition number of the computational matrix *M* (see Tables 2-1, 2-2) and reach the convergence using moderate number of Stokeslets.

The elapsed computer time are presented in Tables 2-1 and 2-2 and demonstrate its' significant reduction for the proposed allocation schemes and the decrease in the number of Stokeslets required for Stokes force to converge. In addition, the advanced Stokeslet allocation schemes show smaller oscillation of the Stokes force with the number of Stokeslets compared to BSM solution using the non-uniform Stokeslets' allocation scheme (compare Figures 2-8a and 2-9a).

As a result of application of the combined Stokeslet allocation scheme, the required CPU time has been reduced five times for regular peanut-shaped Cassinian (Table 2-1) and thirty times for a modified "barrel-shaped" Cassinian.

To illustrate the results of the proposed approach, Figure 2-10 presents pressure and velocity vector field for a modified Cassinian obtained using BSM with the combined Stokeslets' allocation scheme applied. To show applicability of the approach to an arbitrary flow direction, the pressure and velocity vector fields are presented for longitudinally and transversally oriented peanut-shaped Cassinians (see in next Section, Figures 2-11d – 2-14d).

2.5 Application of BSM to the merging particles Stokes force computation

Evaluation of Stokes force is important to study interaction of two spherical gaseous bubbles (Wijngaarden [65], Moshfegh, [66]) and liquid or solid particles approaching each other and adhering in the flow (Ardekani [61], Goldman, Cox and Brenner [67] and Laurenceau et al. [64]). Two slow-moving particles immersed in viscous media were considered in literature either in steady [68,69,70] or in unsteady formulation [61]. Considered cases of Stokes flow for particles in a different degree of proximity and corresponding computed pressure and velocity vector field are shown in Figures 2-11 through 2-14. The radius of each of two merging particles was chosen R = 0.5713, so as the total volume of two particles equals the volume of the peanut-shaped Cassinian (Figure 2-5) described by Equation (2-8) with its' parameters listed in Section 2.2. The quasi-steady approach to solution of Stokes equations is adopted for the lead-up to a merge. The drag force exerted to each particle by the flow is computed till they touch

each other. Then the drag force exerted on a single merged peanut-shaped particle is computed.

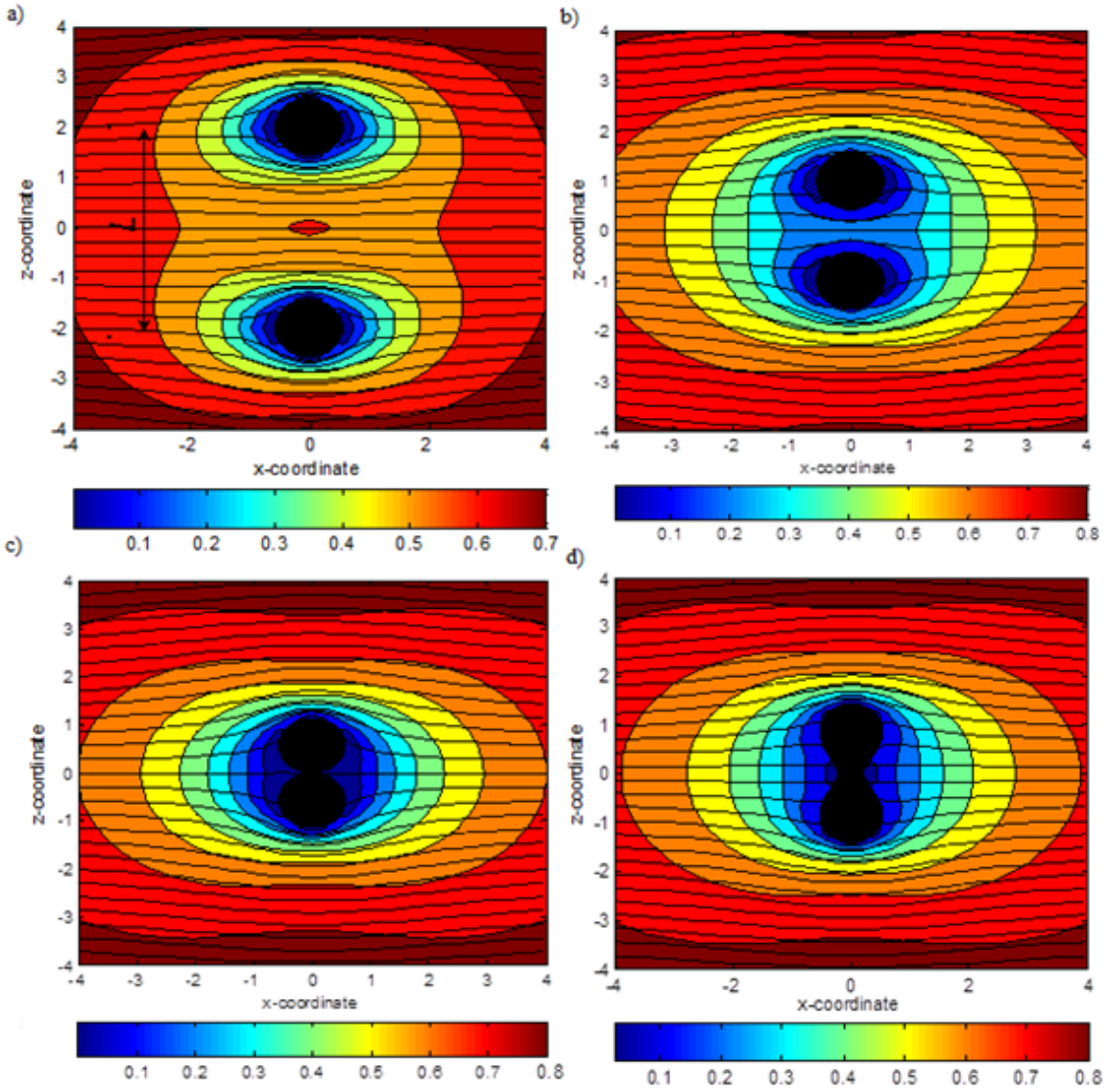

Figure 2-11 Velocity contours and field about two transversally-oriented spherical particles at various distance between their centers: a) *L=7R*, b) *L=3.5R*, c) *L=2R*, and d) merged transversally-oriented peanut-shaped Cassinian.

Depending on orientation of particles in the flow, two formulations of the problem are considered: a) Stokes flow about transversally-oriented particles [70] and b) Stokes flow

about longitudinally-oriented particles. In the former case a Stokes flow velocity vector field is normal to the line passing through the centers of both spheres as shown in Figure 2-11, while in the latter case a Stokes flow velocity vector field is parallel to the line passing through the centers of the spheres as shown in Figure 2-13.

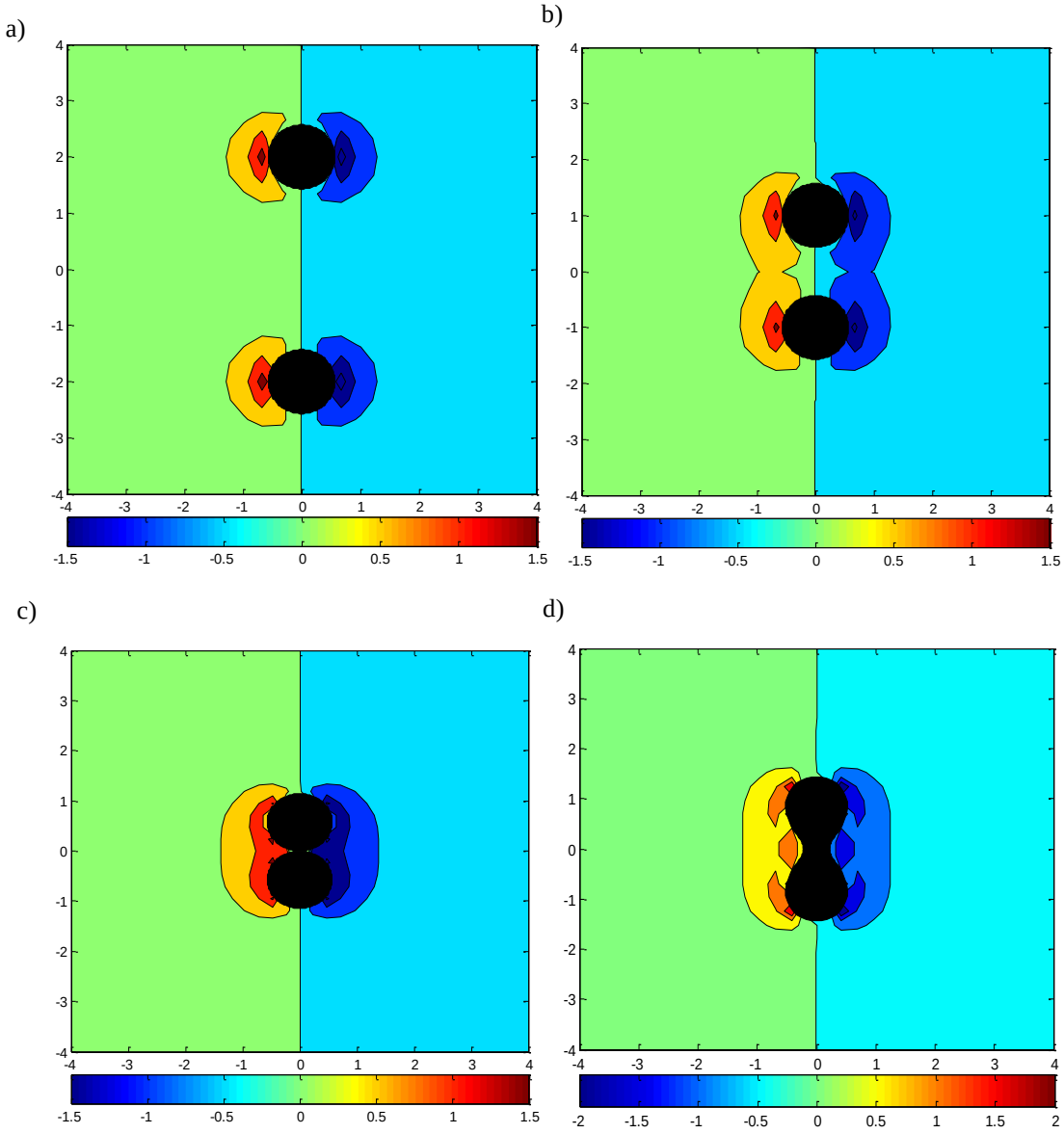

Figure 2-12 Pressure field about two transversally-oriented spherical particles: a) L=7R, b) L=3.5R, c) L=2R, and d) merged transversally-oriented peanut-shaped Cassinian.

Corresponding pressure field is shown in Figures 2-12 and 2-14. When the spherical particles merge in transversal orientation, they can form a peanut-shaped particle in an unstable transversal state (Figure 2-11d). Consequently, the angular momentum rotates merging pair of particles around its center of mass in the flow field and eventually the cluster takes a sustainable longitudinal equilibrium state (Figure 2-13d).

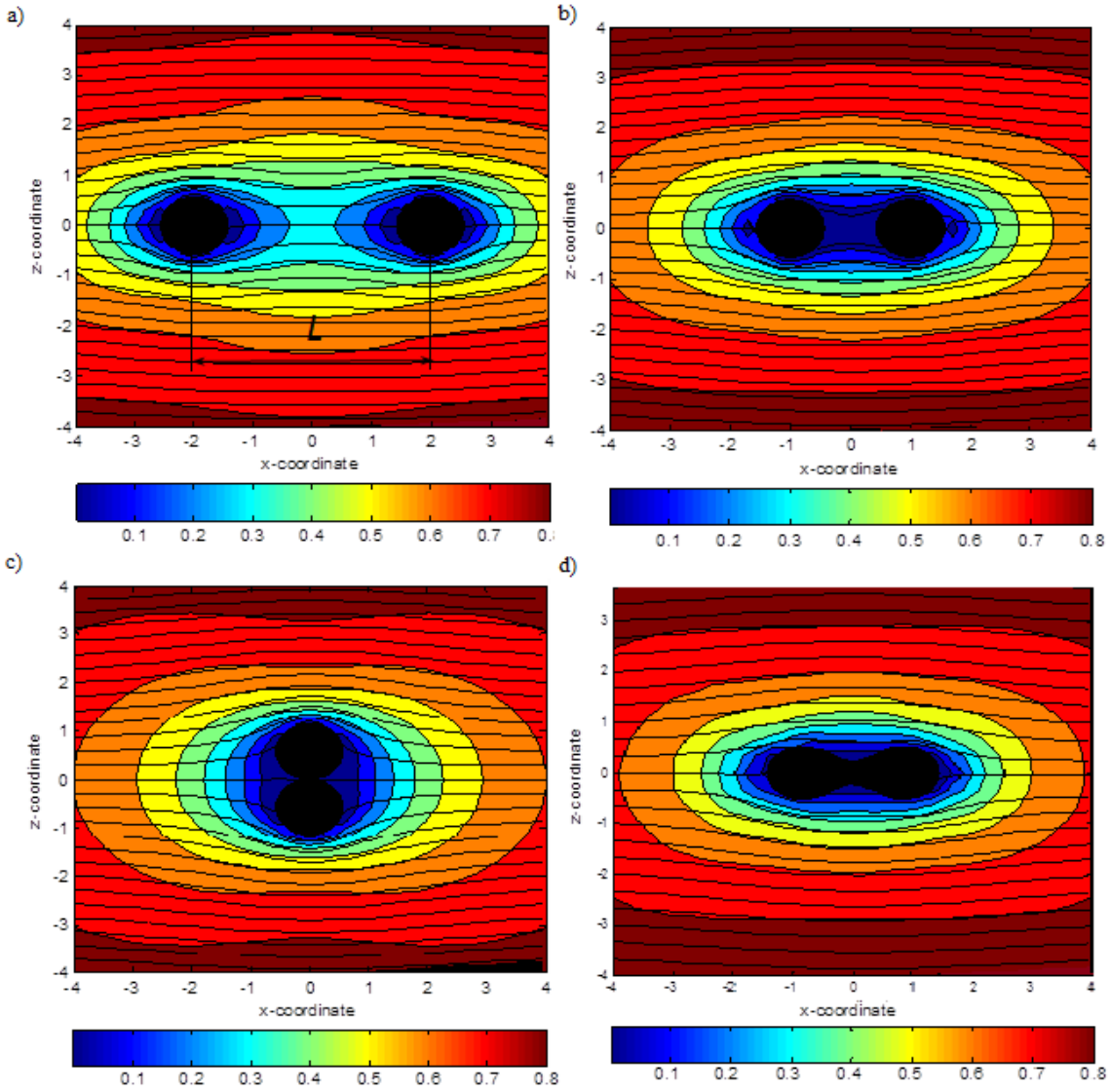

Figure 2-13 Velocity contours and streamlines about longitudinally-oriented spherical particles: a) *L=7R*, b) *L=3.5R*, c) *L=2R*, and d) merged peanut-shaped Cassinian.

Computations of the Stokes force exerted on particles were performed at characteristic stages of their merging. The uniform Stokeslets' distribution scheme with geometrically similar surfaces Γ_S and Γ [1, 2] is adopted for spherical particles before they merge. According to the results presented in Tables 2-1 and 2-2 (see previous Section), the local normal and combined Stokeslet distribution methods have demonstrated superior performance compared to uniform and non-uniform distribution schemes. The local normal and combined Stokeslet allocation schemes are used for merged particles.

The results obtained for the Stokes force about two spherical particles approaching each other correlate well with the results [67] obtained for two equal spheres. In BSM computations total force consists of the sum of z-components of Stokeslet solutions, while sums of *x*- and *y*- components cancel. The Stokes force for two equal spheres in longitudinal orientation (Figure 2-15a) is normalized by the sum of Stokes forces about two far apart spherical particles of equal radii, i.e. $F_{\Sigma} = 2[6\pi\mu R U_{\infty}]$.

The BSM simulation result shows that total Stokes force about two spheres contacting at a single point (*L=2R*) and oriented longitudinally to the flow direction (Figure 2-15a) is equal to 64.53% of that value, $F_{2\text{spheres}} = 0.6453 F_{\Sigma}$. Stimson and Jeffrey correction factor for two translating spheres moving in a Stokes flow parallel to far-field velocity vector [67] is 64.514%, therefore, the relative error of the BSM result is $\sim 10^{-4}$.

The BSM result is compared with the Stokes force obtained by Goldman, Cox and Brenner [67] for two spheres in the flow oriented transversally to the far field velocity

vector. The Stokes force about two spheres in contact ($L = 2R$) was 72.472% of F_Σ (Figure 2-15b). Its relative error compared to the solution [67] (72.469%) was $\sim 10^{-4}$.

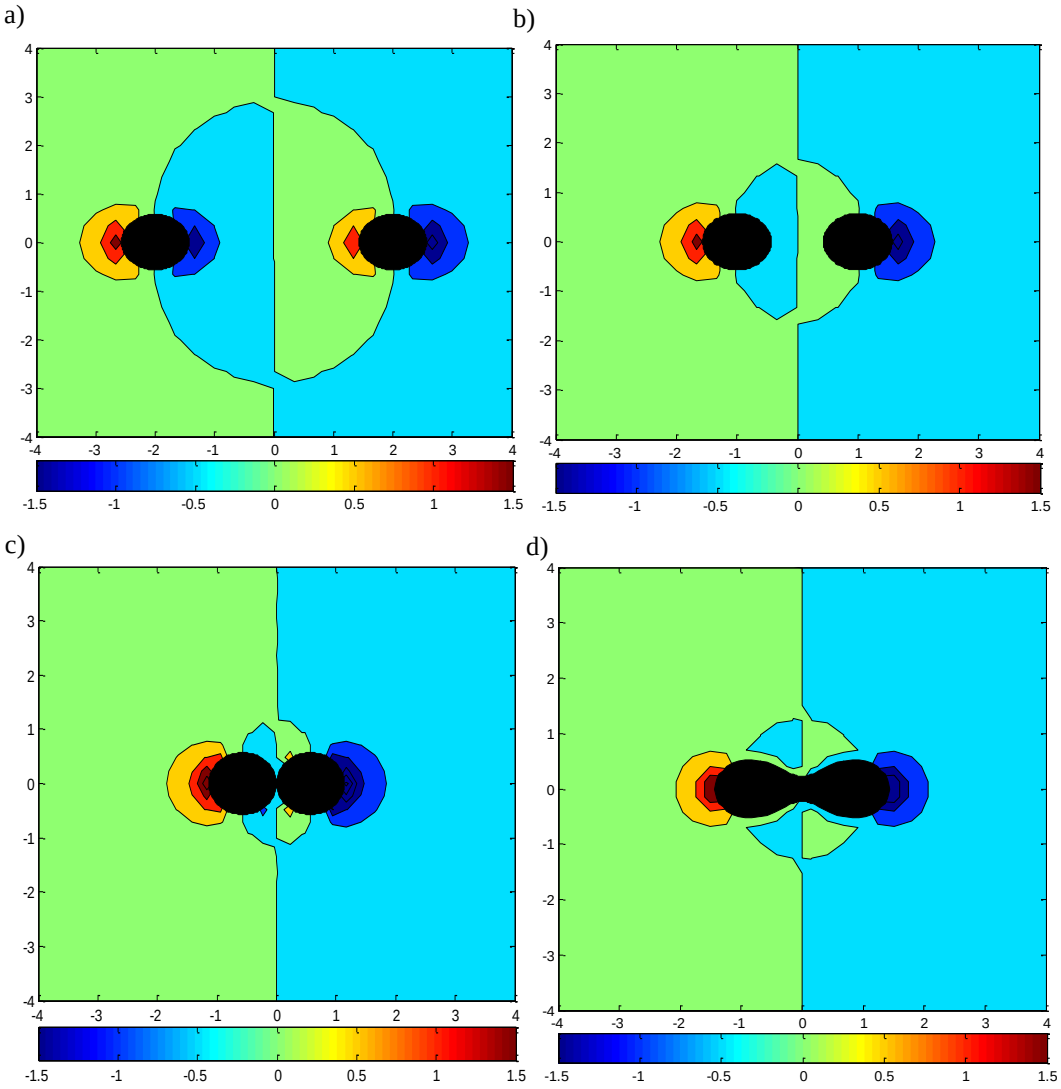

Figure 2-14 Pressure field about two longitudinally-oriented spherical particles: a) *L=7R*, b) *L=3.5R*, c) L=*2R* and d) merged peanut-shaped Cassinian.

The analysis of both cases shows that Stokes force decreases as soon as particles are approaching each other (Figure 2-15). This trend is valid until particles come into the

contact and start adhering. As soon as they start forming a peanut-shaped surface, Stokes force increases.

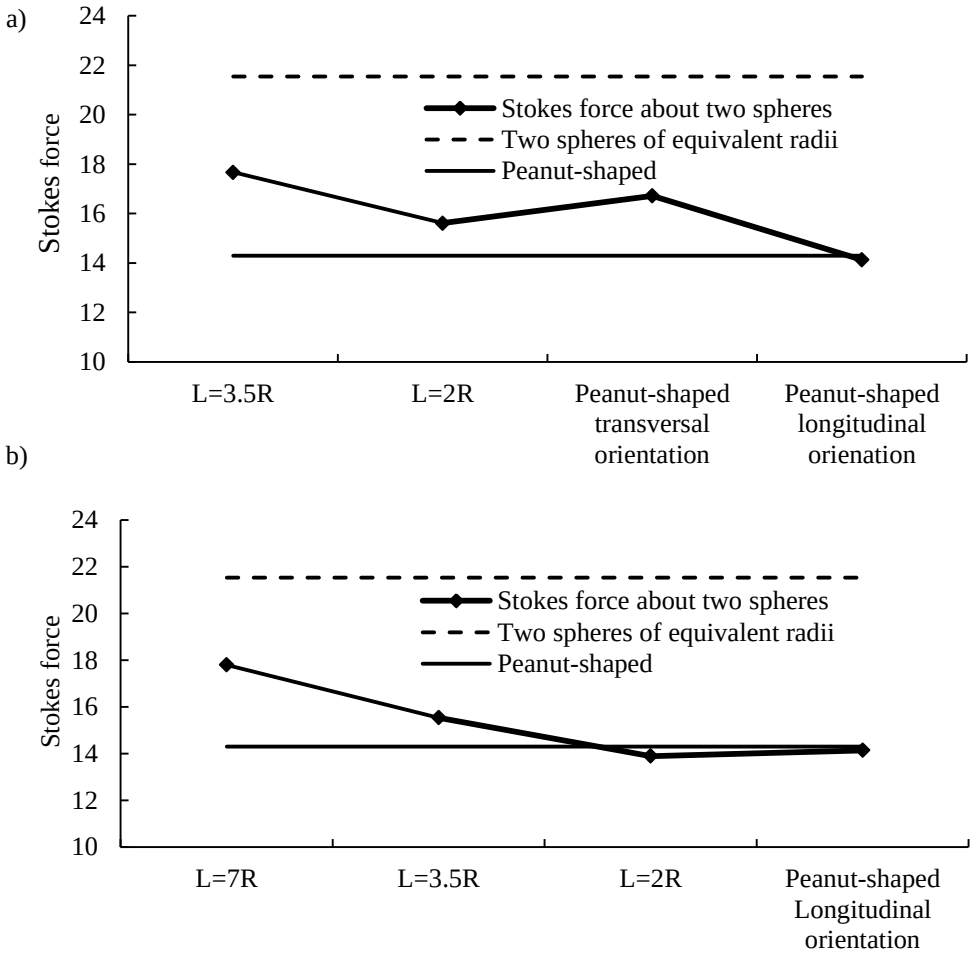

Figure 2-15 Stokes force exerted on two particles with various distances between particles: a) longitudinally oriented and b) transversally oriented. In sub-figures a) and b) the force acting on two isolated merging spheres of equal radius and the force acting on merging pair of spherical particles in longitudinal orientation are shown for comparison.

One may notice that the Stokes forces exerted on each of two particles are equal in longitudinal Stokes flow orientation regardless of the distance between particles. Stokes equations describe entirely diffusive exchange of momentum, where advection terms are

neglected. As a result, mutual hydrodynamic interaction between particles is of much longer range compare to cases with $Re > 1$ and the drag force on both particles become equal.

Obtained by the BSM computations, the repetitive pattern of pressure distribution about spherical particles in longitudinal orientation confirms this statement (see Figure 2-16). Indeed, the drag forces about each of two particles become unequal if particles are of different sizes [70, 71]. Note that if $Re > 1$ the flow cannot be described by the Stokes equations anymore and forward particle in longitudinal orientation gets larger drag even if two particles are of an equal size.

Figure 2-16 shows that the monotonic pressure distribution along the isolated particles' surface (Figure 2-16a) becomes non-monotonic as particles approach each other (Figure 2-16b,c). This causes reduction in net pressure force (the difference between pressures at front and rear semi-spheres). For the merged particles (Figures 2-16c,d), the area of non-monotonic pressure corresponds to the neck of Cassinian that confirms pressure isolines shown in Figures 2-14c,d.

In Figure 2-17 the Stokes force as a function of particle orientation with respect to the flow is presented. The zero degrees case corresponds to the transversal orientation while the ninety degrees corresponds to the longitudinal orientation. In Figure 2-17 the value of Stokes force on the sphere of equal volume is presented for comparison. The Stokes force reaches its' maximum value at about 45 degrees. The pressure and velocity flowfield for this case are shown in Figure 2-18. The maximum value of the Stokes force is close to that obtained for two spheres with the same total volume as the peanut shape.

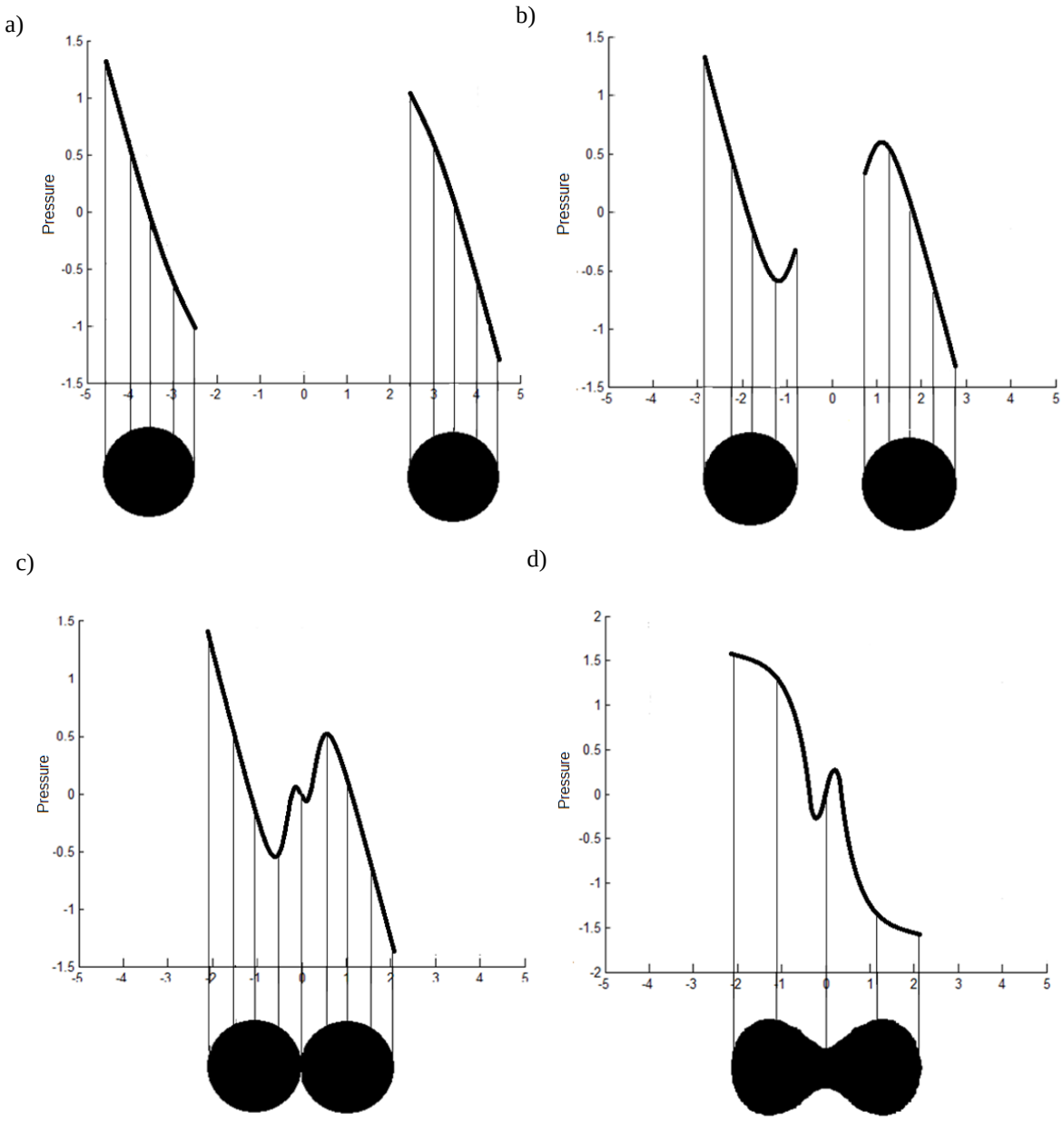

Figure 2-16 Dimensionless pressure distribution at the surface of two merging spherical particles in longitudinal orientation: a) *L=7R*, b) *L=3.5R*, c) *L=2R*, and d) peanut-shape merged spherical particles.

The minimum value of the Stokes force is observed in longitudinal orientation and close to that one obtained for a single sphere of an equal volume.

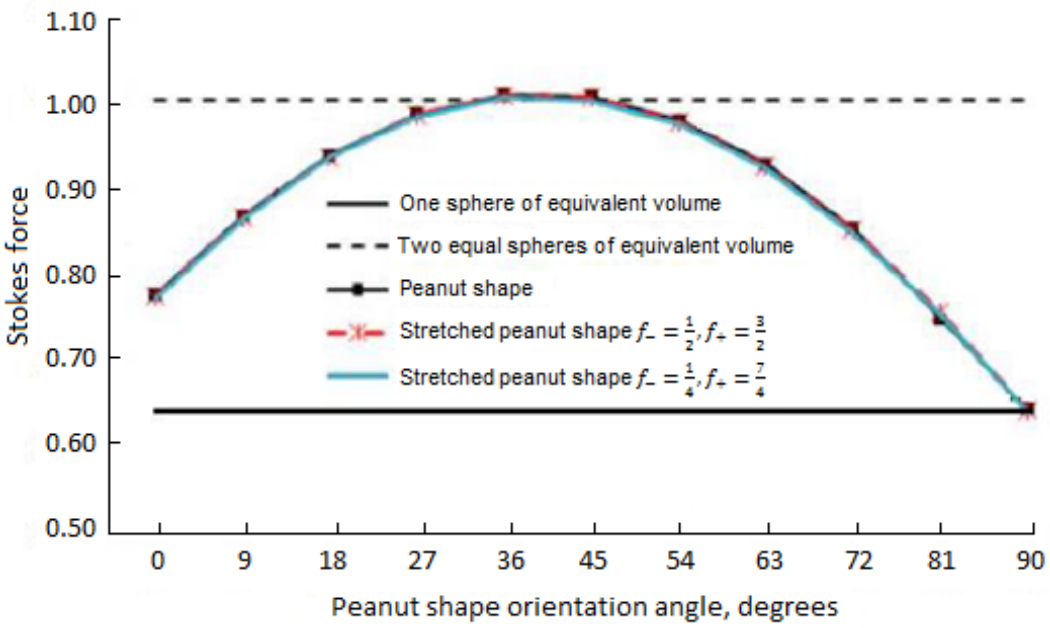

Figure 2-17 Stokes force exerted on peanut-shaped particles at the range of angles between particle's axis and the flow velocity. Results are presented for peanut-shaped Cassinian and stretched Cassinians with two pairs of stretching coefficients f_+ and f_-.

To confirm applicability of the proposed algorithms to a broader variety of merged particles and droplets, BSM was applied to two stretched Cassinian ovals with values of $f_+ = 1.5, f_- = 0.5$ and $f_+ = 1.75, f_- = 0.25$,respectively. The Stokes forces in Figure 2-15 practically coincide for cases considered.

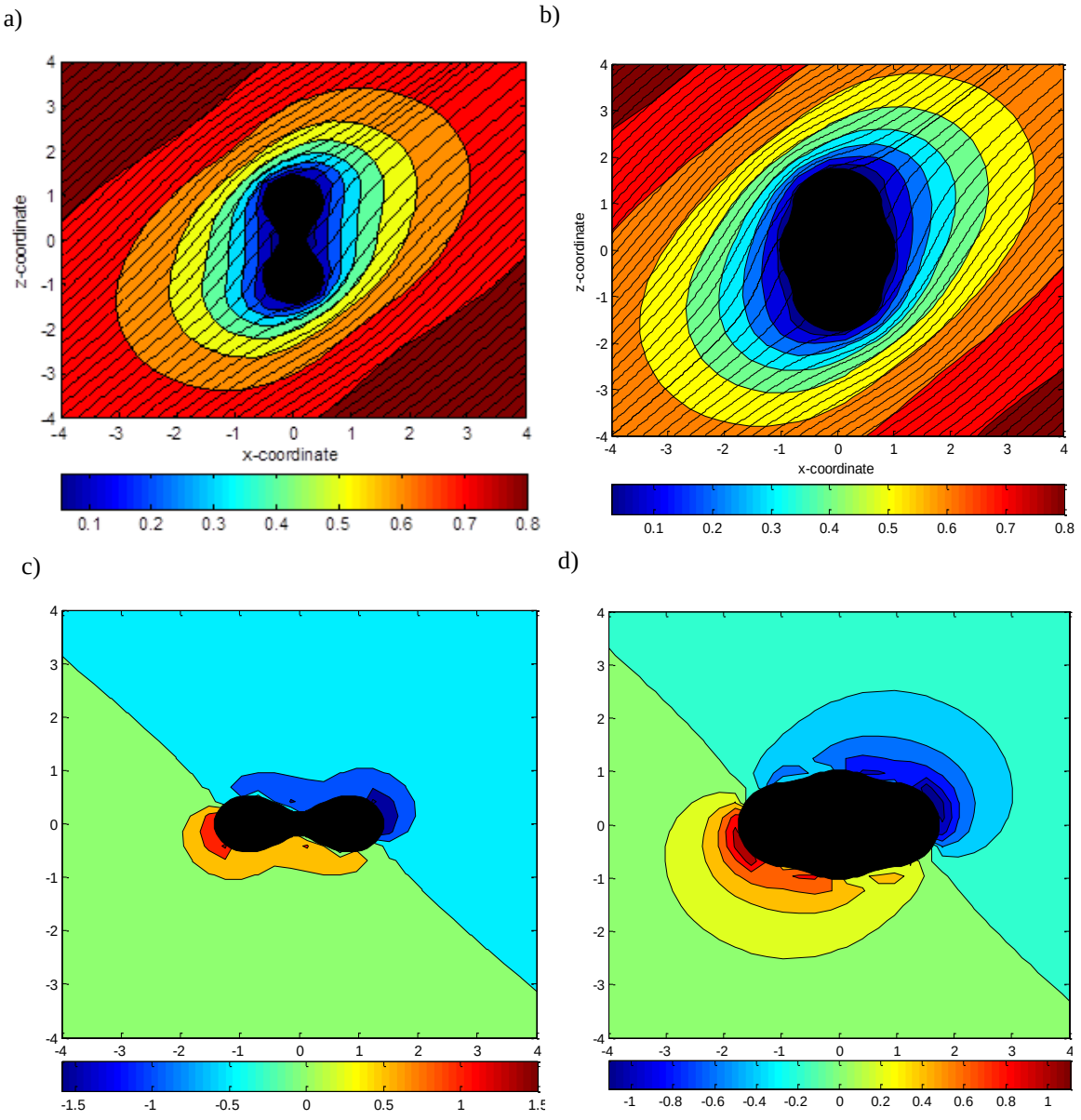

Figure 2-18 Velocity contours, streamlines and pressure for Stokes flow at 45 degrees with the axis of Cassini oval: a) velocity contours and streamlines about peanut shape, b) velocity contours and streamlines about barrel shape, c) isolines of pressure for the flow about peanut shape, and d) isolines of pressure for the flow about barrel-shaped Cassinian.

Computations presented in this section can be used to detect changes of the Stokes force at various phases of particles' collective motion and to apply appropriate measures to keep particles dispersed or, per contra, to collect them into pairs and clusters of particles.

2.6 Validation of the Stokes force for merging droplet surfaces

Validation of the Stokes force for a peanut-shaped 3-D body derived from 2-D Cassinian is possible using numerous empirical relations provided in literature. One of the most accurate total drag solutions may be obtained using empirical formula (11) introduced in [72] by Haider and Levenspiel. The Stokes force calculated $F_{Stokes} = 6\pi\mu R_{eq}$, where R_{eq} is a radius of sphere of equal volume, does not account for orientation of the considered surface with respect to flow and therefore it cannot accurately predict drag.

In order to find Reynolds number at a given dimensionless velocity and viscosity, one needs to find a characteristic dimension of the cross-sectional area.

$$C_D = \frac{24}{Re}\left[1 + e^{2.3288-6.4581\phi+2.4486\phi^2} Re^{0.0964+0.5565\phi}\right] + \\ +Re\frac{e^{4.905-13.8944\phi+18.4222\phi^2-10.2599\phi^3}}{Re+e^{1.4681+12.2584\phi-20.7322\phi^2+15.8855\phi^3}}, \quad (2\text{-}10)$$

where ϕ is a sphericity factor (see Equation 2-12).

For simplicity, we need to find dimensions of the given 3-D "peanut-shaped" body that has the same volume as the sphere of a unity radius. In order to do that, a special algorithm evaluating 2-D curve and derived 3-D shape geometric parameters was used (Figure 2.19).

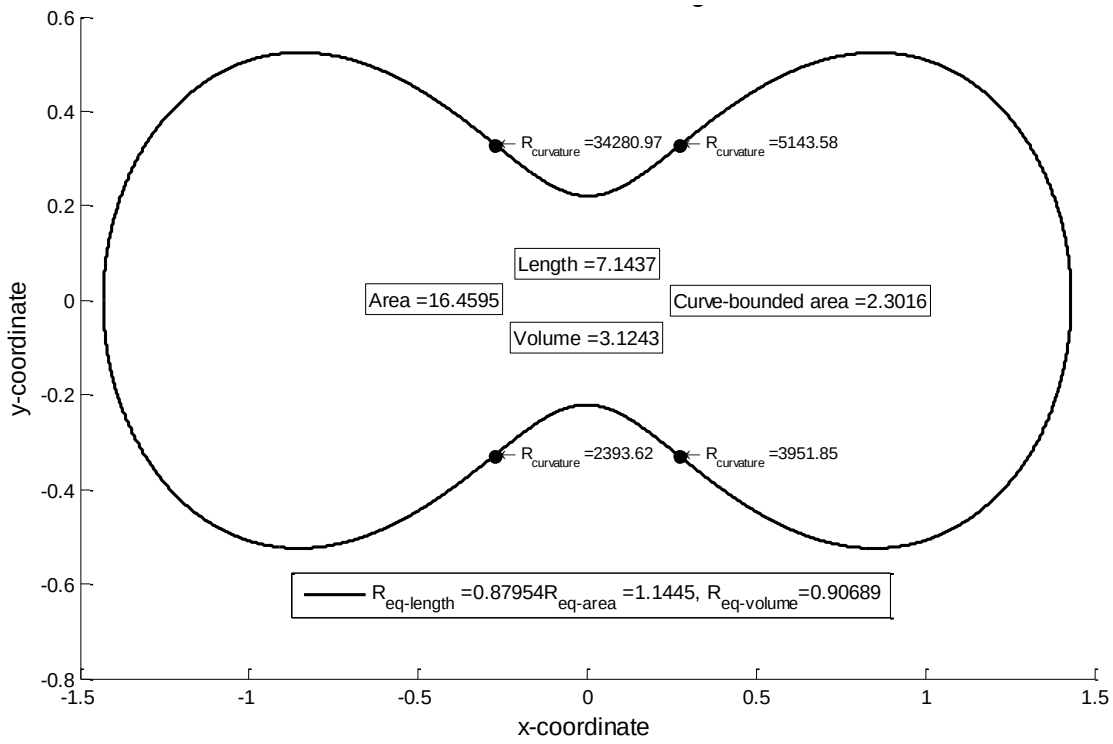

Figure 2-19 Parametric curve analysis. Traditional Cassinian.

It finds the initial curve length, local curvature radii, surface area and volume of the shape derived from the initial curve by its rotation around selected axis, as well as equivalent radius of the sphere having the same volume or the same surface area.

Looking in the figure above, one may find the radius/diameter of the middle section of the 3-D "peanut-shaped" body with respect to the flow depending on its' orientation. For longitudinal orientation, the middle section diameter is $D = 1.0488$.

Therefore:

$$Re_D = \frac{\overline{U_\infty} D}{\bar{\nu}} = 1.0488, \tag{2-11}$$

where U_∞ is the velocity of a far-field flow about the considered body. Finally, the sphericity parameter ϕ by definition is:

$$\phi = \frac{s_{sph}}{S_{body}} \tag{2-12}$$

where s_{sph} is a sphere area having the same volume as the considered "peanut-shaped" body, and S_{body} is a considered body surface area. The respective surface area of 3-D peanut-shaped body with the coefficients c and d taken equal to 1 and $1.1^{0.25}$ (Figure 2-19) is 16.4595, and the resulting sphericity is $\phi = \frac{4\pi}{20.0139} = 0.6279$.

Substituting the resulting values obtained in (2-10), the resulting drag coefficient for longitudinal orientation is $C_D = 33.8241$;

The total drag force (Stokes force) is computed with the following well-known [56] expression:

$$C_D = \frac{F_{Stokes}}{\frac{1}{2}\rho U_\infty^2 A_{mid}} \tag{2-13}$$

where A_{mid} is a 3-D shape middle section oriented across the flow.

$$Drag_\parallel = \frac{1}{2} C_D \rho U_\infty^2 A_{mid_\parallel} = 14.6110,$$

which may be compared to the values presented at Figure 2-15.

For transversal orientation, we need to calculate new Reynolds number based on middle section of equivalent characteristic diameter, which is presented at Figure 2-15 and equal to $A_{mid_\perp} = 2.3016$. The characteristic dimension of transversally-oriented "peanut-

shape" is $\max(x) - \min(x) = 2.8627$. The respective Reynolds number defined from characteristic dimension in the transversal shape orientation is also $Re = 2.8627$ according to (2-11) assuming that far-field velocity and kinematic viscosity are both normalized to unity. Then substituting again into the formula (2-10), we obtain $C_D = 14.6950$.

Finally, the total drag becomes:

$$Drag_{\perp} = \frac{1}{2} C_D \rho U_{\infty}^2 A_{mid\,\perp} = 16.9110;$$

It is easy to see that the resulting values obtained with (2-10) correlate well with the numerical results obtained with BSM. Total drag force computed with BSM is different from the solution proposed by Haider and Levenspiel by 2.06% and 1.13% for longitudinally and transversally oriented "peanut-shaped" model respectively. As it is mentioned by Hartman et al in [73], the deviation of the solution obtained from empirical formula suggested in Haider and Levenspiel for respective Reynolds numbers deviates from exact solution by 5-8%.

Present Chapter was dedicated to the development of more efficient allocation of singularities for merging particles and their clusters in Stokes flows. They were compared to traditional similar-shape uniform and non-uniform Stokeslet allocation schemes in terms of Stokes force convergence and extension of possible range of Stokeslet submergence depths. The next Chapter narrates about the development of a new computationally efficient Stokeslet allocation scheme particularly for the problems of interaction of droplets and fibers in low-Reynolds number flows.

CHAPTER III

DEVELOPMENT OF THE BOUNDARY SINGULARITY METHOD FOR HYDRODYNAMIC INTERACTION PROBLEMS IN FIBROUS FILTRATION

As it was mentioned in literature (Zhao and Povitsky [1-5], Wrobel [74]) BSM became more advantageous over traditional mesh-based methods. BSM requires optimization of allocation of boundary elements to reduce the computational time and increase solution convergence. It was shown in Mikhaylenko and Povitsky [75] that CPU time of BSM method needed to obtain solution of the same accuracy in terms of Stokes force and velocity may drop 4 to 6 times for the proposed local normal and combined schemes compared to the similar-shape non-uniform scheme of allocation of singularities.

The modelling of Stokes flowfield about micro- and nano- scale droplets in their proximity to fibers describes flow physics of fibrous filtration and is crucial in predicting drag force and filtration efficiency (Hosseini and Tafreshi [76], Viswanadam and Chase [77], Kulkarni, Patel and Chase [78]). The modelling of flow about droplets and computation of total drag and velocities about surfaces at different stages helps to clarify particle and droplet capturing mechanism (Winkler et al [79]). On another hand, the problems of hydrodynamic interaction between surfaces are challenging in terms of BSM application, because singularities located near the points of contact of the bodies increase

the condition number of the computational matrix and negatively affect solution accuracy. Therefore, the problem of optimal allocation of singularities becomes a critical part of computational set-up.

3.1 Representative model of a Stokes flow about "droplet – fiber" system

Before application of the BSM to the Stokes flow about ensembles of droplets of complex convex-concave shapes and spherical droplets in proximity to each other, a simple 3-D Stokes flow about single sphere and a 2-D Stokes flow about cylinder were solved to validate the approach. The obtained results have matched well-known analytical solutions (Fay [80], Batchelor [18], Schlichting [56]) for the sphere:

$$F_{SS} = 6\pi\mu R U_{\infty} \tag{3-1}$$

and for a cylinder (per its unit length):

$$F_{SC} = \frac{4\pi\mu U_{\infty}}{ln\left(\frac{7.4}{Re_D}\right)} \tag{3-2}$$

where U_{∞} is a far-field velocity.

For the problem of a Stokes flow about spherical droplet settling on fiber depicted at Figure 3-1a, the ratio of droplet to fiber $R_{sphere}/R_{cylinder} = 0.5$ was selected first. The method of submerged Stokeslets presented at Figure 3-1 was used, i.e. fundamental solutions were located under the surface of considered geometrical model. The normalized Stokeslet allocation radius for spherical droplet was chosen $R_{SS} = 0.7$ as an

optimum one proposed in [5], and the uniform Stokeslet allocation scheme was selected as described in [75].

3.2 Proposed Stokeslet allocation scheme for "droplet – fiber" systems

The placement of Stokeslets for a cylindrical fiber (Figure 3-1) was studied in terms of velocity vector field and Stokes force accuracy [81]. In order to apply BSM to the 3-D Stokes flow about the finite length fiber (cylinder) and to get accurate velocity vector field, one has to place Stokeslets so as the normalized Stokeslet allocation radius to satisfy condition:

$$R_{SC} = 0.5 \div 0.8 \tag{3-3}$$

The analysis of geometrical setup of a Stokes flow about spherical droplet touching a fiber solved with BSM leads to elevated condition number of the matrix *M* designated by near-parallel vectors directed from Stokeslets to collocation points [1-5]. This requires allocation of Stokeslets close to the surface.

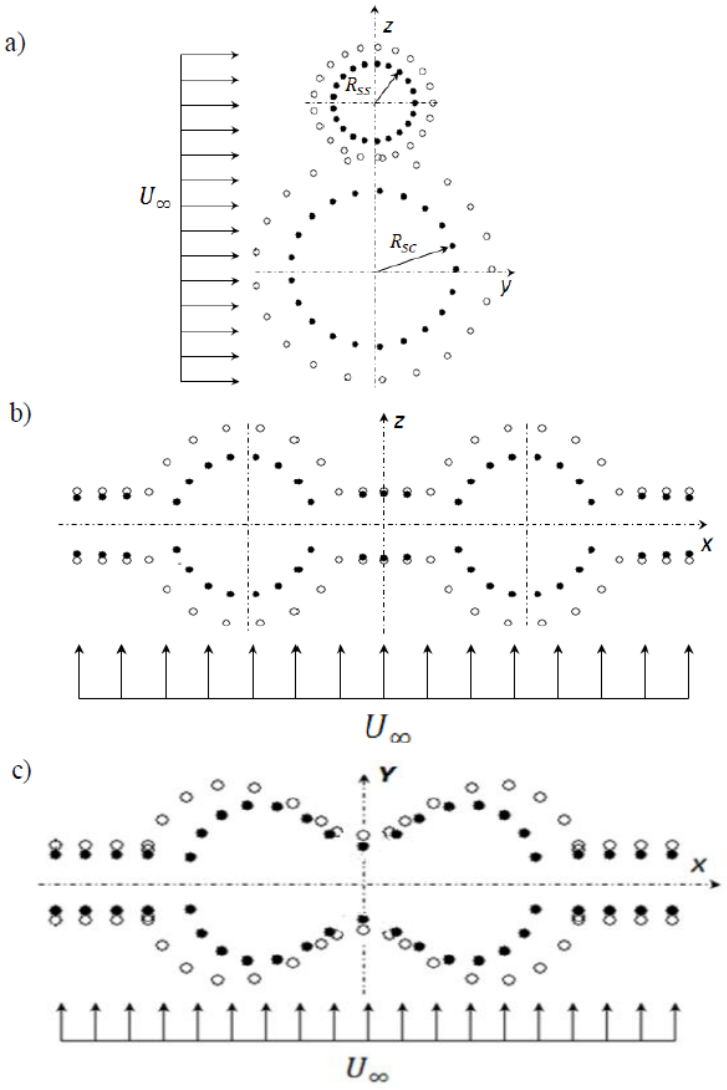

Figure 3-1 Problem set-up and Stokeslet allocation schemes: a) flow about droplet sticking to the fiber, b) flow about two droplets sitting on the fiber and 3) flow about droplets merging to the "peanut-shape" cluster around fiber surface. o - collocation points, · - Stokeslets.

Values of R_{SC} outside of range (3-3) distort velocity flow field for a cylinder and affect accuracy of the solution about sphere in proximity to the point of contact. In order to avoid this inaccuracy, the Stokeslet submergence depth in the vicinity of point of contact needs to be small enough, that is $R_{SC} \to 1$. However, numerical experiments show

that as $R_{SC} \to 1$, the velocity component of the resulting flow field about cylinder is incorrect near the cylinder surface (Figure 3-3a). If $R_{SC} < 0.5$, the computational matrix M condition number increases and the solution becomes inaccurate. For traditional "equidistant" scheme with $R_{SC} = 0.1$ with $N = 650$ Stokeslets, the condition number increases to 1.1674e+026.

Using the same scheme with $R_{SC} = 0.7$ and $N = 802$ Stokeslets, the condition number obtained was 6.6079e+019. To satisfy condition (3-3) apart of point of contact and to improve solution accuracy near the point of contact, the radius R_{SC} should vary along the fiber depending on the distance from the point of contact ($x = 0$).

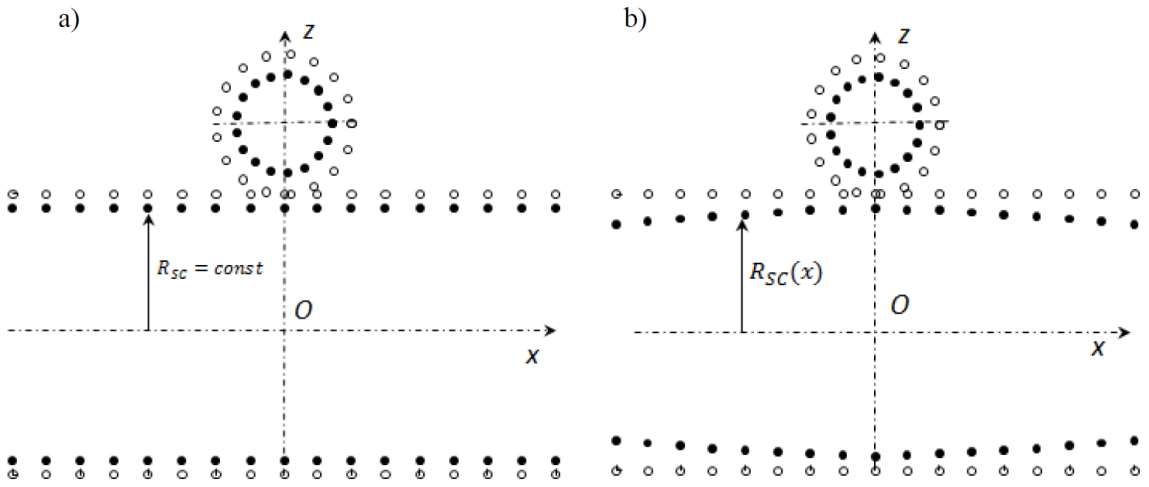

Figure 3-2 Stokeslet allocation scheme for the flow about droplet on a fiber:
a) equidistant scheme, b) alternative scheme: (−° −) collocation points,
(− · −) Stokeslets.

Two schemes for 3-D flow about finite cylinder with attached droplet are considered: the traditional "equidistant" scheme (Figure 3-2a), where Stokeslet placement radius $R_{SC} = const$ in the axial direction and the new scheme described here.

The proposed scheme satisfies condition (3-3) apart from point of contact and, simultaneously, allows allocating Stokeslets close to surface near the contact point. The allocation depth as a function of distance to contact point is described by the following formula:

$$R_{SC}(x) = R_{max} \cdot e^{\left(-\frac{\lambda|x|}{L}\right)} \tag{3-4}$$

where x – axial coordinate along the cylinder, R_{SC} – Stokeslet allocation radius, R_{max} – parameter defining the location of Stokeslets closest to the surface of the cylinder near the point of contact with a spherical droplet in the middle of the cylinder: $x = 0$, λ is a differentiation coefficient affecting the range of Stokeslet allocation radii along the fiber.

3.3 Validation of the proposed Stokeslet allocation scheme.

The resulting solution for a spherical droplet touching cylindrical fiber using "equidistant" Stokeslet allocation scheme with $R_{SC} = 0.97$ is shown at Figure 3-3a. One may observe irregular velocity vectors representing violation of no-slip and non-penetrating boundary conditions at the cylinder surface. This was accompanied by the high computational matrix condition number observed when solving linear system of equations. The matrix condition number in this case exceeded 1e+031. For the close to

surface equidistant Stokeslet allocation ($D < 0.1$ or $R_{SC} > 0.9$) this was observed for the figures of large principle curvature radii in any of the directions. The Stokeslet allocation scheme presented here for cylindrical fiber is aimed to struggle with this phenomenon.

For proposed Stokeslet allocation scheme applied to the case of Stokes flow about droplet on a fiber, the parameters of scheme introduced by Equation (3-4) were taken: $\lambda = 0.075$, $L = 10R$ and $R_{max} = 0.97$, where $L = 10R$ and $R = 1$ are dimensionless length and radius of cylindrical fiber for this case.

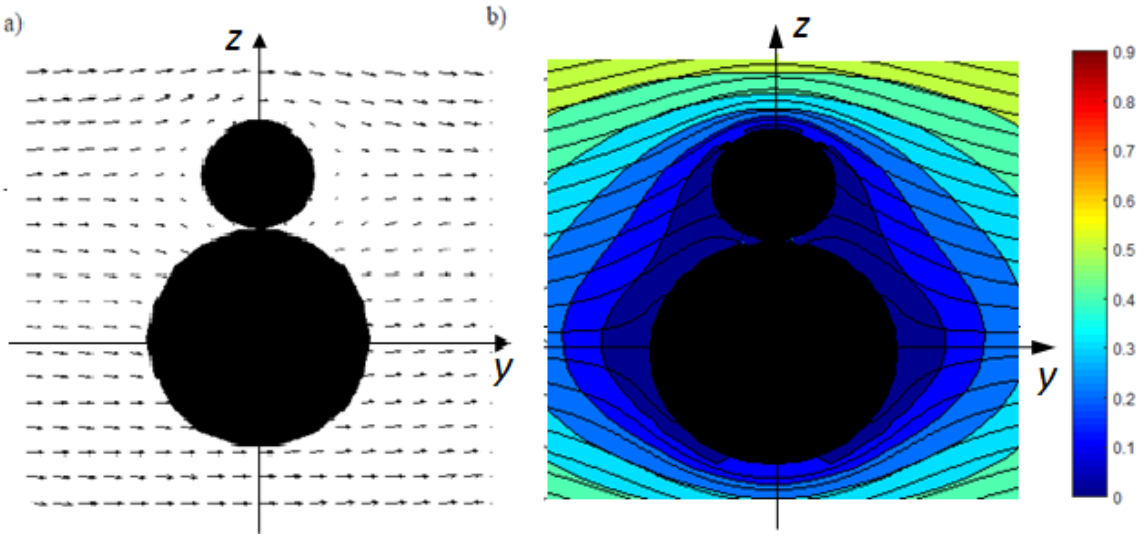

Figure 3-3 A ZY-plane view at 3-D velocity about spherical droplet on cylindrical fiber: a) "equidistant" allocation scheme at R_{SC} = 0.97, N = 677 Stokeslets, b) proposed allocation scheme (3-4), R_{max} = 0.97, λ = 0.07, N = 498 Stokeslets.

By varying parameters a and R_{max} it is possible to tune the scheme in the way to reduce the number of Stokeslets and achieve accurate flowfield parameters. For example, by changing parameter λ from 0.075 to 0.05 and keeping $R_{max} = 0.97$ it was possible to achieve accurate velocity vector field for $N = 352$ Stokeslets instead of $N = 560$ for the

traditional non-uniform scheme. The minimum condition number achieved for proposed scheme was 1.83e+019 for $N = 444$ Stokeslets.

Similar effect in terms of velocity vector field accuracy was obtained for the problem of a Stokes flow about "peanut-shape" droplet cluster on a cylindrical fiber. Submergence of Stokeslets with $R_{SC} = 0.7$ or application of proposed Stokeslet allocatiocation schemes helped resolving this issue.

3.4 Application of BSM to Stokes flow problems of "droplet – fiber" interaction

In order to demonstrate capability of BSM and proposed Stokeslet allocation schemes for droplet-fiber system, three test problems of variation of the Stokes force about cylindrical fiber loaded with spherical droplets are considered as shown in the Figure 3-1.

The first problem presumes evaluation of drag versus the radius of spherical droplet sticking to a fiber. The ratio of radii $R_{sphere}/R_{cylinder}$ varied from 0.1 to 1 (Figure 3-4a). The second test problem is evaluation of the Stokes force at flow angles between flow velocity vector and y-axis varying from 0 to 90 degrees. The results illustrated on Figure 3-10b, were obtained for the different length-to-radius ratio for comparison. First case is presented for unit length cylinder with $R_{cylinder} = 1$ and the second case is presented for the length-to-radius ration equal to 5. The third problem studies the flow about two droplets, one sliding along the fiber toward another and merging into a "peanut-shape"

cluster. All these problems are important in terms of determining filtering efficiency and help predicting droplets and particles capturing effects (Yarin and Chase [82]).

The Stokes force (total drag force) was calculated for a spherical droplet at a cylindrical fiber of unit length using the proposed BSM approach and then normalized over analytical Stokes force value F_{SC} for a circular cylinder (3-2).

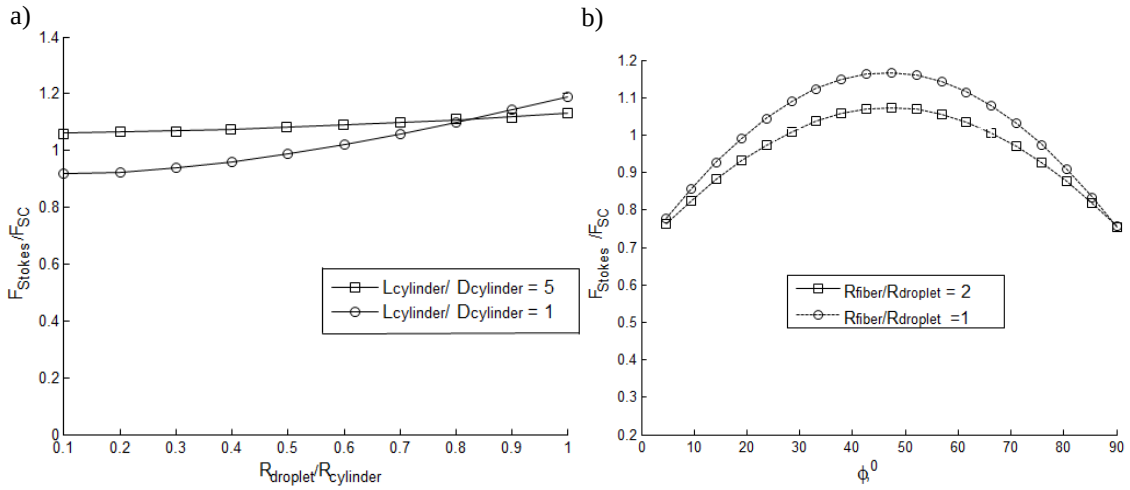

Figure 3-4 Stokes force about cylindrical fiber loaded with spherical droplet: a) Drag vs flow orientation angle, b) total loaded fiber drag F_{Stokes} versus $R_{sphere}/R_{cylinder}$ ratio. F_{SC} is a Stokes force about the part of single cylindrical fiber of $2R_{sphere}$ length without presence of droplet.

The results provided at Figure 3-4b are somewhat comparable to the total drag shown in [76] for cylindrical fiber loaded with sticking droplet dendrite for considerable solid volume fraction α and packing density. Total loaded fiber drag hereto designate the sum of Stokes forces about spherical droplets attached to a part of fiber with the length of one fiber diameter with the middle in a contact point. The volume fraction is determined as:

$$\alpha = \frac{N_p V_p}{Ah}, \tag{3-5}$$

where V_p is the single droplet volume, N_p – total number of droplets, A – view area and h is the depth of view. In the present test problems $\alpha = 9.82\%$, which is close to the one presented in [76].

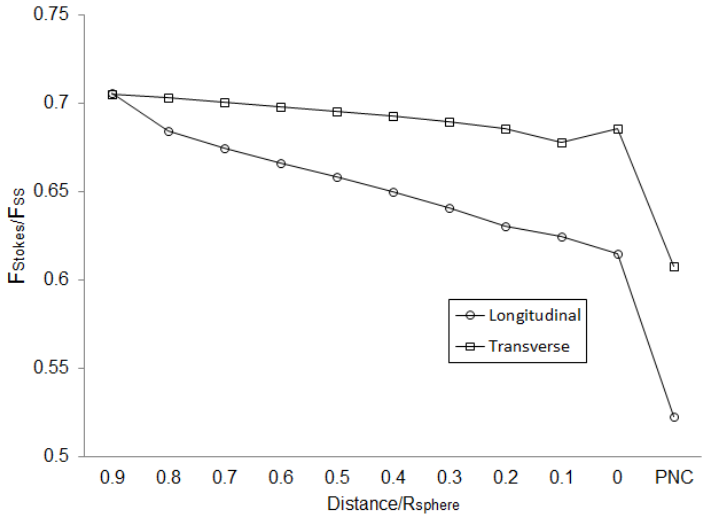

Figure 3-5 Stokes force (total drag) about two merging spherical droplets at cylindrical fiber versus distance between droplets normalized over droplet radius. The limiting case is a "peanut-shape" cluster (PNC) that is formed by droplets at merger phase.

The total drag exerted by a Stokes flow about two droplets settling on a fiber and merging to a "peanut-shape" cluster is shown at Figure 3-5. The Stokes force about spherical droplets was evaluated for both longitudinal and transversal far-field flow orientation.

It is worthwhile noting that accurate solution could not be obtained for traditional non-uniform and equidistant allocation schemes for the sphere and for cylindrical fiber respectively. Slow convergence of non-uniform scheme and solution artefacts observed

for equidistant scheme applied to cylindrical geometry negatively affect solution convergence for the overall boundary surface formed with contacting sphere and cylinder. Therefore, the proposed Stokeslet allocation scheme or alternative schemes are needed.

The resulting drag obtained for two merging droplets on fiber when the surface of the latter is completely covered, may be compared with the drag force obtained by Goldman, Cox and Brenner in [67] for two contacting particles in longitudinal or transversal translational motion in a creeping flow.

The developed schemes and the results provided in Chapters II and III are helpful in evaluation of the steady-state problems of a Stokes flow parameters in particulate multiphase flows, fibrous filtration. The next more complex extension to a Stokes flow problems considered in this work encompasses quasi-steady processes of viscous deformation of liquid surface under low-Reynolds number flows in micro-channels, which is described in Chapter IV. Among other methods, MRS with uniform allocation scheme for micro-scale low Reynolds number flow coupled with FV method for macroscopic flows have been used.

CHAPTER IV

MODELING OF THE NGJ PROCESS BY EXPERIMENTAL AND COMPUTATIONAL STUDY OF DEFORMATION OF POLYDIMETHYLSILOXANE DROPLETS AND TRACKS IN A RECTANGULAR CHANNEL

As mentioned in the Introduction, the meltblowing and NGJ nanofiber (Figures 1-1 and 1-2) derivation processes have many advantages compared to traditional spinning methods, especially when applying materials with sophisticated rheology. The latter includes but is not limited by liquid crystal mesophase pitches and other carbon-based polymers. The study of the NGJ nanofiber derivation method is critical for understanding and improvement of the process in terms of determination and control of outcome product specifications, e.g. thermoelectric and mechanical properties, structure homogeneity and morphology. The proper control of air flow parameters and the homogeneity of liquid surface perturbations help to minimize standard deviation and dispersion of derived submicron/nanofibers diameters and to make them uniform, as well as to achieve desired morphology, which is important for commercial companies working using submicron and nanoscale precursors for the composite materials production.

However, visualization of the process inside a nozzle is a laborious process hindered by the lack of access to a gas-liquid reacting zone for high-speed imaging. An alternative

way to reproduce the process taking place in such reaction nozzle areas is based on scaling up the nozzle and studying liquid deformable surface of sample droplets controlling air flow velocity and its' orientation in a considered area. In the present Chapter experimental deformation of polydimethylsiloxane (PDMS) droplets and tracks is studied. The experiments with a scaled up replica of the gas-liquid reaction zone of the NGJ nozzle channel were attempted to model processes in the real scale NGJ nozzle and predict viscous deformations of molten carbon pitches in contact with air flow inside it. In order to determine proper experimental set up dimensions and air flow conditions for the selected droplet and track properties, numerical simulation of the process has to be conducted.

4.1 Numerical simulation of the flow in the air-pitch reaction zone of the NGJ nozzle

The problem is described as a steady-state flow impinging at a free molten pitch surface in an infinitely wide rectangular channel at 30^o and 45^o (Figure 1-1). It represents a two-scale problem, where the pressure drop along the channel and air jet temperature was used to solve Navier-Stokes equations coupled with continuity and energy equations applying FVM. In order to model the NGJ process and compare experimental results with the BSM simulation of Stokes flow about deformable liquid droplets and tracks discussed in Chapter V, a preliminary flow field of initially unperturbed surface for the whole domain was computed with FVM (Figures 4-1 and 4-2). At the second stage, the resulting cell-based Reynolds number, were computed along the horizontal line located at 10 μm from the bottom Figures 4-1. Finally, the location of low Reynolds number region ($Re<1$) was found (Figure 4-3) and used as a droplet placement region for experimental

and numerical simulations. The micro-scale pitch ripple (liquid track) size is assumed to be $D \cong 3 \div 5\ \mu m$, which is 10 times greater than mean submicron fiber diameter derived [87].

The macroscale flow problem in a whole domain of 1mm long and 0.25 mm high of NGJ channel reaction zone is described as viscous compressible jet flow impinging at a lower surface. The inlet velocity is 250 m/s and the temperature is 480℃.

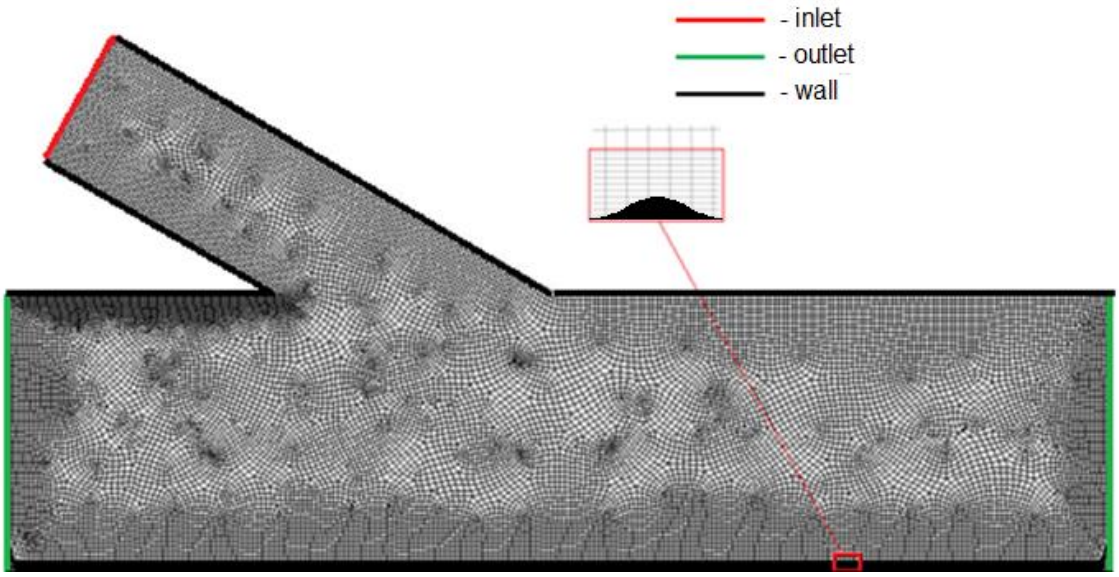

Figure 4-1 Unstructured grid in ANSYS Fluent with 10-layer inflation on the bottom surface.

For the purpose of initial velocity vector field computation in the overall domain, a 2-D channel model meshed with unstructured grid and the bottom surface inflation were created (Figure 4-1). Specified mesh resulted in 23213 nodes and 22746 elements including the 10-layer inflation zone.

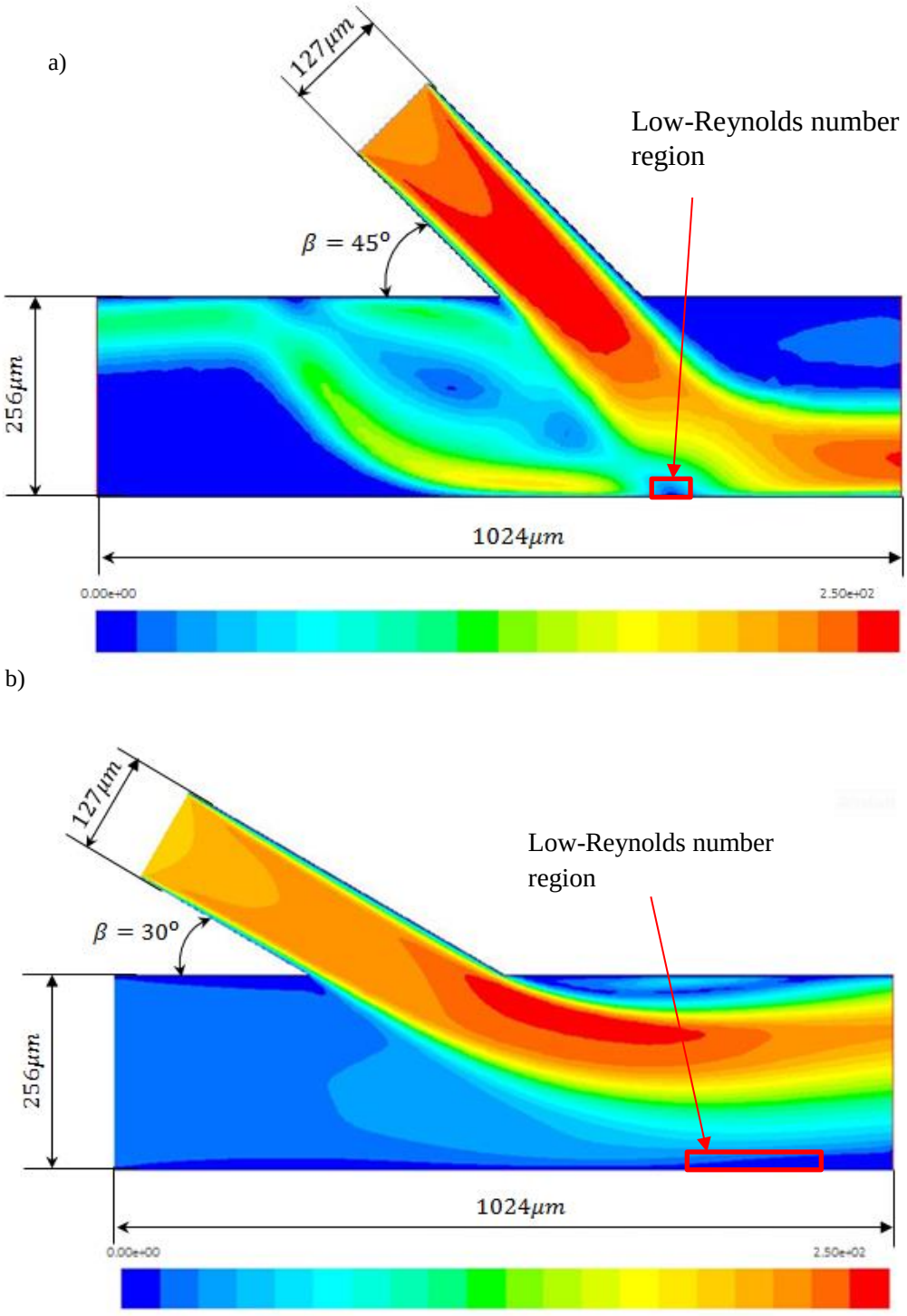

Figure 4-2 ANSYS Fluent solution for velocity magnitude contours for the air jet flowing into the reaction channel at: a) 45 degrees; b) 30 degrees.

Although reasonable refinement of the grid and more accurate flow prediction in the droplet deposition region is possible, the resulting grid is not fine enough for accurate computation of the velocity and stress components about the droplet itself. Each layer thickness in the inflation zone was equivalent to $1\mu m$, while considered droplet size was 3.5 μm and therefore it requires refinement for accurate prediction of the flow field, stress and deformation computations of the droplet. However, this leads to a significant computation time increase.

The fluid flow model was selected based on Reynolds number for the real case flow in the channel has been calculated based on the characteristic dimension of the channel and inlet velocity. The air jet was calculated equal to $Re \approx 2850$, which relates it to transition flow regime. In the present computations, low-Reynolds $k-\varepsilon$ flow model was selected to find the solution of the air flow velocity in the overall domain. The resulting FVM solution is presented in Figure (4-2).

Once computed, the local Reynolds numbers (Figure 4-3) throughout the domain are determined and the low-Reynolds number ($Re_d \leq 1$) regions are then found using (4-1).

Based on the air flow data in the NGJ process, the air flow speed during the experiment was tuned such that local Reynolds number based on droplet characteristic size was less than or equal to unity:

$$Re_D = \frac{\langle U_{local_1} \rangle R_{droplet_1}}{\nu_{air_1}} = \frac{\langle U_{local_2} \rangle R_{droplet_2}}{\nu_{air_2}} \leq 1, \qquad (4\text{-}1)$$

which yields to:

$$\langle U_{local_1} \rangle \leq \frac{\nu_{air_2}}{\nu_{air_1}} \frac{U_{local_1} R_{droplet_1}}{R_{droplet_2}}, \tag{4-1a}$$

where $\langle U_{local_1} \rangle$, and is the average local velocity across the low Reynolds number region (Figure 4-3) in vicinity of stagnation region of the real NGJ nozzle obtained from FVM simulation (see Figure 4-2). $R_{droplet_1}$ is a liquid pitch ripple radius and ν_{air_1} is the air viscosity taken at $T_1 = 400$℃ and $p_1 = 4.76atm$. Consequently, $\langle U_{local_2} \rangle, R_{droplet_2}$ and ν_{air_2} are the values taken at $T_2 = 20$℃ and $p_2 = 1atm$ for deformation simulations.

The low-Reynolds number region for the case of 45° coincides with the stagnation region where jet impinges the wall, as shown in the Figure 4-2a.

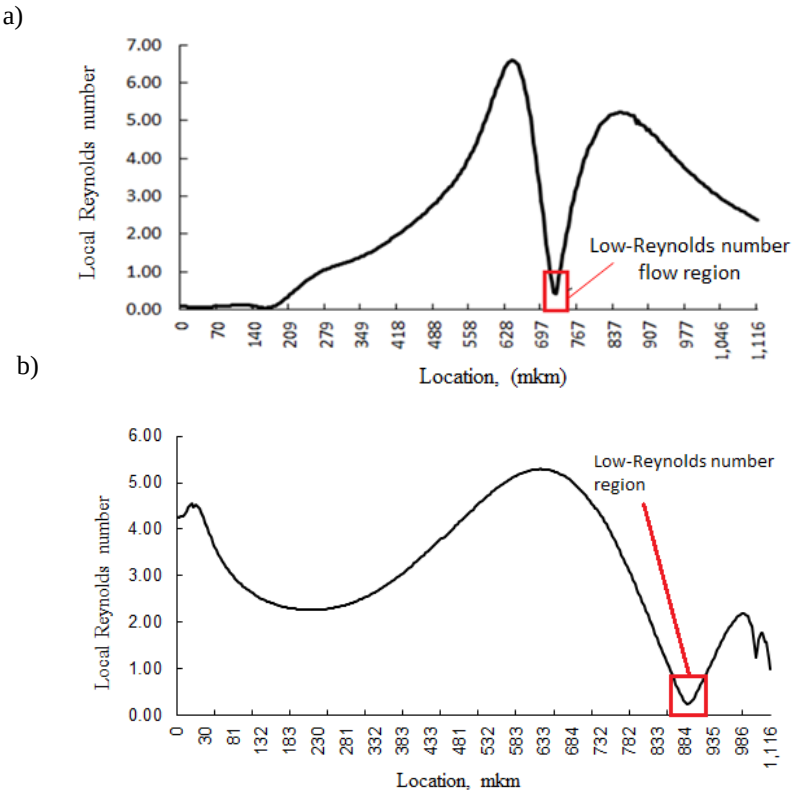

Figure 4-3 Local Reynolds numbers at 10 μm from surface of the 1116 × 256 μm domain with air inlet flow orientation: a) 45 degrees; b) 30 degrees.

Local Reynolds number data (Figure 4-3) were further used to determine the boundaries of the low-Reynolds number flow domain for subsequent BSM simulation to maintain applicability conditions. Then velocity flow field, magnitude and local Reynolds number regions found with ANSYS Fluent simulation were used determine appropriate experimental set up scaling factor and similarity conditions that will be discussed in the next Section.

4.2 Experimental set up and justification of the scale-up model

For experimental purposes, the apparatus presented in Figure 4-4 was designed and built to study viscous droplets and tracks deformation in reaction with an impinging air flow in the channel at different flow angles with respect to the channel bottom.

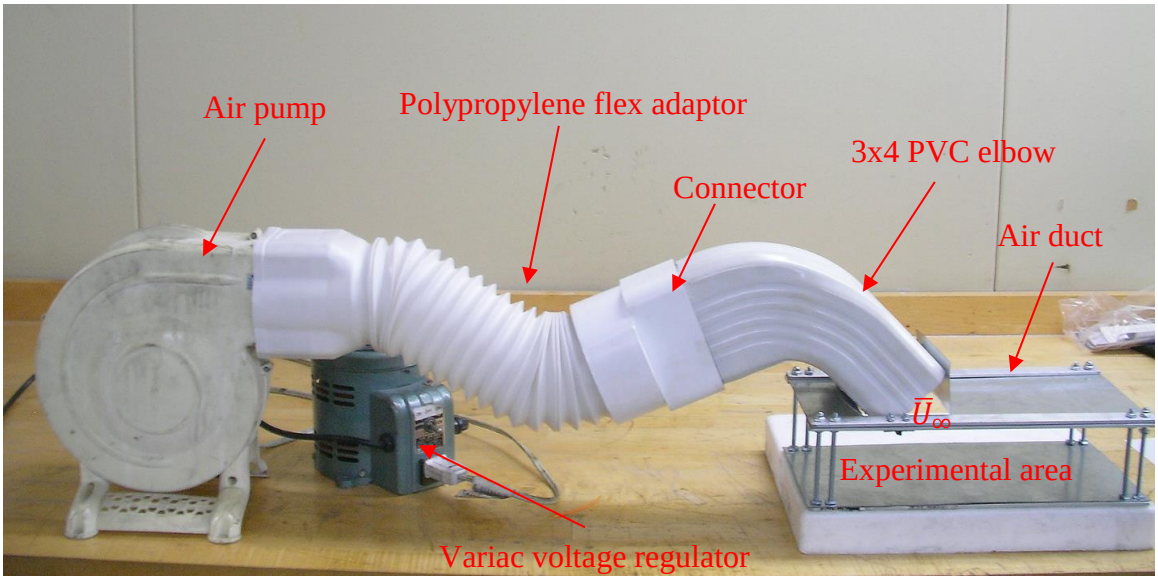

Figure 4-4 Experimental set up for tracks and droplets deformation study

Polydimethylsiloxane (PDMS) was selected as a sampling material for the experiment conducted in the room conditions. It has viscous properties similar to those of molten mesophase pitch at operation temperatures ($T_{pitch} = T_{air} 380 \div 400℃$) and air flow conditions in the NGJ nozzle reaction zone, which will be discussed later in this Section.

For better experimental results visualization, the initial NGJ channel "air-liquid" reaction area was designed similar to NGJ experimental set up and scaled by factor $m = 300$, which gives the dimensions depicted in Figure 4-5. "1" and "2" in Figure 4-5 designate droplet and track deposition lines for 45 and 30 degrees air flow orientation respectively.

The experimental set up includes assembly of the air supply line from air pump to the aluminum experimental channel via polypropylene flexible adapter, styrene connector and 3x4 inch PVC elbow. The latter is attached to the testing channel inlet lips (Figure 4-5) and sealed from the sides before experiment.

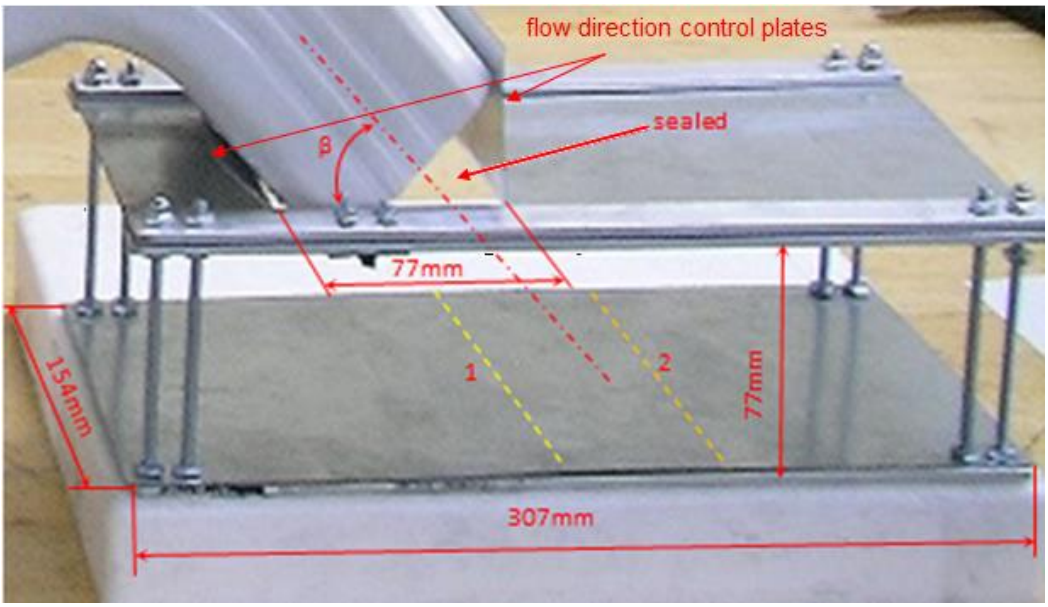

Figure 4-5 Experimental testing zone dimensions.

The angle β between the elbow and channel surface allows adjusting the air flow orientation to model respective flow case as per Figure 4-2 in the previous Section.

The centrifugal air pump was then plugged to a Variac voltage regulator to control air flow speed. It was derived from dynamic pressure measured with an inclined manometer connected to an elbow channel via static pressure port at the bottom (Figure 4-6a) and to a pitot tube mounted under the top channel surface to measure total pressure at the elbow outlet (Figure 4-6b).

a) b)

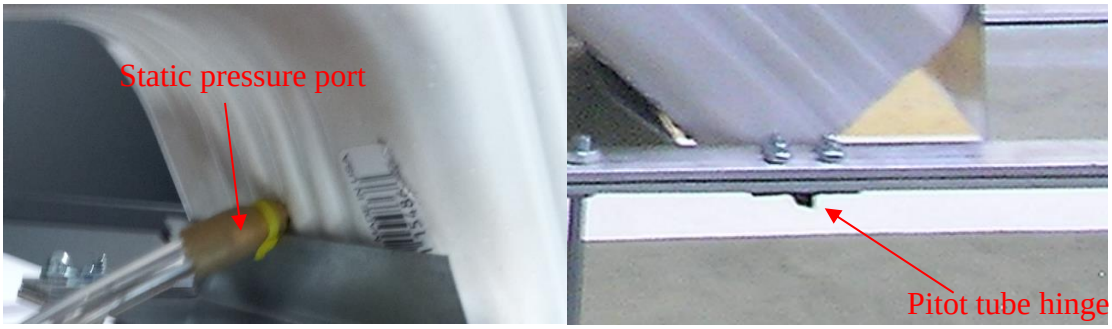

Figure 4-6 Static pressure measurement port and Pitot tube hinge.

The dynamic sequence of the experiment steps is the following. Air is supplied by the centrifugal pump and discharged though the duct into the rectangular channel, where viscous PDMS droplets and tracks were placed for each particular air flow orientation.

MicroLubrol 200 silicone oil was selected for the liquid droplet/track sample deformation tests. It represents PDMS with apparent viscosity 1000 cSt or 0.965 $Pa \cdot s$ [83]. The local velocity of the air flow about 1mm size droplet in low-Reynolds number region needed for the experiment was found from the condition (4-1). The equivalent

velocity magnitude near liquid pitch ripple in the NGJ apparatus $\langle U_{local_1} \rangle = 6.5 \frac{m}{s}$ was found from 2-D flow FV simulation results in ANSYS Fluent for the real NGJ process presented in Section 4.1:

$$\langle U_{local_2} \rangle \leq \frac{1.5328 \cdot 10^{-5}}{1.3384 \cdot 10^{-5}} \cdot \frac{6.5 \cdot 3.5 \cdot 10^{-6}}{10^{-3}} \leq 0.026 \frac{m}{s}.$$

The air speed at the inlet of the air duct in the experiment was controlled by the Variac voltage regulator, and the dynamic pressure was measured using inclined pressure manometer. The velocity was then computed as:

$$U_\infty = \sqrt{\frac{2\Delta p}{\rho_{air}}}, \tag{4-2}$$

where Δp is a difference between total and static pressure measured across the duct of the rectangular channel. To have average local velocity $\langle U_{local_2} \rangle = 0.026 \frac{m}{s}$ and satisfy condition (4-1) approximately, the velocity in the air duct of the experimental set up had to be $U_\infty = 6.3$ m/s, which follows from the condition (4-1) and has been found in ANSYS FLUENT using geometry of the scaled up NGJ channel. The resulting FVM solutions gave $\langle U_{local_2} \rangle$ values ranging from ~0.03 m/s for 45^o impinging air stream down to ~0.025 m/s for 30^o degrees oriented air stream, which results in $Re_{D_{45^0}} \cong 1$.

The following experimental conditions had to be met:

1) The multiphase flow process in the gas-liquid reaction area is isothermal ($T_{air} = T_{gas} = T_{surface}$);

2) The size of the liquid droplet or track and velocity have to be small enough so that local Reynolds number is less than or equal to unity ($Re_D \leq 1$). That is droplet height $h \leq 1mm$.

Another criterion that helps to evaluate equivalent of test droplet and liquid track deformation compared to real NGJ process is a dimensionless time. It can be expressed with the equation (4-3):

$$\bar{t} = \frac{tU_\infty}{R}\frac{\mu_g}{\mu_l}, \tag{4-3}$$

where μ_g and μ_l are gas and liquid dynamic viscosities.

The first two conditions have to be satisfied in order to make experimental results comparable to the ones obtained with BSM. According to (4-3), the real NGJ experiment simulation time for the estimated flow conditions (see Section 4.1) is:

$$\bar{t}_{pitch} = \frac{1s \cdot 14.4776\frac{m}{s}}{10^{-6}m} \cdot \frac{3.4 \cdot 10^{-5} Pa \cdot s}{100\ Pa \cdot s} \cong 5.$$

For the air flow conditions found during the experiment and computed for the reaction zone near PDMS droplet deposition lines, the dimensionless deformation time becomes:

$$\bar{t}_{PDMS} = \frac{1s \cdot 0.026}{0.001} \cdot \frac{1.5328 \cdot 10^{-5}}{0.001} \cong 0.4,$$

depending on the angle of the air flow orientation. These two values computed for two different liquids show that the same relative deformation of liquid droplet or track with respect to their size would take approximately 12.5 times longer for those made from PDMS than those from carbon mesophase pitch in the real NGJ apparatus.

The specified above dimensionless time values were obtained for the considered liquids in respective air flow conditions, channel dimensions and fluid properties. The duration of each run for both the 3-D droplet and the 2-D liquid track deformation experiment was 2÷3s.

It has to be mentioned that $\frac{\mu_{air}}{\mu_{pitch}}$ ratio in (4-3) plays a significant role in the equivalent deformation time estimate for various liquid media in a gas flow and determines the quantitative measure of deformation derived from the constitutive equation, which will be discussed in the next Chapter. The ratio of viscosities together with the measured duct inlet velocity magnitude U_∞ has been used in the experimental part to justify selection of the pitch prototype liquid material to model real NGJ process in the nozzle with carbon mesophase pitch.

In order to determine validity of a Newtonian fluid model selected for further simulations and comparison with the experimental results, one has to ascertain that viscosity is nearly invariable of shear rate values taking place in both real NGJ process and its' prototype for the respective materials. The interface boundary condition at the droplet surface during the process comprises of equality of shear stresses arising from both gas flow and liquid motion due to drag induced, which yields:

$$-\mu_g \frac{\partial \vec{u}_g}{\partial \vec{n}} = -\mu_l \frac{\partial \vec{u}_l}{\partial \vec{n}}, \tag{4-4}$$

The resulting shear rate of a liquid droplet at a gas-liquid interface becomes:

$$\frac{\partial \vec{u}_l}{\partial \vec{n}} = \frac{\mu_g}{\mu_l} \frac{\partial \vec{u}_g}{\partial \vec{n}}, \tag{4-5}$$

Using Eq.15 from the previous Section it was found:

$$\dot{\gamma}_{PDMS} = \frac{\mu_{air}}{\mu_{PDMS}} \dot{\gamma}_{air} \cong 360 \div 500\ s^{-1},$$

Here local $\dot{\gamma}_{air} = \frac{\partial \vec{u}_{air}}{\partial \vec{n}}$ was the maximum shear rate evaluated at the liquid surface. This value for the low-Reynolds number flow region has not been measured but calculated in ANSYS Fluent, where previously measured velocity in the channel duct was set as the inlet boundary condition for a 2-D channel model. It is worthwhile to mention that the specified shear rate values were estimated particularly for low-Reynolds number flow regions of the test channel and correspond to the flow orientation range from 30^{o} to 45^{o}.

Similarly to the fluid viscosities ratio, determination of a shear rate at the liquid boundary is important for the deformation of droplet modeling and for comparison of numerical simulations with the obtained experimental results.

PDMS suited well for the scaled-up experiment of the NGJ process in terms of shear rates required for the Newtonian fluid model assumption and the dimensions of the flow channel. The respective liquid shear rate values must be lying within a range of Newtonian fluid model with invariable viscosity. The resulting shear rate at a surface of PDMS must be within the range of linear apparent dynamic viscosity values (Figure 4-7), which can be determined using (4-5).

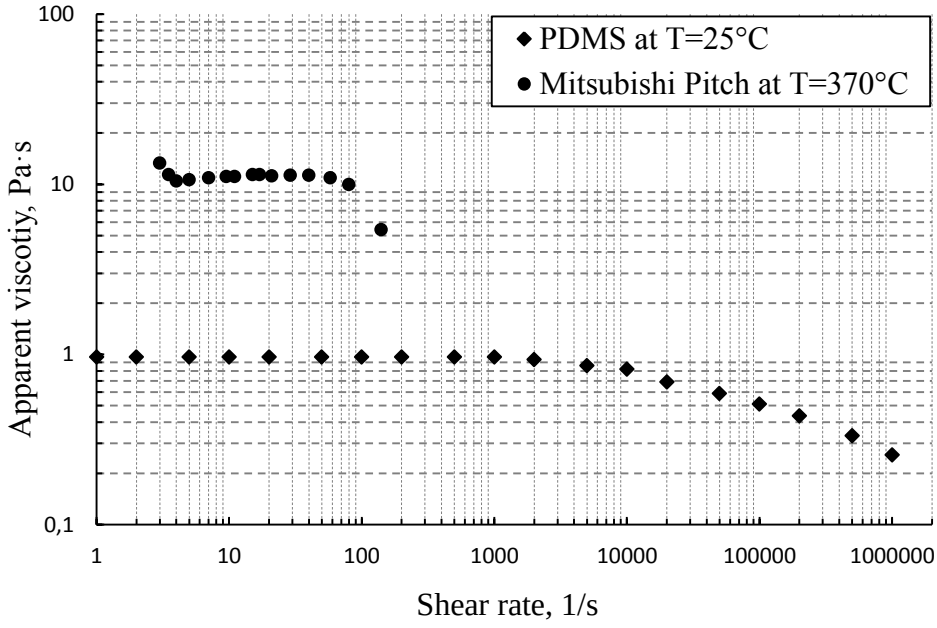

Figure 4-7 Apparent dynamic viscosity versus shear rate for PDMS [83] and Mitsubishi mesophase pitch [84].

In the real case for ARA24r Mitsubishi carbon mesophase pitch (assuming it to be material with similar behavior to GrafTech mesophase pitch at $T \geq 380^{\circ}\mathrm{C}$):

$$\dot{\gamma}_{pitch} = \frac{\mu_{air}}{\mu_{pitch}} \dot{\gamma}_{air} \cong 36 \div 50\ s^{-1},$$

This estimate justifies application of Newtonian fluid stress model in constitutive equation for calculation of the corresponding deformation at each point of an "air-liquid" interface.

4.3 Experimental results and discussion

As a result of the proposed experiment, a set of photographs of PDMS droplets and tracks deformation were obtained for two different angles of air flow that was supplied to the reaction zone of the testing channel (Figure 4-8). In order to evaluate results quantitatively, a special $1mm$ scale was installed along the deposition lines of the reaction zone.

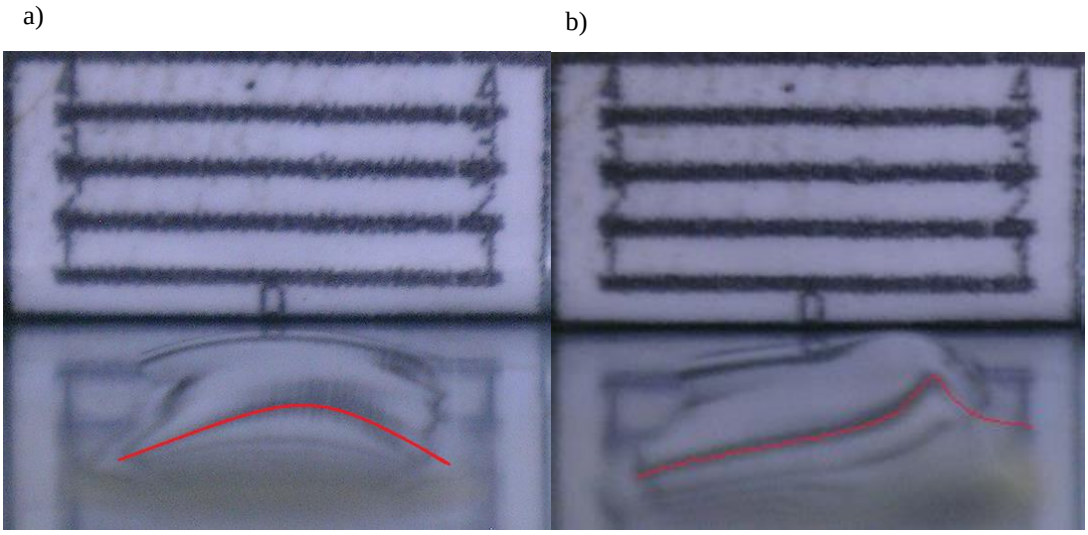

Figure 4-8 Change of shape of a PDMS 2-D track placed in a low-Reynolds number region: before and after its' deformation under the air jet discharged into the rectangular channel at 30 degrees: a) initial profile; b) deformed surface after 2s.

The scale lines depicted in Figures 4-8 – 4-11 have dual purpose: they help to evaluate the size of a PDMS track or droplet and their distorted reflection from the semi-transparent surface shows initial and deformed profile that can be compared with the numerical simulation results.

Figures 4-8 and 4-9 let one notice reflection of the scale lines at the surface of deformed PDMS 2-D tracks and recognize initial and resulting shapes of a transparent sample. It is also possible to see that the height of the track peak increases and moves to the right with the flow in case air flow oriented at 30° to the channel bottom. Further deformation at later times was not tracked and studied since samples leaved low-Reynolds number flow region and the results are not comparable to the deformation profiles computed with BSM.

a) b)

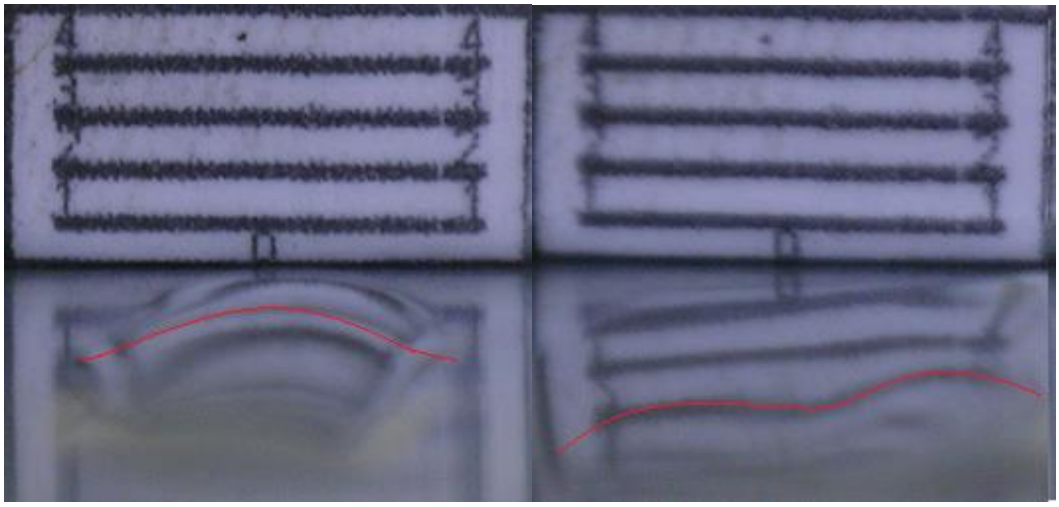

Figure 4-9 Change of shape of a PDMS 2-D track placed in a low-Reynolds number region: before and after its' deformation under the air jet discharged into the rectangular channel at 45 degrees: a) initial profile; b) deformed surface after 2s.

At the 45-degree air flow, the 2-D liquid track is being smeared over the bottom of the channel and finally split in two parts both sides of the flow stagnation line. Contrary to the 30º air flow orientation case, the height of a track sample decreases, which can be observed in Figures 4-9.

a) b)

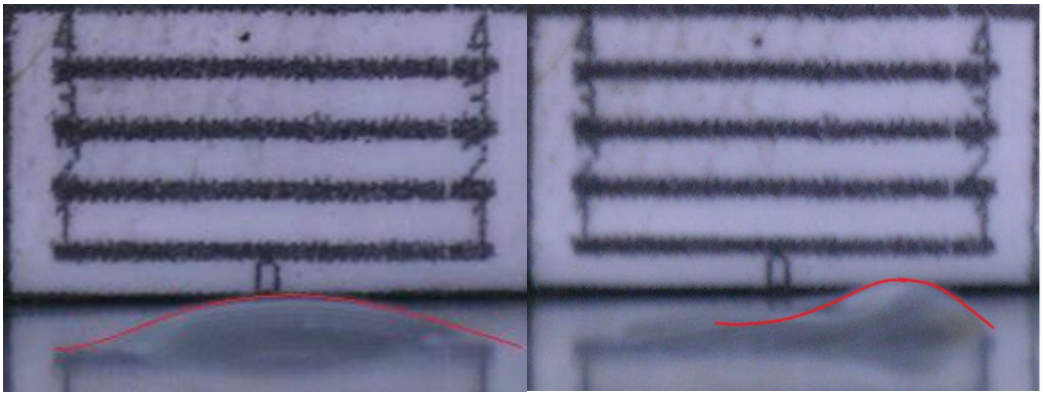

Figure 4-10 Change of a PDMS droplet shape of a droplet placed in a low-Reynolds number flow region after its' deformation under the air jet discharged into the rectangular channel at 30 degrees: a) initial profile; b) deformed surface after 2s.

a) b)

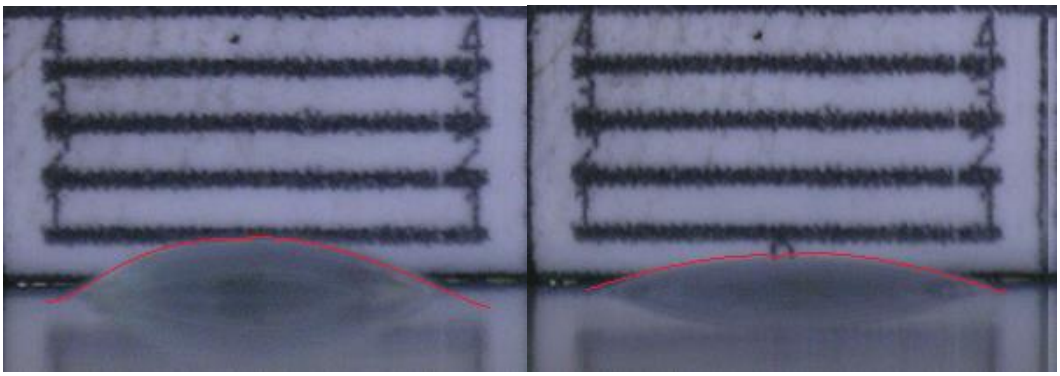

Figure 4-11 Change of a PDMS droplet shape of a droplet placed in a stagnation point after its' deformation under the air jet discharged into the rectangular channel at 45 degrees: a) initial profile; b) deformed surface after 2s.

4.4 Experimental uncertainty analysis and error estimate

In order to evaluate the obtained results quantitatively, error estimate was conducted assuming the following contributing factors:

a) imaging parallax error estimate;

b) linear measurements uncertainty and

c) deformation time error estimate.

The parallax (Figure 4-12) observed for imaging of the droplet deformation in the present experiment was calculated according to the principles explained in [85]. The resulting error can also be found from geometric relationships using Figure 4-12.

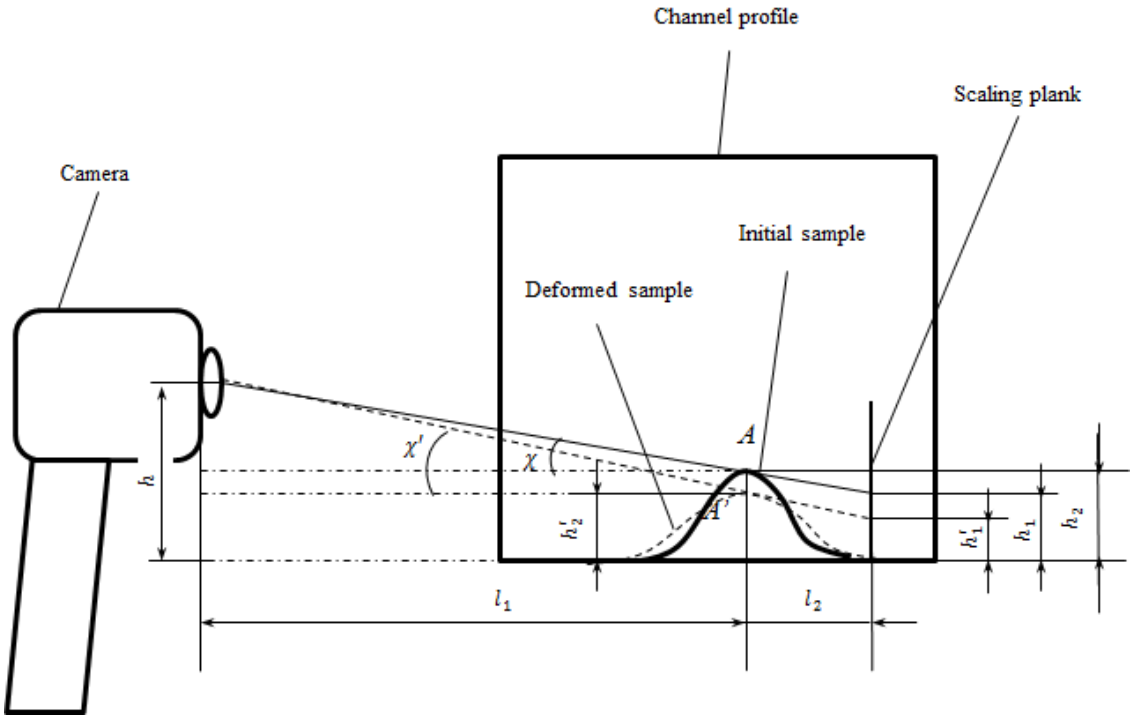

Figure 4-12 Imaging scheme and parallax determination parameters.

It easy to notice that h, l_1 and l_2 are known pre-determined distances. They were measured every time before the experiment and after the droplet or track deposition. h_1 is the droplet or track height, which is read from the photograph in the place of deformation observation. The elevation of the camera objective above channel surface h is assumed to

be constant, while distances from the camera to the observation point A on a sample droplet or track and l_1, distance from the observation point at a sample surface to the scale plank and initial droplet height h_2 depend on each particular test run. At the end of the experiment, the true and observed sample heights are $h_2{}'$ and h_1' respectively. It was noticed that the distance from the camera to an observation point at a sample surface was almost the same during the experiment. Therefore, l_1 and l_2 were assumed constant.

The analysis of uncertainty of the experimental results visualization was performed based on calculated of the difference between initial droplet/track heights calculated from the angle χ and between deformed droplet/track surfaces that is observed at the angle χ' in Figure 4-12:

$$\begin{cases} \varepsilon = h_2 - h_1 \\ \varepsilon' = h_2{}' - h_1{}' \end{cases} \tag{4-6}$$

Observation line is tangent to a sample surface before and after deformation in points A and A' respectively (Figure 4-12). Due to small change of height of the sample, it is assumed that are located at the same vertical line and therefore l_1 and l_2 are invariant during experiment for each particular test. On another hand, the total uncertainty also depends on inaccuracy in deformation time measurement. Moreover, for the liquid surface deformation the rate of change of deformation is critical. It also allows accounting for time measurement uncertainty together with the displacement error.

The total uncertainty ε_Σ is determined as follows:

$$\{h_1, h_1', l_1, l_2, h\} \rightarrow \begin{cases} \begin{cases} \varepsilon \\ \varepsilon' \end{cases} \\ \{t_0, t_1\} \end{cases} \rightarrow \begin{cases} \varepsilon_d \\ \varepsilon_d' \end{cases} \rightarrow \varepsilon_\Sigma, \tag{4-7}$$

where

$$\varepsilon_d = \frac{h_2 - h_1}{t_1 - t_0} \quad \text{and} \quad \varepsilon_d' = \frac{h_2' - h_1'}{t_1 - t_0}. \tag{4-8}$$

Using formulas in [86] or deriving trigonometric relations for angles χ and χ' from Figure 4-11 it is possible to calculate h_2 and $h_2{}'$ to find parallaxes ε and ε_1:

$$\tan\chi = \frac{h - h_2}{l_1} = \frac{h_2 - h_1}{l_2} \quad \text{and} \quad \tan\chi' = \frac{h - h_2'}{l_1} = \frac{h_2' - h_1'}{l_2}, \tag{4-9}$$

which yields:

$$h_2 = \frac{hl_2 - h_1 l_1}{l_1 + l_2} \quad \text{and} \quad h_2' = \frac{hl_2 - h_1' l_1}{l_1 + l_2}. \tag{4-10}$$

Substituting (4-10) into (4-6):

$$\varepsilon = \frac{hl_2 - h_1(2l_1 + l_2)}{l_1 + l_2};\ \varepsilon' = \frac{hl_2 - h_1'(2l_1 + l_2)}{l_1 + l_2}. \tag{4-11}$$

The partial derivatives of absolute error over the set of parameters are as follows:

$$\begin{bmatrix} \frac{\partial\varepsilon}{\partial l_1} = -\frac{(h_1 + h)l_2}{(l_1 + l_2)^2}, \\ \frac{\partial\varepsilon}{\partial l_2} = \frac{(h + h_1)l_1}{(l_1 + l_2)^2}, \\ \frac{\partial\varepsilon}{\partial h_1} = -\frac{2l_1 + l_2}{(l_1 + l_2)} \\ \frac{\partial\varepsilon}{\partial h} = \frac{l_2}{(l_1 + l_2)}, \end{bmatrix} \quad \text{and} \quad \begin{bmatrix} \frac{\partial\varepsilon'}{\partial l_1} = -\frac{(h + h_1')l_2}{(l_1 + l_2)^2}, \\ \frac{\partial\varepsilon'}{\partial l_2} = \frac{(h + h_1')l_1}{(l_1 + l_2)^2}, \\ \frac{\partial\varepsilon'}{\partial h_1'} = -\frac{2l_1 + l_2}{(l_1 + l_2)}, \\ \frac{\partial\varepsilon'}{\partial h} = \frac{l_2}{(l_1 + l_2)}. \end{bmatrix} \tag{4-12}$$

These expressions represent two groups of four parameters each: $d = \{l_1, l_2, h\ and\ h_1$ or $h_1'\}$. Applying well-known relation for the uncertainty propagation, we have:

$$\varepsilon_{\Sigma_1} = \sum_{i=1}^{4}\left(\varepsilon_{d_i}\frac{\partial\varepsilon}{\partial d_i}\right)^2 + \phi^2;\ \varepsilon_{\Sigma_2} = \sum_{i=1}^{4}\left(\varepsilon'_{d_i}\frac{\partial\varepsilon'}{\partial d_i}\right)^2 + \phi^2, \tag{4-13}$$

where ε_{d_i} and ε'_{d_i} are uncertainties determined for each parameter d_i and ϕ^2 is omitted since each test case was set up individually for different liquid droplet or track sample.

According to the National Institute of Standards and Technology, the metal ruler uncertainty used is:

$$\varepsilon_{d_i} = \left(27 + 0.88d_i\right)\mu m. \tag{4-14}$$

The calculated distance from camera to the observation plane is $l_1 = 150$ mm. Therefore, $\varepsilon_{l_1} = 2.713 \cdot 10^{-5}$m. Similarly, for $l_1 = 12.5$ mm, the uncertainty for l_2 as well as for the rest of length parameters measured with a metal ruler was found equal to $\varepsilon_{l_2} \approx \varepsilon_h \approx \varepsilon_{h_1} \approx \varepsilon_{h'_1} = 2.7 \cdot 10^{-5}$ m. Time measurement error for t_0 and t_1 falls within 0.1s, and therefore $\varepsilon_{t_1} = \varepsilon_{t_0} = 0.05s$.

Combining (4-6) and (4-8), it is reasonable now to re-write the expressions for the rate of change of strain observation errors as follows:

$$\varepsilon_d = \frac{\varepsilon}{t_1 - t_0} \quad \text{and} \quad \varepsilon'_d = \frac{\varepsilon'}{t_1 - t_0}. \tag{4-15}$$

Taking derivative of (4-15) one obtaines:

$$\begin{cases} \frac{\partial\varepsilon_d}{\partial\varepsilon} = \frac{1}{t_1 - t_0}, \\ \frac{\partial\varepsilon_d}{\partial t_0} = \frac{\varepsilon}{(t_1 - t_0)^2}, \\ \frac{\partial\varepsilon_d}{\partial t_1} = -\frac{\varepsilon}{(t_1 - t_0)^2} \end{cases} \text{and} \begin{cases} \frac{\partial\varepsilon'_d}{\partial\varepsilon'} = \frac{1}{t_1 - t_0}, \\ \frac{\partial\varepsilon'_d}{\partial t_0} = \frac{\varepsilon'}{(t_1 - t_0)^2}, \\ \frac{\partial\varepsilon'_d}{\partial t_1} = -\frac{\varepsilon'}{(t_1 - t_0)^2}. \end{cases} \tag{4-16}$$

Using the parallax determination uncertainties given in (4-13), the total uncertainty of measure and calculated droplet deformation height becomes:

$$\varepsilon_{\Sigma} = \sqrt{\left(\varepsilon_{\Sigma_1}\frac{\partial \varepsilon_d}{\partial \varepsilon}\right)^2 + \left(\varepsilon_{t_0}\frac{\partial \varepsilon_d}{\partial t_0}\right)^2 + \left(\varepsilon_{t_1}\frac{\partial \varepsilon_d}{\partial t_1}\right)^2 + \left(\varepsilon_{\Sigma_2}\frac{\partial \varepsilon_d}{\partial \varepsilon'}\right)^2 + \left(\varepsilon'_{t_0}\frac{\partial \varepsilon'_d}{\partial t_0}\right)^2 + \left(\varepsilon'_{t_1}\frac{\partial \varepsilon'_d}{\partial t_1}\right)^2} \quad (4\text{-}17)$$

For PDMS droplet deformation experiment results presented in Figure 4-12, the parameter values were taken as follows: $h = 0.025$ m, $h_1 = 0.001$ m, $h'_1 = 5 \cdot 10^{-4}$ m, $l_1 = 0.15$ m, $l_2 = 0.0125$ m, $t_0 = 0$, $t_1 = 2s$. Using these parameters in (4-16) and then plugging the resulting values into (4-13) together with (4-14) computed for each parameter yields $\varepsilon_{\Sigma} = 5.012 \cdot 10^{-2} mm$.

It is seen that visualization of PDMS droplets and tracks deformation for this particular experimental set up has a significant parallax, which leads to total error reaching 50% and more. Therefore, the uncertainty analysis and error estimate of the visualized experimental results was based on computed h_2 and h'_2 values representing real heights of droplet or track before and after experiment. This allows avoiding introduction of parallax into the general uncertainty and measurement error estimate.

Numerical simulation results presented in Chapters V and VI is only compared qualitatively to the deformation profile images presented in this Chapter. The idea of this comparison is to demonstrate liquid surface development trends depending on the air flow orientation and to show capabilities of the proposed numerical algorithms to predict such deformations.

CHAPTER V

APPLICATION OF THE BOUNDARY SINGULARITY METHOD TO QUASI-STEADY TWO-DIMENSIONAL PROBLEMS OF VISCOUS DEFORMATION IN STOKES FLOWS

The physics of NGJ ([87], Figures 1-1 and 1-2) is generally represented by turbulent flow about a viscous molten carbon mesophase pitch surface at a high temperature. According to the experimental data, this temperature was 30 – 50 ℃ higher than the pitch melting point [87]. The molten carbon mesophase pitch exemplifies a non-Newtonian fluid in general. However, Dumont et al showed in [84] that carbon mesophase pitch may have nearly Newtonian properties for a certain range of shear rates at which viscosity remains almost the same. The experiments conducted in the Polymer Research & Engineering Center of the University of Akron [52] show that for the range of shear rates $30 \div 200\ s^{-1}$ Mitsubishi [84] and GrafTech carbon mesophase pitches exhibit Newtonian fluid properties at their respective operating temperatures. For the specified shear rates, the viscosity remains nearly constant. Furthermore, based on experiments in the NGJ lab, a shear-thinning effect for even higher shear rates (over $100\ s^{-1}$) is predicted for GraphTech mesophase pitch. This improved spreading of the pitch flow across the fiber manufacturing rectangular nozzle and helped against deceleration of the pitch flow in supply channels, manifolds and nozzle clogging. The

assumption of quasi-Newtonian molten pitch properties represents basis of the physical model of deformation of droplet based on evaluation of shear stress for the considered problem.

The proposed FVM and BSM coupling approach is presented and applied in Chapters V and VI for numerical simulation of a multiphase quasi-steady problem that represent idealized 2-D and 3-D models of the flow inside the reaction zone of the NGJ nozzle.

These models must be considered as a coarse attempt to describe a physically complex process associated with the deformation of a liquid surface under impinging high-speed jet discharged into a narrow channel. In fact, other sophisticated effects, such as recirculation in vicinity of the liquid surface perturbation, jet reflections and heat transfer problems across the boundary layer adjacent to the surface need to be accounted for. These effects, however, have been neglected in the simplified formulation presented here for limitation of the problem complexity. It is less likely to find Reynolds numbers less than 1 for high speed flows even in stagnation zones of the slit channel. Besides, the problems discussed in Chapters V and VI are solved for single liquid droplets and tracks settling on a rigid non-deformable surface, while in reality the droplet or track represent continuous wave or ripple on a liquid film surface, which is also constantly exposed to the air flow.

Therefore, obtained numerical solution for the viscous deformation under impinging air flow in a stagnation zone of the channel where $Re \leq 1$ may serve as a rough estimate of an evolution of a single liquid droplet or track surface shape for the

different flow impingement angles. However, they also represent a good opportunity to test numerical methods and to understand simplified basics of correlation between different flow conditions and corresponding changes in viscous deformation profiles using capabilities of BSM, the proposed coupling method and algorithms discussed here.

5.1 Introduction of regularized BSM for the problems of the Stokes flow in a channel

In order to validate the method applicability to more complex problems of the Stokes flow about deformable liquid surfaces, a 2-D problem of pressure-driven flow in the micro-channel was computed.

The initial geometric and physical formulation of the problem is similar to the one presented by Cortez [34] and in semi-circle droplet viscous deformation problem formulated by Fry in Chapter 8 of [88]. For the problem presented in [34], the size of 2-D rectangular domain was taken 1-by-0.05 (Figure 5-1) and the semicircular obstacle radius was taken 0.0125. The problem setup for comparison with [88] is presented in Figure (5-9). The same geometry was used for simulations in Section 5.2.

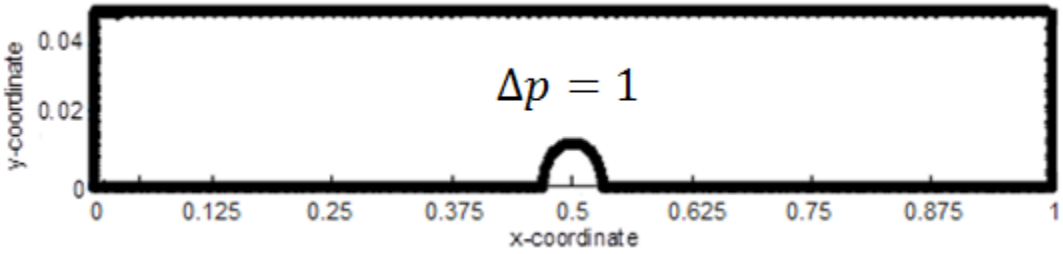

Figure 5-1 Problem set up as per [34]

Henceforth, a quasi-steady algorithm for deformation simulations has been applied and the surface coordinates are updated at each time step as suggested later in Section 5.2 and used further in Chapters V and VI.

Viscous deformations at a surface point induced by impinging air jet were found here from shear stress computed for a respective elementary surface area based on velocity solution. In Chapter V, 2-D class of viscous deformation problems was considered and solved using Stokeslet regularization technique for BSM presented in [34]:

$$u_{\epsilon_j}^{(k)} = -\frac{1}{4\pi\mu}\sum_{i=1}^{N}\left(F_i^{(k)} \ln\left(\sqrt{|\tilde{r}|^2+\epsilon^2}+\epsilon\right) - \frac{\left(\sqrt{|\tilde{r}|^2+\epsilon^2}+2\epsilon\right)\left(F_i^{(k)}\left(\epsilon\sqrt{|\tilde{r}|^2+\epsilon^2}+\epsilon^2\right)+F_i^{(m)}\tilde{r}_{ij}{}^k\tilde{r}_{ij}^m\right)}{\left(\sqrt{|\tilde{r}|^2+\epsilon^2}+\epsilon\right)^2\sqrt{|\tilde{r}|^2+\epsilon^2}} \right), \qquad (5\text{-}1)$$

$$p_{\epsilon_j} = \frac{1}{2\pi}\sum_{i=1}^{N} F_i^{(m)}\tilde{r}_{ij}{}^k \frac{\epsilon\sqrt{|\tilde{r}|^2+\epsilon^2}+2\epsilon^2+|\tilde{r}|^2}{\left(\sqrt{|\tilde{r}|^2+\epsilon^2}+\epsilon\right)^2(|\tilde{r}|^2+\epsilon^2)^{\frac{3}{2}}}$$

where $u_{\epsilon_j}^{(k)}$ and p_{ϵ_j} are regularized velocity and pressure fundamental solutions in 2-D notation. F is a vector of Stokeslets, which is determined as discussed in the Section 2.1 of the Chapter II. Shear stress can be found as a normal derivative of the velocity vector obtained with (5-1):

$$\bar{\tau} = -\bar{\mu}_l \frac{\partial \vec{u}}{\partial \hat{n}} = \bar{\mu}_l \frac{-4\bar{u}_{r_2}+3\bar{u}_{r_1}}{2\Delta\bar{r}}, \qquad (5\text{-}2)$$

where $\bar{u}_{r_2}$ is a total normalized velocity magnitude at a two-layer distance $2\Delta r$ from the surface and $\bar{u}_{r_1}$ is a velocity at one-layer distance surface, and $\bar{u}_{r_0} = 0$ due to no-slip and no-penetrating boundary conditions. This formula represents $O(\Delta\bar{r}^2)$ accurate finite difference presented in [89].

The resulting solution for velocity vector field, streamlines, shear and normal stresses was determined and compared to the one obtained with the Method of Regularized Stokslets by Cortez in [34] and by Gaver and Kute in [90] that solved the problem numerically applying boundary element method to algebraic relations derived from the governing equations in lubrication theory. Additional solution of the same problem was obtained with FV method in ANSYS Fluent and compared to the results derived with BSM with submerged Stokeslets and with the Method of Regularized Stokeslets.

The resulting velocity magnitude contours obtained with BSM and FV methods are shown at Figure 5-2.

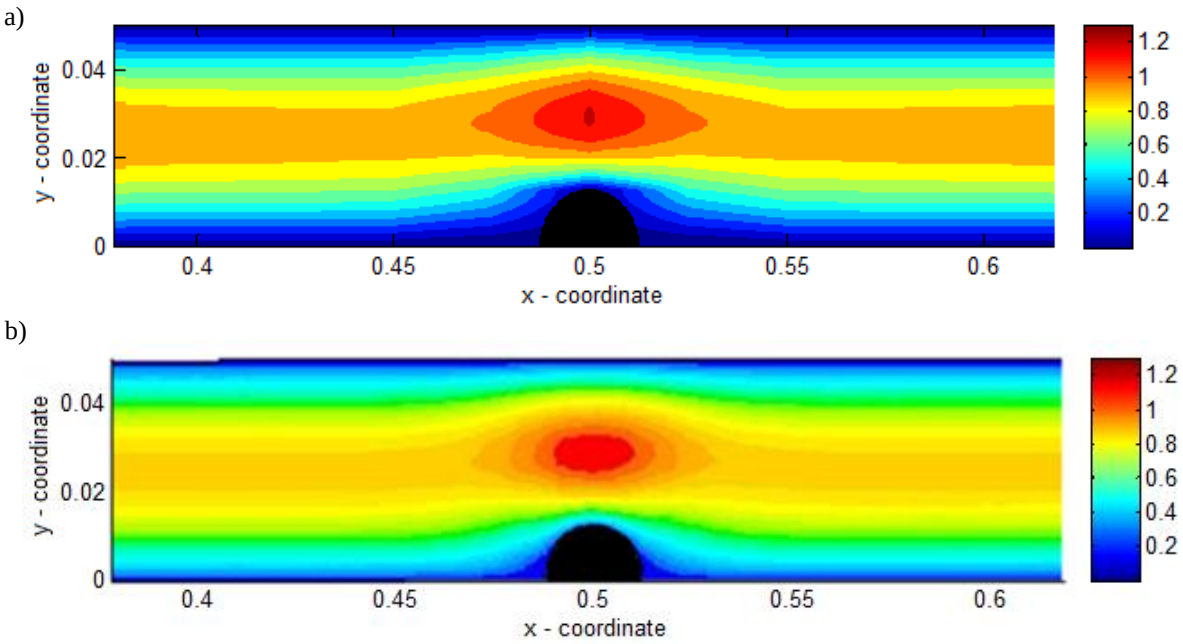

Figure 5-2 Velocity magnitude contours: a) BSM numerical solution, b) finite-volume (ANSYS Fluent) solution

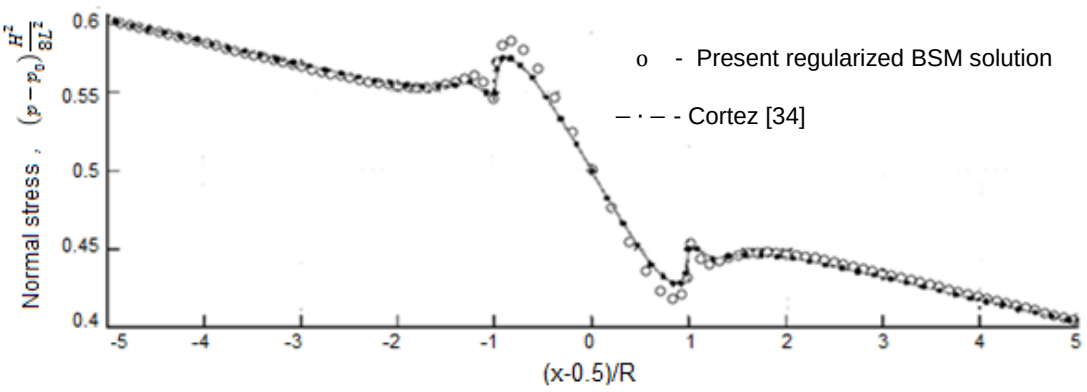

Figure 5-3 Numerical solution for normal stress: BSM with regularized Stokeslets (o) and Cortez (– · –) [34] solutions.

The good correspondence of normal stress and pressure numerical solution obtained with BSM and the solutions obtained with the original solution provided by Cortez in [34] and with the finite-volume method are shown at Figures 5-3 and 5-4.

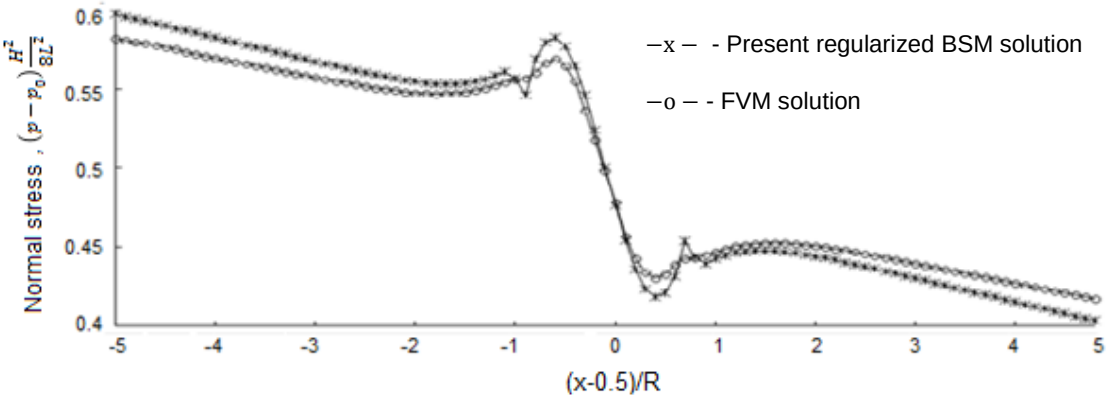

Figure 5-4 Pressure numerical solutions with FVM (–o–) and regularized BSM (– ∗ –) methods.

The difference in pressure between finite-volume and BSM numerical solutions in the figure above is associated with numerical errors and solution of different sets of

equations: BSM is used to solve Stokes equations while finite-volume method in ANSYS Fluent solves Navier-Stokes equations, even though Reynolds number is small in both cases ($Re \leq 1$). It may also be noticed that finite-volume solution smears away pressure jumps in vicinity of cylindrical protrusion. Those jumps are, however, preserved and clearly seen in Figures 5-3 and 5-4.

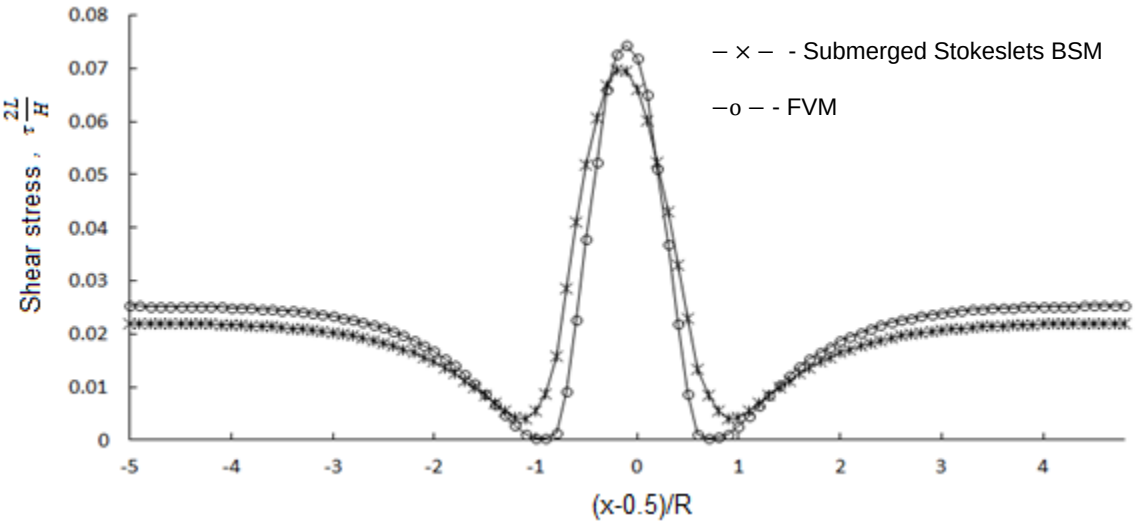

Figure 5-5 Shear stress numerical solutions with FVM ($-o-$) and BSM ($- \times -$) methods.

The shear stress numerical solutions obtained with BSM also show good correspondence with the finite-volume solution (Figure 5-5), as well as with the solution provided by Gaver and Kute in [90] (Figure 5-6). They used boundary integral representations of the flow described with the Stokes and continuity equations. Both graphs represent quite a smooth solution transition for the regions adjacent to the channel protrusion. The only major difference is smaller shear stress amplitudes in those regions shown at both Figures

5-5 and 5-6. This, however, is not the case when comparing solution with the [34] (Figure 5-7). The shear stress jumps present there for the solution obtained by Cortez.

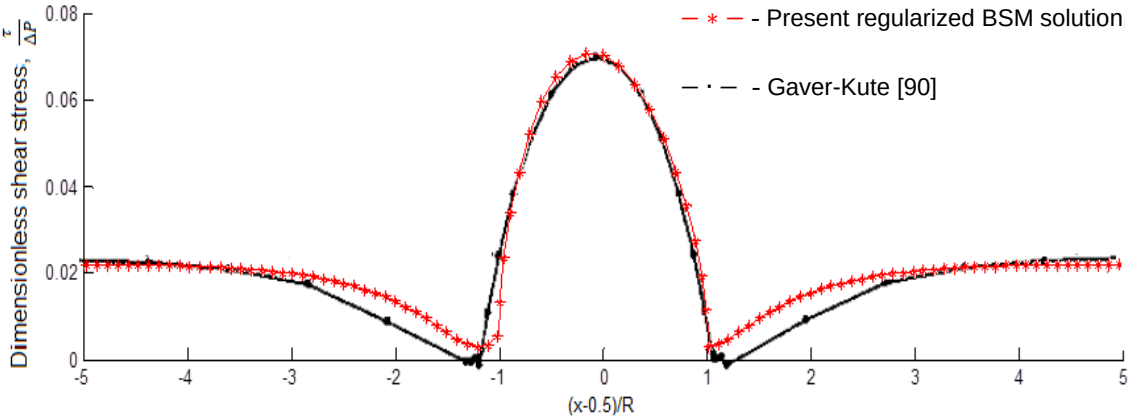

Figure 5-6 Shear stress solutions: BSM with submerged Stokeslets (– ∗ –) and Gaver-Kute solution (– · –) [90].

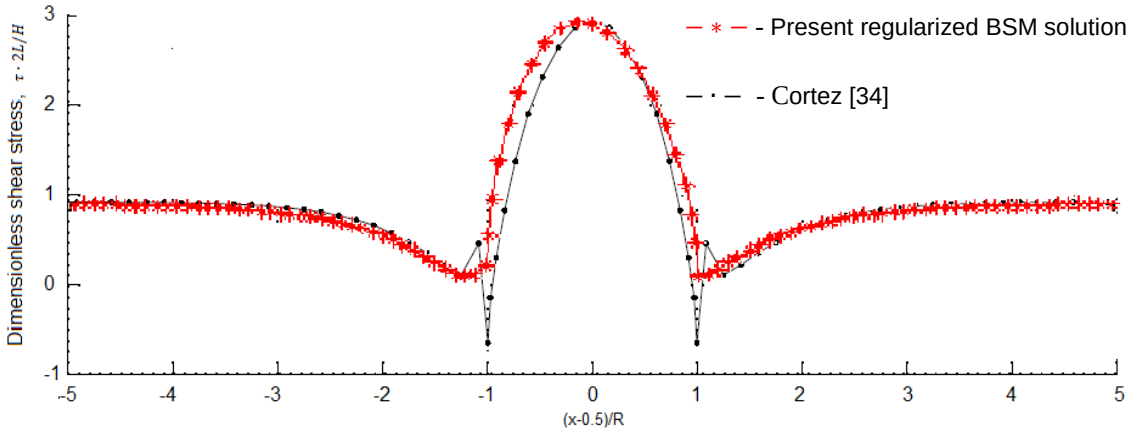

Figure 5-7 Normalized shear stress: BSM with submerged Stokeslets (– ∗ –) and Cortez solution [34] (– · –).

In the present solution, regularization as per Cortez in [34] was used. However, the results shown in Figures 5-3 and 5-7 are not identical. This may be caused by different computational algorithms used in modern solver of linear systems of equation, different round-off errors. Also, shear stress was derived from velocity solution using FDM.

5.2 Deformation of semi-circular geometry in 2-D Stokes flow

The study of the simplified version of a viscous pitch surface deformation near the stagnation region of the NGJ nozzle is considered in the present Section (see Figure 1-1).

Despite of the inaccuracy in pressure and total stress solution discussed in Chapter II, proper Stokeslet regularization parameter $\epsilon = \frac{\Delta s}{4}$ as suggested in [34] and discussed in Section 5.3.1 allows for its' significant reduction. Besides, derivation of shear stress from velocity vector field solution allows diminishing of this inaccuracy during viscous surface deformation simulations. The advantage of regularized Stokeslets in BSM for quasi-steady problems allows avoiding reallocation of Stokeslets under the surface at each time step. They coincide with respective collocation points at each time step, which saves total computation time for surface re-parametrization.

The surface coordinate change is calculated using the following formula:

$$\bar{x}_i^{new} = \bar{x}_i^{old} + \frac{(-\bar{\sigma}_i + \bar{\tau}_{s_i})\hat{t}_i}{\bar{\mu}_l} \Delta s_i \Delta \bar{t}, \tag{5-3}$$

where x_i^{new} is a 2-component coordinate vector of a droplet shape at each iteration; $\hat{t}_i$ is a local tangential direction vector, $\bar{\sigma}_i$ – normalized local surface tension component for the *i*-the Stokeslet; $\bar{\mu}_l$ is an equivalent of Young's modulus in constitutive equation for solid matters, which has a dimension of dynamic viscosity here. In the present problem, there are two droplet viscosity values have been tested to compare droplet deformation

profiles: $\bar{\mu}_l = \frac{H^2}{8L^2}$ and $\bar{\mu}_l = 1$ as per [34] and [88] respectively. $\bar{\tau}_{s_i}$ is a shear stress in a respective surface point. The specified stress component values were normalized by ρU_∞^2.

5.2.1 Validation of the proposed quasi-steady viscous deformation algorithm

A well-known test case of deformation of an infinitesimal cube in a shear horizontal flow [91] has been considered. For simplicity, all properties of an air flow and deformable surface media are taken normalized to unity. The side of the cube was also taken equal to 1. The velocity of the horizontal air has linear distribution with magnitude from 0 to 1. The shear deformation time step here was taken equal to $\Delta t = 0.1s$.

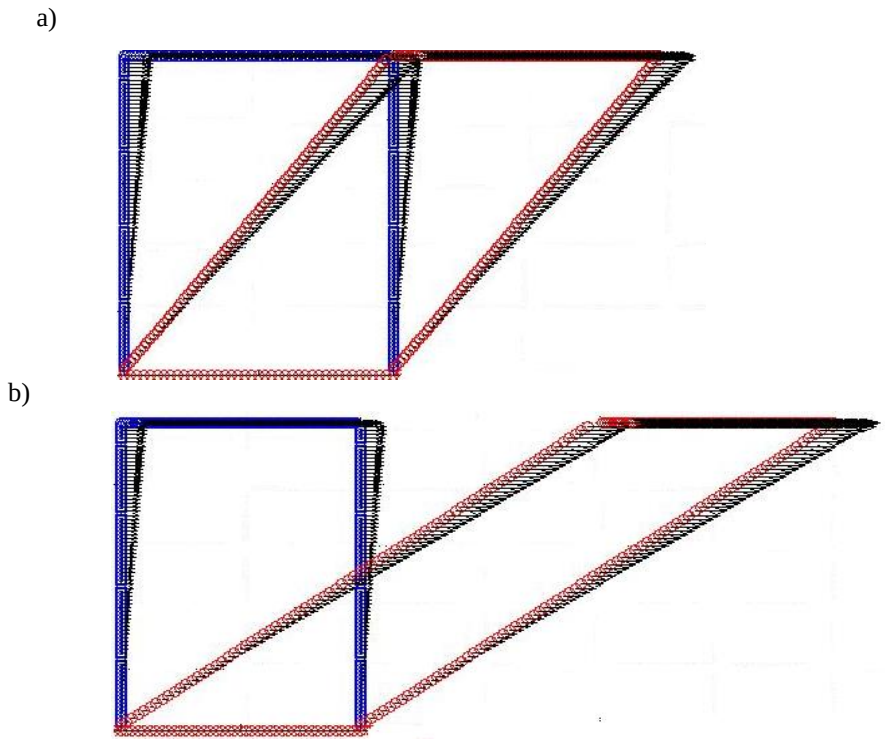

Figure 5-8 Incremental infinitesimal 1x1 cube deformations in a horizontal shear flow: a) after t = 1s, b) after t = 2s.

The results of quasi-steady incremental cube deformation simulation applying proposed quasi-steady algorithm is presented at Figure 5-8. Blue circles designate initial cube boundaries, while red circles represent new location of the dots after respective time of the shear flow action on the surface of the cube. Black arrows show velocity vector field at the boundaries.

The test case of infinitesimal cube deformation in a shear flow has shown validity of the viscous deformation algorithm quasi-steady algorithm and will be implemented in the Matlab solver.

5.2.2 Validation of the BSM with regularized Stokeslets to flow in the protruded channel

The initial set up of the problem is illustrated in Figure 5-9. The inlet uniform velocity flow field with no-slip and no penetrating boundary conditions at the surface of the wall and droplet were assumed. The uniform allocation scheme with regularized Stokeslet was used for BSM simulations of the latter flow stages and subsequent viscous deformations.

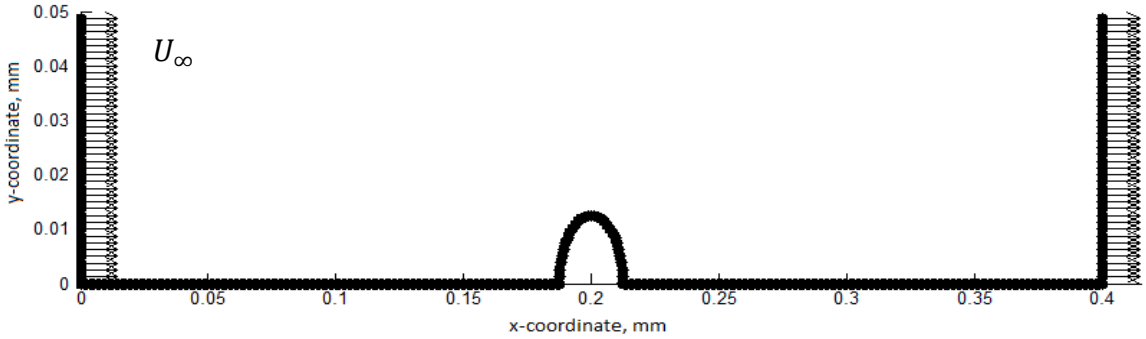

Figure 5-9 Semi-circle viscous deformation problem

The essential feature of the selected scheme for regularized Stokeslets' allocation is that they coincide with the collocation points. Therefore, uniform similar shape allocation scheme was applied to both Stokeslets and collocation points and updated at each time step forming the resulting shape.

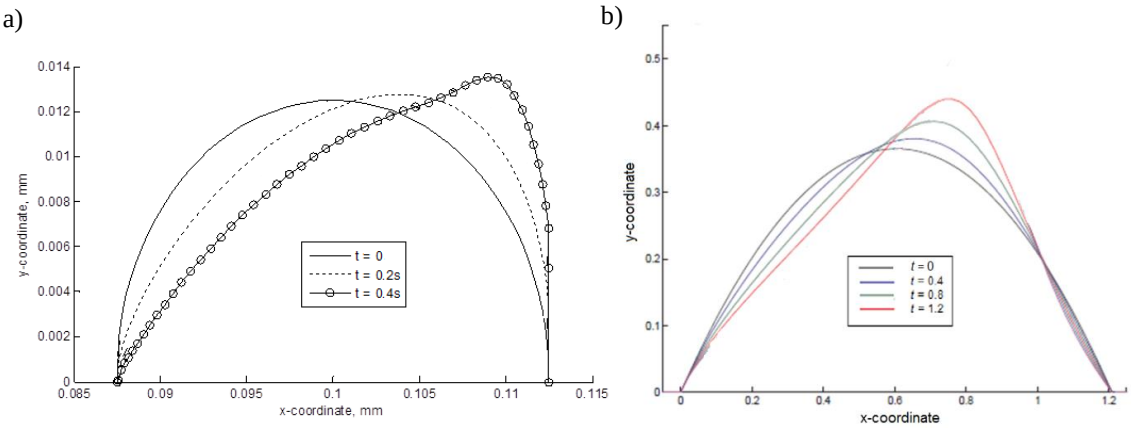

Figure 5-10 Deformation of droplet in a Stokes flow boundary layer: a) BSM solution for semi-circular droplet and viscosity normalized to $\bar{\mu} = \frac{H^2}{8L^2} = 0.002$; b) parabolic surface deformation (subfigure taken from [88]).

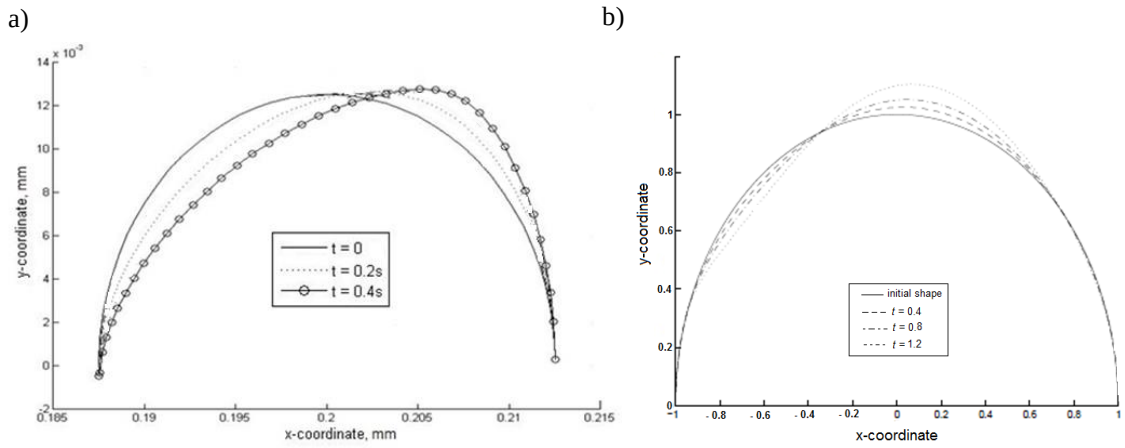

Figure 5-11 Deformation of droplet in a Stokes flow boundary layer with the center located 0.2 specific length units away from the flow entrance at viscosity equal to $\bar{\mu}$ = 1; b) deformation of semi-circular droplet (subfigure taken from [88]).

Once simulations were performed, the resulting deformation profiles of semi-circular shapes have been obtained (Figures 5-10 and 5-11). The viscous properties of deformed surface remained unchanged for the sake of solution validation.

Figures 5-10 and 5-11 designate surface deformation for two different cases: Figure 5-3 represents the case $\frac{\mu_g}{\mu_l} = 1$ as per [88] and Figure 5-11 show simulation results for $\frac{\mu_g}{\mu_l} = \frac{H^2}{8L^2}$ as per [34] discussed in the Chapter III.

Despite the differences in problem formulation and initial shapes presented in Figures 5-10 and 5-11, the resulting show significant qualitative resemblance of viscous surface deformation. In the next Sections the surface tension component is included in the constitutive equation of deformation simulation.

For the future validation of a solution for viscous deformation simulations for 3-D semi-spherical droplet on a flat surface it is interesting to compare BSM results with the ones provided in the paper by Dimitrakopoulos [92].

5.3 Deformation of parabolic shape obstacle in 2-D Stokes flow

In the present Section, a parabolic curve described with (5-12) was used as a representative shape for 2-D numerical modeling using BSM. This family of shapes can be introduced to simulate viscous droplets and tracks having large contact area with the surface, which is characterized by highly intense surface wetting.

5.3.1 Validation of BSM for two-dimensional problems of viscous deformation of non-circular obstacle in a horizontal Stokes flow.

The problem solved here was used for further validation of BSM applied to 2-D quasi-steady viscous deformation under low-Reynolds number flows. The BSM solution was compared to the one presented by H.Fry [88] in her dissertation, who solved the problem with the particular assumption of the perfect slip of the droplet. It has been extended here and split into two cases of viscous 2-D parabolic droplet deformation in Stokes flow that solved using BSM with regularized Stokeslets:

1) deformation of the liquid droplet in the Stokes flow through a rectangular channel;
2) deformation of a liquid droplet in the Stokes flow along the plate in semi-infinite domain.

The geometrical model presented in Figure 5-12 and physical assumptions are given as follows:

1) The problem is physically formulated as a Stokes flow over the horizontal flat plate or in the rectangular channel with a settling water droplet. No-penetrating and no-slip boundary conditions are assumed at the wall and the water droplet surface. The gravity is neglected.
2) The initial droplet shape is described with the following governing equations:

$$\begin{cases} \bar{y}(\bar{x}) = g(1-\bar{x}^2)^4, & |\bar{x}| < 1 \\ 0, & otherwise \end{cases}, \tag{5-4}$$

where g factor in this Section was equal to 0.1 to match the geometry in [88].

3) Following test case formulation in [88] for the parabolic shape droplet, the ratio of viscosities of droplet liquid and surrounding gas has been taken $\frac{\nu_g}{\nu_l} = 1$ (densities are assumed equal to unity).

The initial velocity boundary conditions of a horizontal Stokes flow were normalized to unity, which yields $\bar{u} = 1, \bar{v} = 0$. The actual size of the considered part of the flow field is also normalized to the droplet shape coordinate units (5-4) and represents a 4-by-0.4 rectangular domain. Corresponding normalized spatial coordinates are introduced as follows.

$$\{\bar{x}, \bar{y}, \bar{z}\} = \frac{1}{L}\{x, y, z\}, \tag{5-5}$$

where $L = 1116\ \mu m$, and x, y and z are actual domain coordinates in μm.

For the purpose of validation of BSM, the solution of the problem was obtained by using regularized Stokeslets. A characteristic spatial discretization parameter – distance between neighboring Stokeslets - was selected equal to $\Delta s = 0.0113$, and the optimal regularization parameter value (according to Cortez) was computed as $\epsilon = \frac{\max(\Delta s)}{4}$. The number of Stokeslets for the overall problem domain was equal to 1681.

As it was discussed in the first two Chapters, contrary to the FD and FV methods, BSM does not imply usage of stability numbers as Courant-Friedrichs-Lewy number. BSM solution convergence is controlled by selection of appropriate Stokeslet allocation

scheme, allocation depth or regularization parameter value and the number of Stokeslets, which in its' turn prescribes the distance between neighboring points Δs.

The time step in present simulations was $\Delta\bar{t} \cong 0.01$. Normalized dimensionless time for the droplet deformation simulations has been calculated based on the condition of shear stress equity at the interface that has been found from (4-3).

Finally, the surface coordinates are updated at each time step using the proposed discretized constitutive equation for viscous fluid deformation (5-3).

Surface tension in point can be found from Young-Laplace equation. It is reciprocal to a local surface curvature radius multiplied by the surface tension coefficient for the particular gas-liquid interface [93]:

$$\sigma_i = \frac{\gamma_f}{r_i} = \gamma_f \kappa_i \,, \tag{5-6}$$

where κ_i is a principal curvature in *i*-th collocation point. For 2-D case problems in this Section principal curvature was determined numerically using central finite-difference scheme:

$$\kappa_i \approx \frac{\bar{y}_{i+1} - 2\bar{y}_i + \bar{y}_{i-1}}{\frac{1}{4}(\bar{x}_{i+1} - \bar{x}_{i-1})^2}, \tag{5-7}$$

where $\bar{x}_{i-1}, \bar{x}_{i+1}, \bar{y}_{i-1}, \bar{y}_i, \bar{y}_{i+1}$ are normalized coordinates of collocation points at a boundary surface.

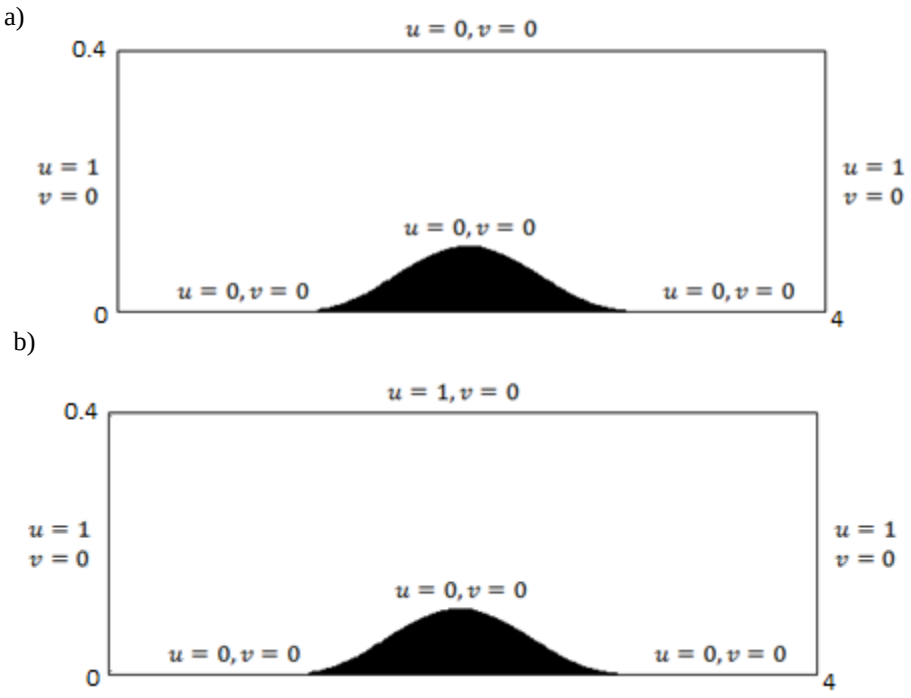

Figure 5-12 Problem domain and boundary conditions set up: a) Stokes flow over droplet settling in rectangular channel; b) free-surface Stokes flow along the flat plate with a droplet settling on it.

In case of flow inside the boundary layer about deformable obstacles of various shapes presented in Chapter 8 of [88], finite difference method with the explicit in time numerical scheme was applied to solve nonlinear partial differential equation incorporating shear and surface tension components.

The discretized governing differential equation for the droplet interface coordinate change presented in [88] was derived from the continuity equation and kinematic condition resulting in Reynolds lubrication type equation for the deformable interface coordinate. The grid cell size of the domain in the discretized solution of the equation was selected $\Delta\bar{x} = 0.01$ and the time step was $\Delta\bar{t} = 0.01$. The presented solution,

however, does not assume horizontal droplet displacement due to shear stress exerted at its' surface.

The initial Stokes flow boundary conditions for both problems are set up as presented in Figure 5-12. They are only different with the upper boundary conditions.

a)

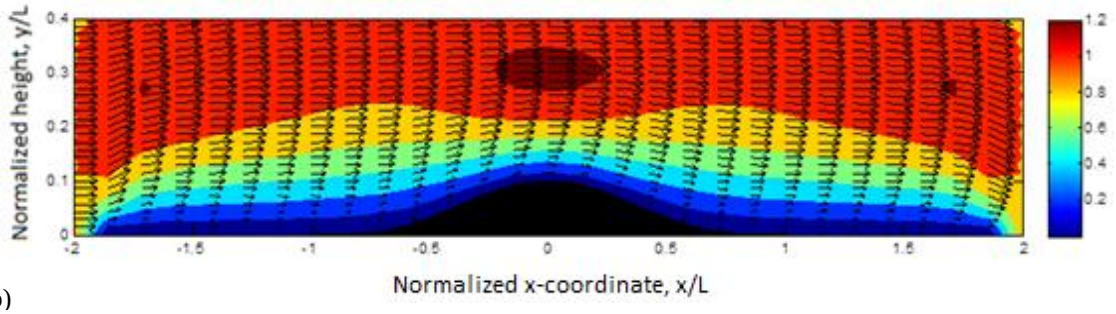

b)

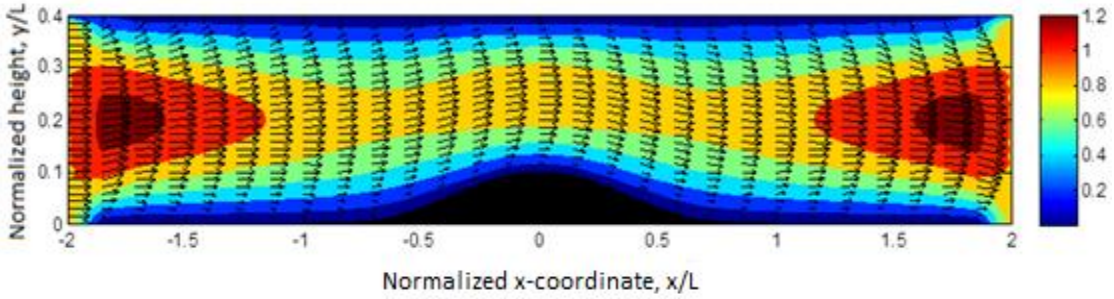

Figure 5-13 Velocity vector field, magnitude contours and the flow streamlines about droplet model presented in [88]: a) flow over a flat plate; b) flow in a rectangular channel.

The resulting velocity vector field and magnitude contours for the problem of droplet deformation in a horizontal Stokes flow in the rectangular channel and at the flat plate are presented in Figure 5-13. Coordinates were normalized as per (5-5) and velocity was normalized over the maximum value at the boundaries of the domain.

a)

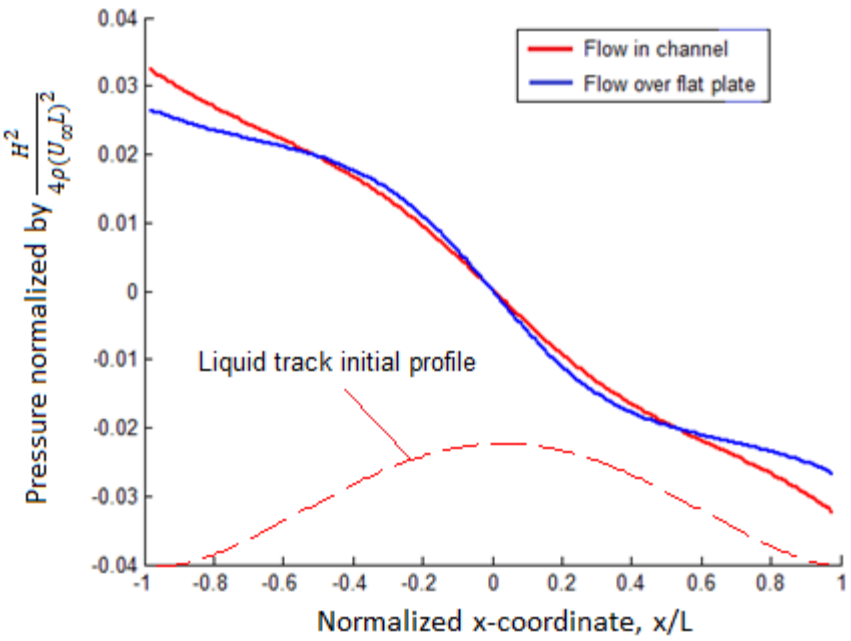

b)

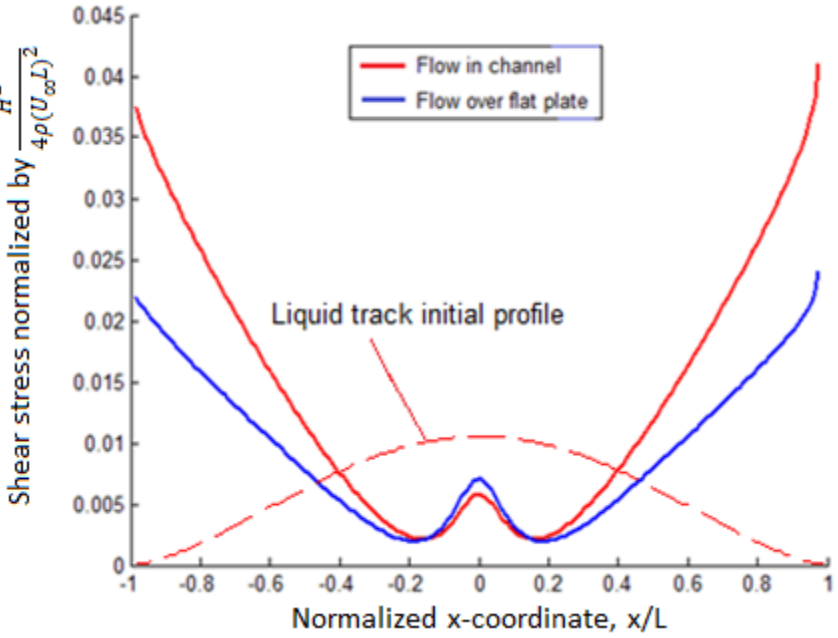

Figure 5-14 Normalized pressure (a) and shear stress (b) about parabolic pitch ripple in the rectangular channel.

a)

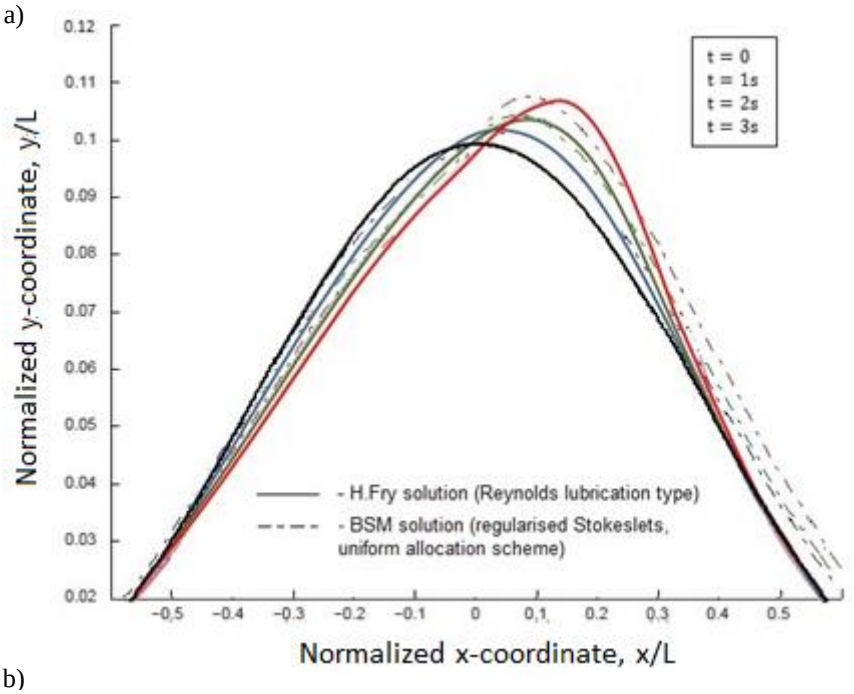

b)

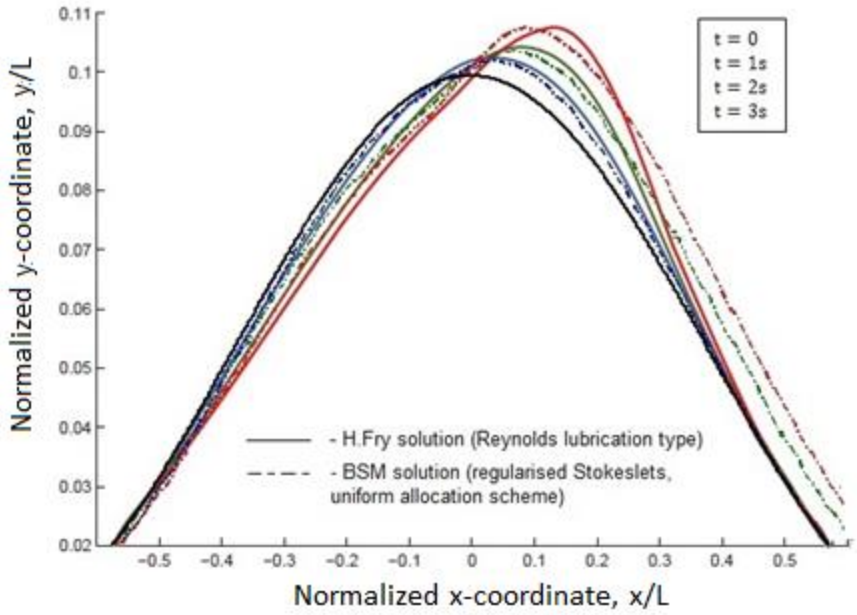

Figure 5-15 Comparison of viscous droplet deformation profiles for the Stokes flow: a) in rectangular channel; b) along the plate with the settling droplet (Fry model [88] and BSM solution).

The flow velocity magnitude and pressure depend on the channel dimensions. In fact, for very narrow channel boundary conditions start affecting the solution. Therefore, it was chosen to use $\frac{H^2}{L^2}$ ratio in the stress normalization in Chapters V (Figures 5-14, 5-18 and 5-19), as well as in the Chapter VI for 3-D problem of the viscous droplet deformation in the channel.

Figure 5-14 shows slightly higher pressure and shear rate gradients for the flow past a droplet in a 2-D rectangular channel than for the flow over droplet sitting on a flat plate. This causes slightly higher amplitude deformations of droplet in a Stokes flow in the channel compared to the same droplet deformation sitting on a flat wall in semi-infinite domain.

One may evaluate deformation profiles of highly viscous droplet obtained with the BSM at a given dimensionless time. The simulation times were particularly selected to compare the resulting droplet deformation shape profiles to the ones presented in [88]. The results are presented in Figure 5-15.

One may observe significant resemblance between Figures 5-15a and 5-15b in the part of BSM solution corresponding to cases of a Stokes flow about parabolic droplet settling in the rectangular channel and at the flat plate respectively. However, larger viscous deformation at $\bar{t} = 3$ are noticeable for the first case due to higher shear rates in the domain area adjacent to the droplet surface, especially in vicinity of its' top part.

5.3.2 Validation of BSM solution in two-dimensional problems of non-circular droplet viscous deformation under non-horizontal Stokes flow.

The following data were taken to formulate and solve the problem of Stokes flow impinging viscous surface of parabolic pitch ripple in rectangular channel (Table 5-1).

Table 5-1 Number of Stokeslets and velocity magnitude in boundary conditions

Flow angle, degrees:	Number of Stokeslets	Velocity boundary conditions:	
		x-component	y-component
0	1681	1	0
30	- // -	0.866	-0.5
45	- // -	0.707	-0.707

The velocity components presented in Table 5-1 for each particular flow orientation designate uniform far field flow direction at boundaries of the computational domain presented in Figure 5-16:

$$\begin{cases} u_x = U_\infty cos\alpha \\ u_y = U_\infty sin\alpha, \end{cases} \tag{5-10}$$

For comparison, regular Stokeslet allocation scheme was used to compute velocity vector field, pressure and shear stress. The Stokeslet allocation depth was selected $\overline{D} = 0.001$ around the computational domain. It was normalized by the length of the domain and presented in Figure 5-16 and the resulting solution of the flow field is shown in Figure 5-17.

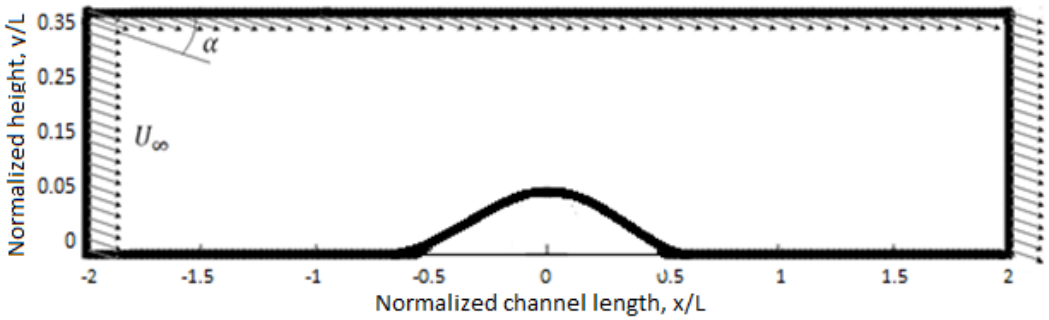

Figure 5-16 Problem formulation.

a)

b)

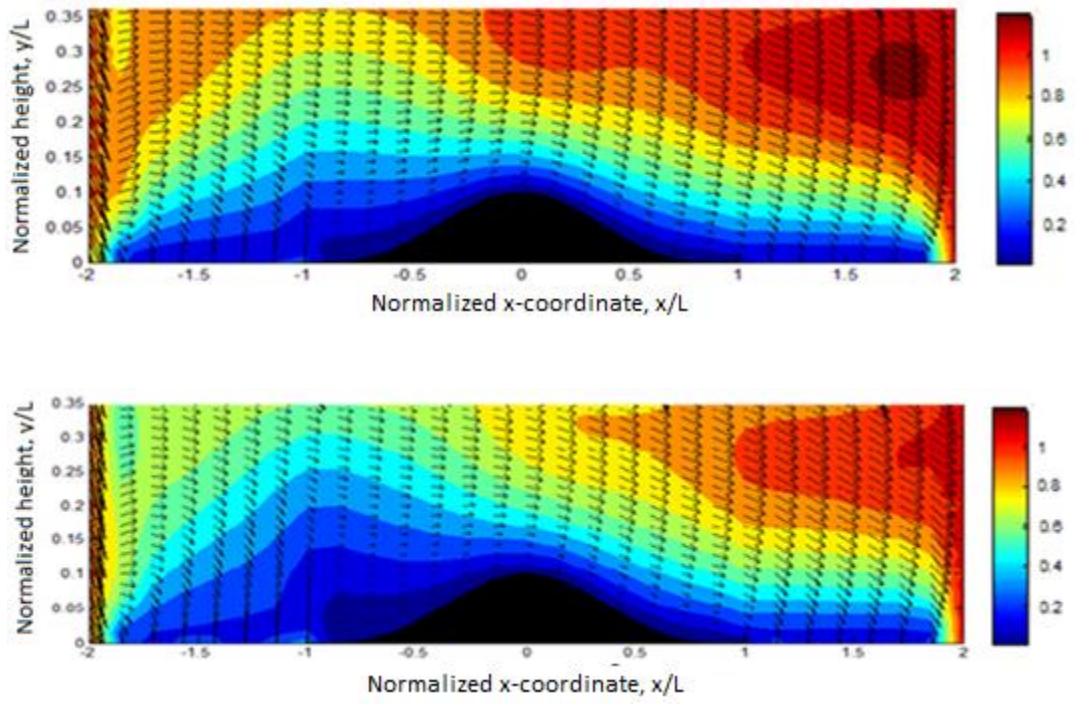

Figure 5-17 Velocity magnitude contours and vector field in rectangular channel: a) flow at 30 degrees; b) flow at 45 degrees.

Numerical experiments show that condition numbers of Stokeslet matrices for BSM with regular Stokeslets (Table 5-2) for all three air flow orientation cases do not differ by

much. Therefore, for this particular problem the angle of velocity in boundary conditions presented above does not have significant influence on computational matrix condition number and, consequently, the solution accuracy in all three cases is the same.

Table 5-2 Condition numbers of velocity Stokeslets computational matrix

Flow angle, deg:	Velocity matrix condition number
0	$1.234 \cdot 10^{20}$
30	$1.676 \cdot 10^{20}$
45	$8.495 \cdot 10^{19}$

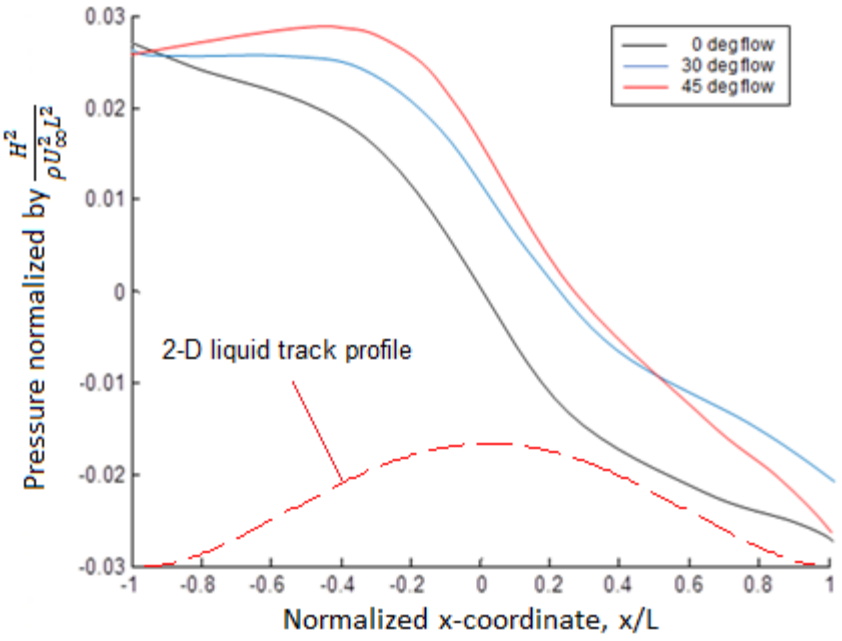

Figure 5-18 Normalized pressure about parabolic pitch ripple in the rectangular channel.

Velocity vector field and magnitude contours presented in Figure 5-17 show initial velocity profile about parabolic shape viscous deformable droplet surface at $\bar{t} = 0$ solving for the uniform far-field velocity at the domain boundaries.

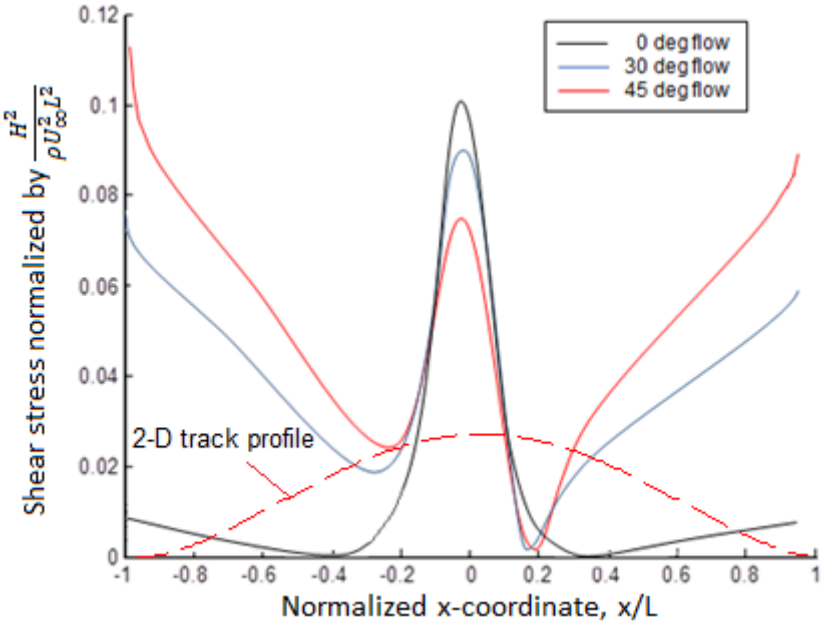

Figure 5-19 Normalized shear stress about parabolic pitch ripple in the rectangular channel.

Figures 5-18 and 5-19 depict normalized pressure and shear stress distribution along the plate versus the flow orientation angle. It is possible to notice that shear stress in the proximity of the droplet becomes smaller with the increase of the flow angle. The normalized total pressure in the areas adjacent to the droplet (Figure 5-18) is growing with the flow angle, which is inherent to the flow stagnation zones.

It was mentioned before that the shear stress solution was obtained during post-processing procedure using biased finite-difference $O(\Delta\bar{r}^2)$ scheme as per (5-3), where

$\Delta\bar{r}_i$ is a normalized distance from the respective point of the flow field to the nearest collocation point and normal to a liquid surface. Computation of shear stress as per (5-3) requires velocity solution at two layers away from the boundary: $\Delta\bar{r}_{1_i} = 0.001|\vec{r}_i|$ and $\Delta r_{2_i} = 0.002|\vec{r}_i|$, where $\vec{r}_i$ is a coordinate in respective droplet surface point.

5.4 Application of BSM to the problems of viscous deformation in stagnation flow in NGJ nozzle

The following problem represents 2-D simulation of inclined air stream impinging deformable liquid track at the bottom of a rectangular channel. It is physical model of prototype interaction between air jet and liquid mesophase pitch surface ripple in NGJ nozzle reaction zone and is aimed at better understanding of aerodynamic interaction pertaining to nanofiber "birth" and further growth process.

5.4.1 Formulation of the problem

In the present sub-section, initial velocity boundary condition profile is imported from preliminary velocity vector field calculated using FV method in ANSYS Fluent for the entire rectangular nozzle domain. Then the low-Reynolds number flow regions have been determined in vicinity of liquid mesophase pitch ripple formation.

The problem considered in this Section is formulated the same way as in Section 4.1 and Figure 1-1. Normalization of the spatial coordinates and flow properties is

performed as prescribed by (5-3) - (5-5). The resulting velocity magnitude contours are presented in Figure 4-2 of the previous Chapter.

5.4.2 Proposed FV-BSM solution algorithm for 2-D Stokes flow problem in stagnation flow region

Like in the previous case, the deformable surface of liquid ripple/track has 2-D parabolic shape and has been incorporated into the BSM computational domain.

A multiple scale problem of a turbulent air flow in the channel and Stokes flow proximity of the stagnation point is considered. The air jet discharged into the channel and impinging surface of a molten mesophase pitch 2-D track on a flat plate in rectangular channel is simulated using FVM and BSM methods coupled with a Stokeslet regularization technique [34]. The detailed method algorithm is shown in Figure 5-20.

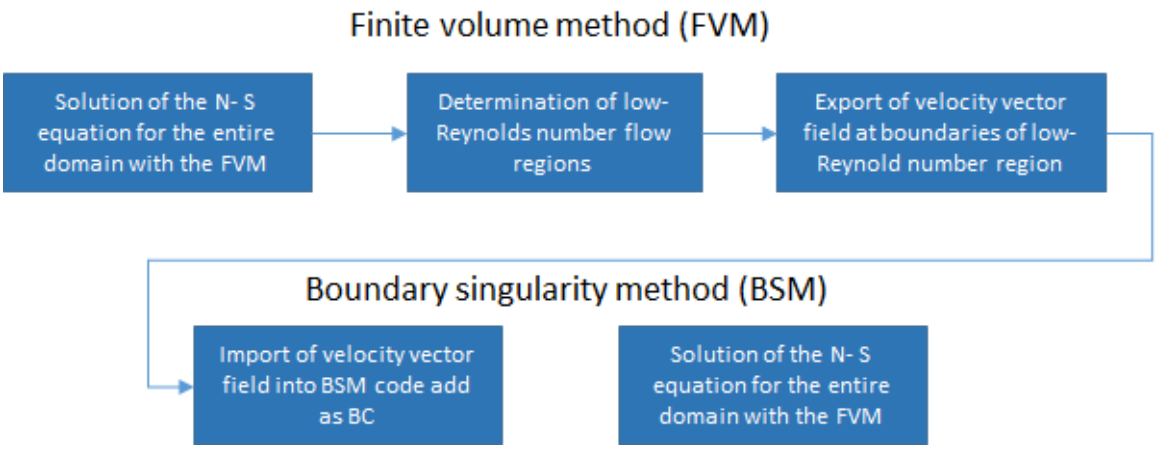

Figure 5-20 Multi-scale solution algorithm for solving quasi-steady problem of viscous deformation of liquid ripple by coupling FVM (for Navier-Stokes (N-S) equations) and BSM (for Stokes equation) with imported boundary conditions (BC).

5.4.3 Modeling of viscous deformation of 2-D shapes in Stokes flow with imported velocity boundary conditions using BSM

The molten viscous pitch 2-D track on the flat surface model is represented by a parabolic profile on a long rectangular surface.

a)

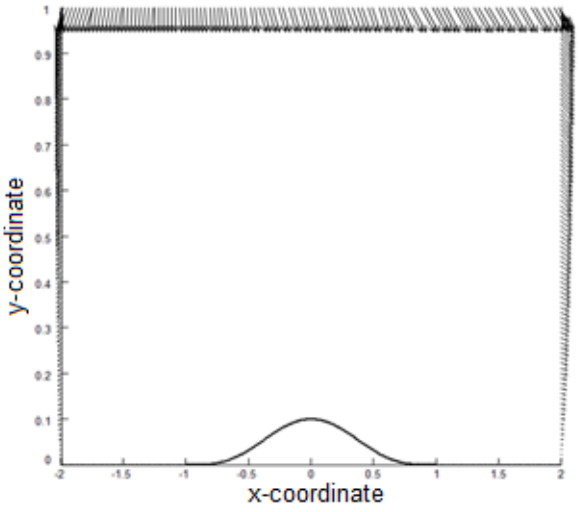

b)

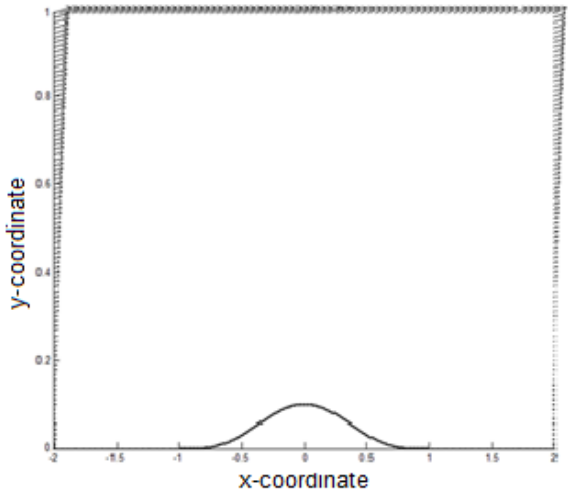

Figure 5-21 Low-Reynolds number flow region domain with imported velocity boundary conditions for air flow orientation: a) 45 degrees; b) 30 degrees.

The flow field in the domain of stagnation region is considered to be isothermal and heat transfer is neglected. Therefore no energy equation incorporated into the physical model describing the process. The liquid track is placed in the center of the stagnation region (Figure 5-21).

In order to apply quasi-steady algorithm (5-3) to the problem of viscous deformations, the linear system is solved for unknown strength of Stokeslets and then velocity, pressure and shear stress are computed by using obtained Stokeslets (2-2)-(2-4). Then shear stress and surface tension components were used to calculate corresponding displacement in the respective direction, multiplying it by the projected area of the deformable surface, where every collocation point is a centroid of respective surface element.

Once completed, the coordinates are updated and used as new collocation points reshaping the surface for subsequent iteration, which concludes the algorithm.

After the preliminary flow field solution was obtained with FVM in ANSYS Fluent for the entire channel domain (Figure 4-2), the velocity vector field at nodes of inflation zone for a low-Reynolds number flow region has been determined. The resulting values were interpolated over rectangular boundaries of the droplet-scale domain for subsequent BSM simulation (Figure 5-21). The new boundary velocity vector field was then used to allow more accurate BSM solution for velocity vector field and evaluate stress components induced by the air flow over the modeled parabolic shape droplet assuming no-slip and no-penetrating boundary condition. The velocity at the bottom

surface and at the droplet placed inside the microscale domain was set equal to zero. Spatial coordinates were normalized to the size of the resulting domain.

The parabolic droplet shape in the channel is described as follows:

$$\begin{cases} \bar{y}(\bar{x}) = g(1-\bar{x}^2)^2, & |\bar{x}| < 1 \\ 0, & otherwise \end{cases}, \tag{5-11}$$

where $g = 0.4$.

The resulting boundary condition velocity components have been normalized as follows:

$$\begin{cases} \bar{u}_i = \dfrac{\bar{u}_{i_{FL}}}{max\sqrt{\bar{u}_{i_{FL}}^2+\bar{v}_{i_{FL}}^2}} \\ \bar{v}_i = \dfrac{\bar{v}_{i_{FL}}}{max\sqrt{\bar{u}_{i_{FL}}^2+\bar{v}_{i_{FL}}^2}} \end{cases}, \tag{5-12}$$

where $\bar{u}_{i_{FL}}$ and $\bar{v}_{i_{FL}}$ are normalized components of 2-D boundary condition velocity vector field imported from ANSYS Fluent.

Figure 5-20b) shows the resemblance between boundary condition velocity vector field imported from the solution obtained using FVM in ANSYS Fluent for the case of air jet impinging the wall at 30^o and boundary conditions presented in Chapter 8 of [88] for the same problem. The difference is the length-to-height ratio of the domain boundaries. It is, therefore, reasonable to expect similar deformation profiles for the parabolic droplet computed with BSM for a 30^o case to the solution presented in [88]. Similarly to the resulting solution for the horizontal flow field presented in Figure 5-17, the velocity

vector fields solved for the boundary conditions imported from ANSYS Fluent (Figure 4-2) and magnitude contours are shown in Figure 5-22.

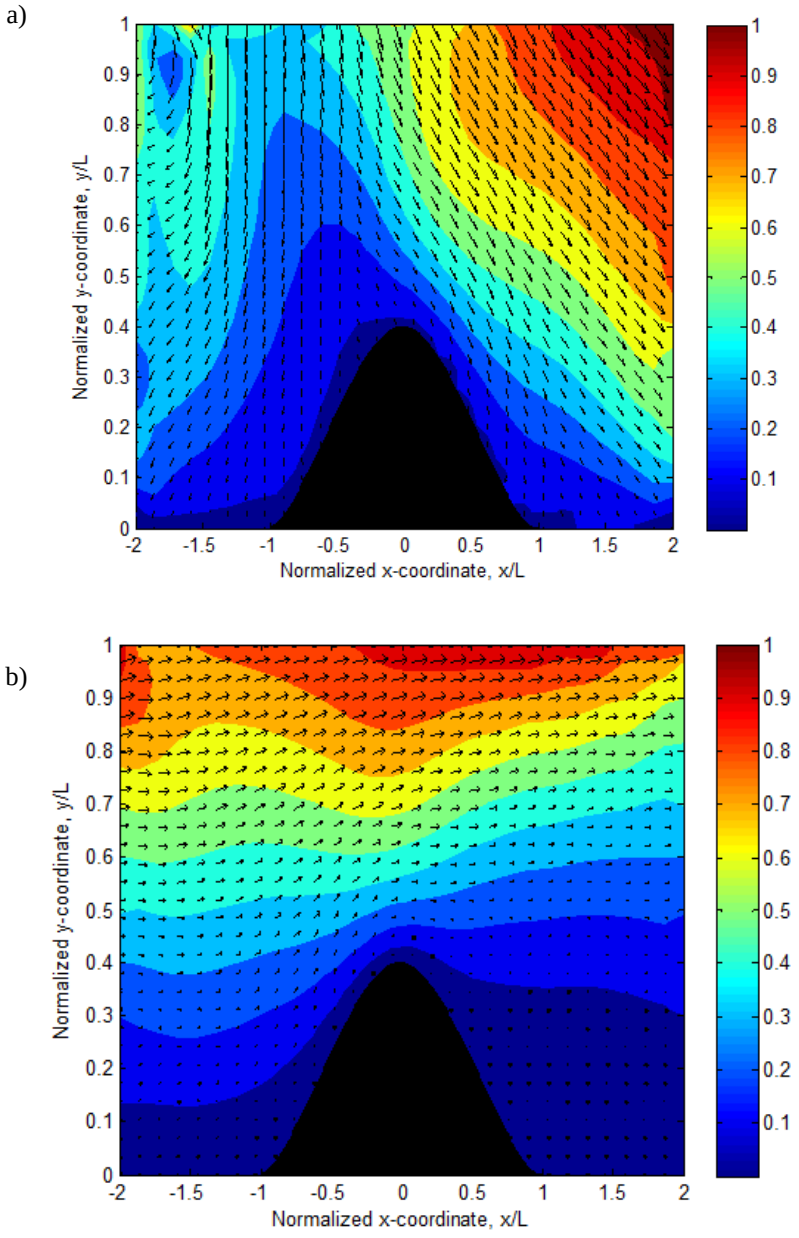

Figure 5-22 Initial velocity magnitude contours and vector field in rectangular channel with imported boundary conditions for the cases of air jet discharged into the channel at: a) 45 degrees; b) 30 degrees.

They represent the velocity profile about the parabolic profile at $\bar{t} = 0$ solving for the low-Reynolds number region in the "air-liquid" reaction zone.

a)

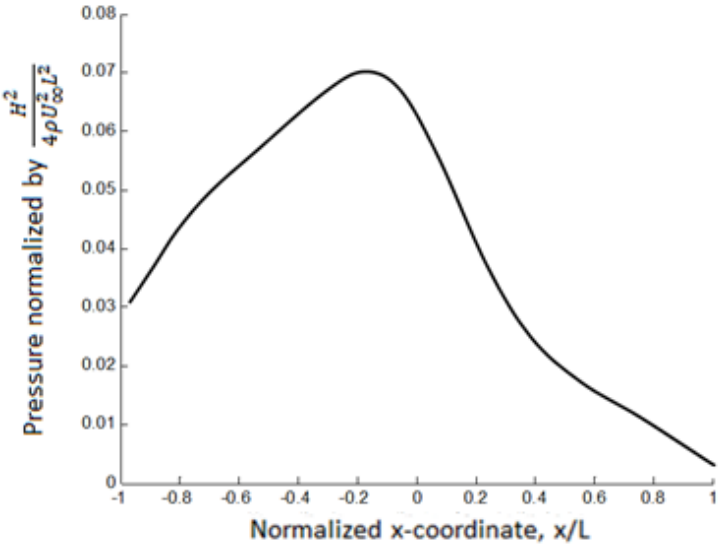

b)

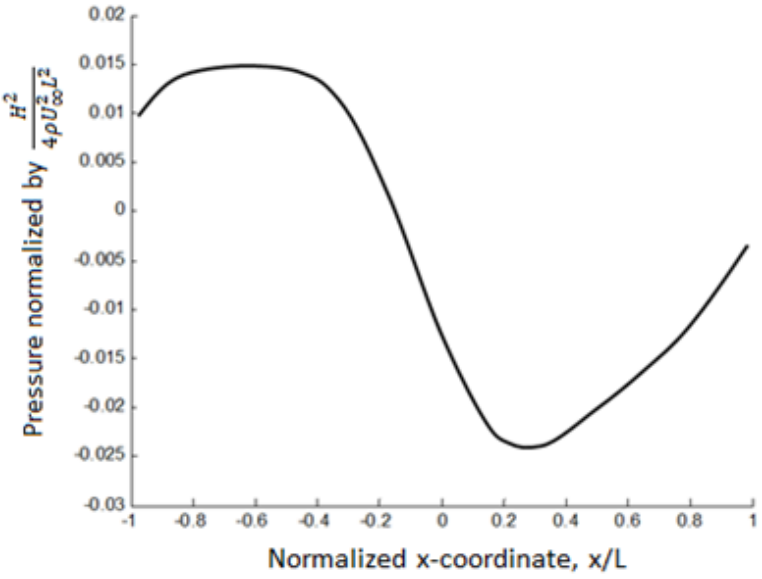

Figure 5-23 Normalized pressure about parabolic pitch ripple for the air jet flow orientation flowing into the rectangular channel: a) 45 degrees; b) 30 degrees.

a)

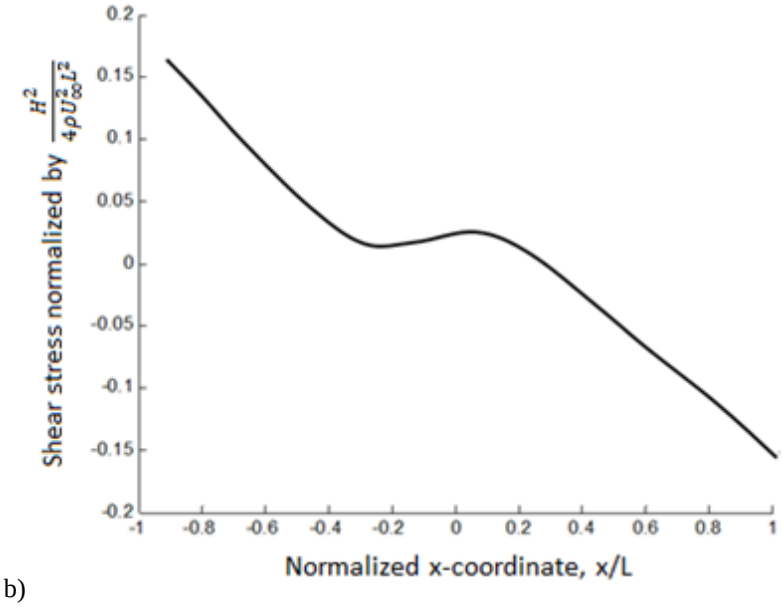

b)

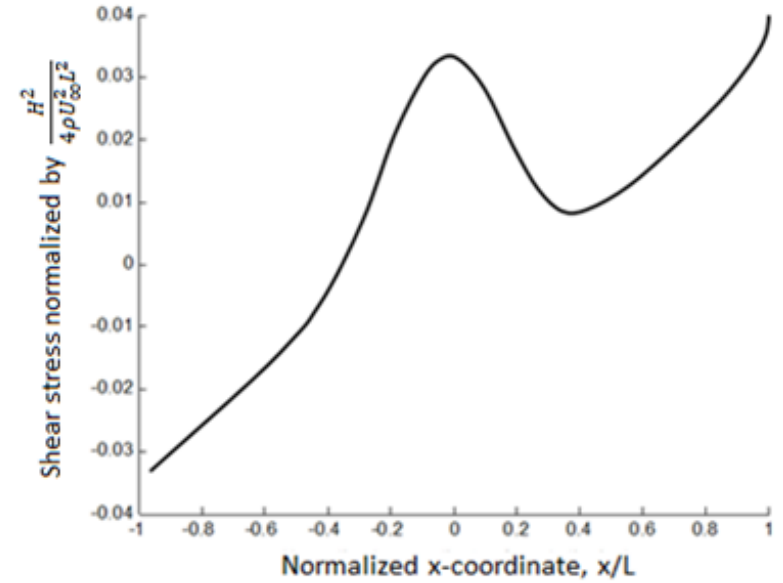

Figure 5-24 Normalized shear stress about parabolic pitch ripple for the air jet flow orientation flowing into the rectangular channel: a) 45 degrees; b) 30 degrees.

It is easy to notice both the qualitative and magnitude difference in pressure at the droplet surface computed for the jet discharged into the rectangular channel at 45^{o} and 30^{o} are observed in Figure 5-23.

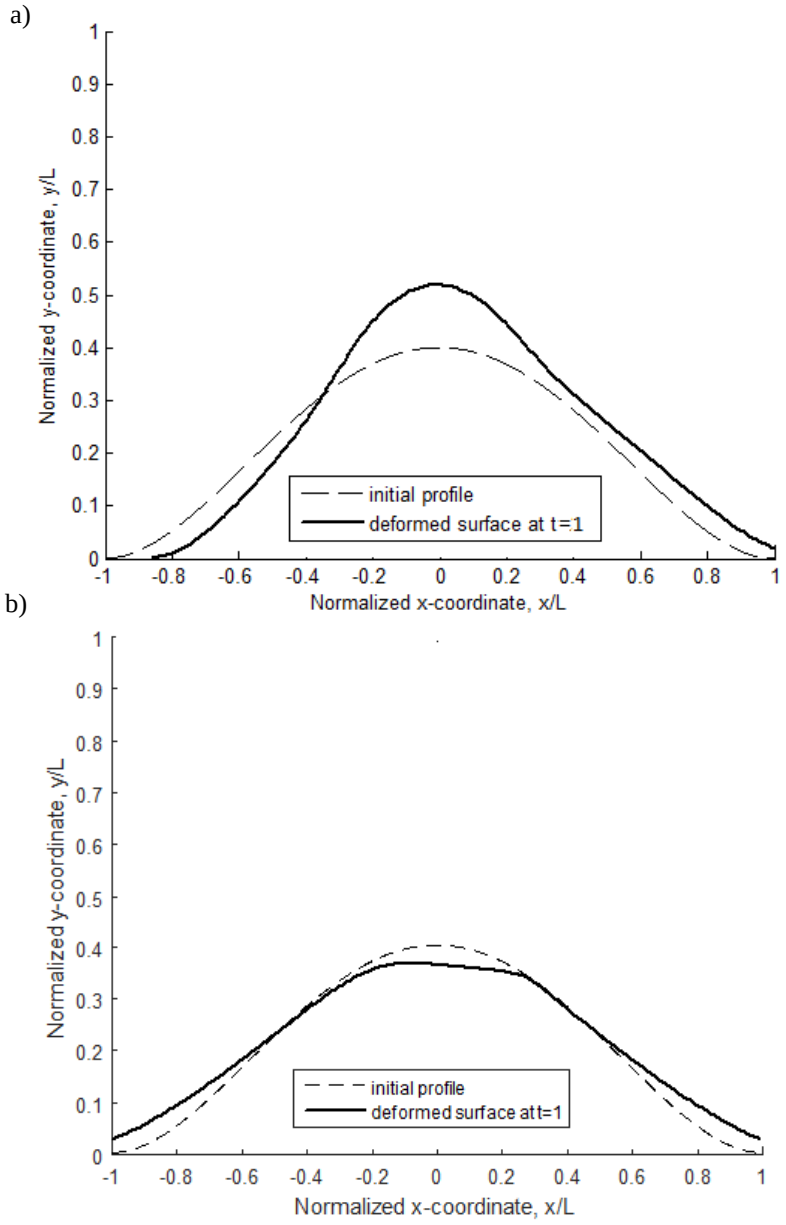

Figure 5-25 Parabolic ripple deformation shape with regularized Stokeslets solution using imported BC for the case of air jet impinging parabolic pitch ripple at: a) 45 degrees; b) at 30 degrees.

Comparing pressure magnitude with shear stress for the respective cases, one may conclude that the droplet shape at the 30-degree flow is changed inherently by shear stress, while at 45 degrees the pressure in vicinity of the droplet peak is larger. Shear stress is smearing it apart from the center (see Figure 5-18). In the present problem BSM solution for velocity vector field and stress components were obtained using regularized Stokeslets.

a) b)

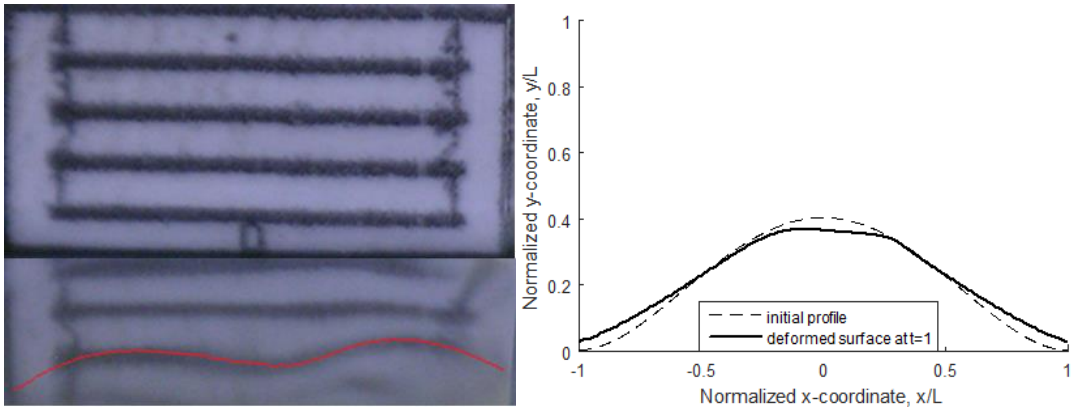

Figure 5-26 Deformation of viscous droplet in the rectangular channel under air jet impinging at 45 degrees: a) experiment b) BSM.

The results of BSM simulations of the pitch ripple profile deformations are presented in Figure 5-25. It is easy to notice that at higher y-component velocity magnitude and pressure for the case of air jet impinging the wall of the rectangular channel at the angle of 45^{o}, pitch ripple deformations are more intense than for the case of 30^{o}. The 30^{o} flow case exhibits smoother transitions and lower pressure magnitude resulting in growth of pitch ripple that will eventually be exposed to the higher Reynolds number region with the drag increased.

Analyzing droplet deformation profile for the case of air jet oriented at 45^{o} with respect to the channel bottom surface and comparing it to the 30^{o} orientation case a qualitative difference is observed.

A comparison of numerical simulations discussed above with the experiment (see Chapter IV) is presented in Figures 5-26 and 5-27.

a)

b)

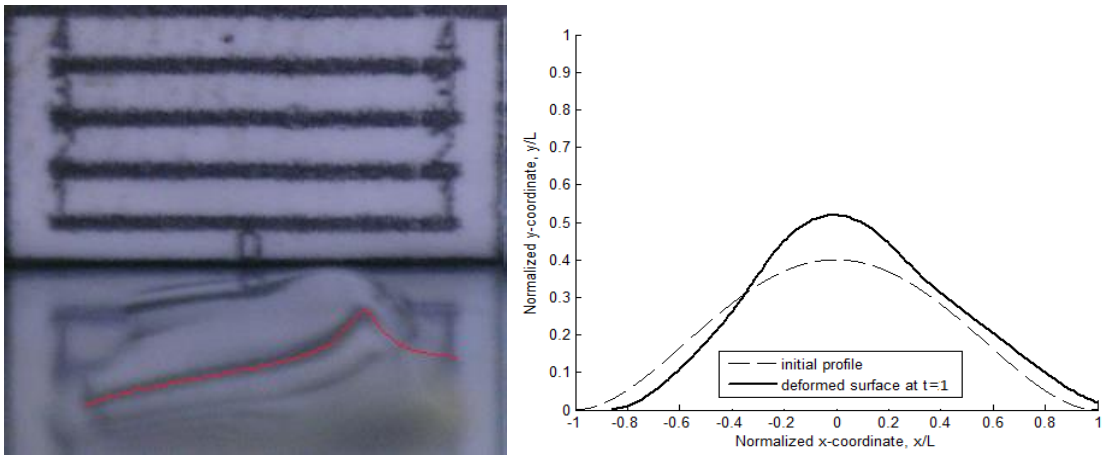

Figure 5-27 Deformation of viscous droplet in the rectangular channel under air jet impinging at 30 degrees: a) experiment; b) BSM.

The numerical simulation of viscous deformation of 2-D PDMS tracks under impinging air flow has a good qualitative correspondence with the experimental results presented in Chapter IV. The deformation profiles were compared for both air flow orientation cases – 30^{o} and 45^{o} – at respective times.

The next Chapter is dedicated to the discussion of BSM simulation results of viscous deformation of 3-D parabolic droplets placed in the same air flow conditions in the stagnation region and their comparison with the respective experimental results.

CHAPTER VI

APPLICATION OF THE BOUNDARY SINGULARITY METHOD TO QUASI-STEADY THREE-DIMENSIONAL PROBLEMS OF VISCOUS DEFORMATION IN STOKES FLOWS

In the present Chapter application of the BSM to 3-D problems of viscous deformation in Stokes flows will be discussed. The first Section is dedicated to a validation of BSM with regular Stokeslets and comparison of the resulting computed spherical droplet deformation with the results of experimental research [93-95] including deformation of PDMS spherical droplet in shear flow of viscous media at low-Reynolds numbers. Section 6.2 introduces the results of BSM application to 3-D quasi-steady problem of parabolic shape droplet deformation in Stokes flow. Similarly to 2-D problems in Chapter V, the problem was solved for imported velocity boundary conditions obtained with FVM for the overall flow channel domain in ANSYS Fluent for two different air flow impingement angles - 30^{o} and 45^{o}.

6.1 Validation of BSM for problems of viscous deformation of a spherical PDMS droplet in a horizontal Stokes flow

Viscous droplet deformation in Stokes flow is a popular computational fluid dynamics [93,94] and experimental research problem [95,96]. It is also a useful validation test case for the solutions of more complicated problems of viscous deformation in quasi-steady and unsteady multiphase problems. It has been selected to evaluate the solution algorithm provided in Chapter VI for a 3-D problem of a gas jet flow in a low-Reynolds number region about a molten pitch surface. The problem discussed here has been solved assuming constant air flow in the overall channel domain. Thus, steady-state velocity and pressure fundamental solutions (2-1) – (2-4) were used to solve quasi-steady problem of viscous deformation.

In the present Chapter submerged Stokeslets are used in the BSM algorithm compared to the previous Chapter where Method of Regularized Stokeslets has been employed. This is made in order to apply uniform and local normal Stokeslet allocation schemes discussed in Chapter II for the 3-D droplet surface obtained by rotation of 2-D profile presented in Chapter V about vertical axis. For 2-D Stokeslets these allocation techniques were unnecessary and we can use regularization to save computational time for separate re-allocation of Stokeslets and collocation points.

The geometrical set up and the initial flow field velocity profile is presented at Figure 6-1, which is similar to the one presented in [94].

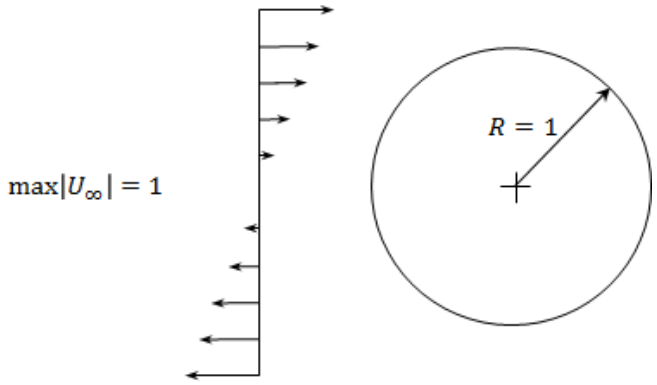

Figure 6-1 Problem set up.

Simplified model of viscous deformation is similar to [95] and represents boundary points' displacement due to shear stress and tangential surface tension exerted by low-Reynolds number air flow.

The resulting shape of the liquid surface is calculated based on the principle that the rate of deformation at every point is proportional to the sum of tangential stresses acting on the respective elementary surface. Similarly to 2-D case, viscous deformation of a spherical droplet is computed as per (5-3) in 3-D notation, where $\bar{x}_i^{new}$ becomes a 3-component coordinate vector of a droplet shape at each iteration; here $\hat{\mathrm{t}}_\mathrm{i}$ is a tangential direction vector to the 3-D surface in point respectively, $s_i -$ local surface tension component for the *i*-th Stokeslet; and the time step was selected $\Delta\bar{t} = 0.01$.

The matrix system of equation (2-1) in 3-D notation is solved with no-slip and no-penetrating velocity boundary conditions set at the channel walls and a droplet surface. For simplicity, the present mathematical model does not presume finding fundamental solution of non-linear Stokes equation with a tangential surface tension as an external

force source term. It rather incorporates surface tension into the balance with the shear stress equation for each surface point after velocity fundamental solution of the linear steady-state Stokes equation is found.

The surface tension in the 3-D case problem of spherical droplet deformation was determined based on the local mean curvature of deformed droplet. It was updated at each time-step using expressions for the first fundamental form of the derived surface:

$$G_{11} = 1 + \left(\frac{\partial \bar{z}}{\partial \bar{x}}\right)^2,\ G_{22} = 1 + \left(\frac{\partial \bar{z}}{\partial \bar{y}}\right)^2, G_{12} = G_{21} = \frac{\partial^2 \bar{z}}{\partial \bar{x} \partial \bar{y}}, \tag{6-1}$$

where G_{ij} are first fundamental forms of the 3-D surface. Then local curvature is determined as follows:

$$\kappa = \sqrt{G_{11}G_{22} - G_{12}^2} \tag{6-2}$$

and then incorporated into the formula (5-6) of the previous Chapter.

Finally, shear stress component acting on a liquid droplet is found based on the following conditions at "gas-liquid" interface:

$$\begin{cases} u_r|_{r=R} = u_\tau|_{r=R} = 0 \\ \tau_{air}|_{r=R} = \tau_{droplet}\big|_{r=R} \end{cases} \tag{6-3}$$

It is possible to express the second condition in terms of shear rates:

$$-\mu_{air} \frac{\partial \overline{u}_{air}}{\partial \hat{n}}\bigg|_{r=R} = -\mu_{droplet} \frac{\partial \overline{u}_{droplet}}{\partial \hat{n}}\bigg|_{r=R} \tag{6-4}$$

Then $\dot{\gamma}_{droplet}$ can be found from (6-5) through the ratio of air and droplet liquid viscosities:

$$\left.\frac{\partial \overline{u}_{droplet}}{\partial \hat{n}}\right|_{r=R} = \frac{\mu_{air}}{\mu_{droplet}} \frac{\partial \overline{u}_{air}}{\partial \hat{n}}_{r=R} \tag{6-5}$$

In the present computation the ratio of fluids' viscosities was taken equal to 0.0012 as in [95].

In the test case formulation, a PDMS-water contact coefficient used in a surface tension component computation is given at a room temperature ($T = 20$°C) and was taken equal to $\gamma_f = 1.9 \cdot 10^{-2} \frac{\mathrm{N}}{\mathrm{m}}$ [97]. In the present problem it was normalized by $\rho \langle U_{local_2} \rangle^2 R_{droplet}$. The dimensionless simulation time in Figure 6-2 was calculated using (4-3).

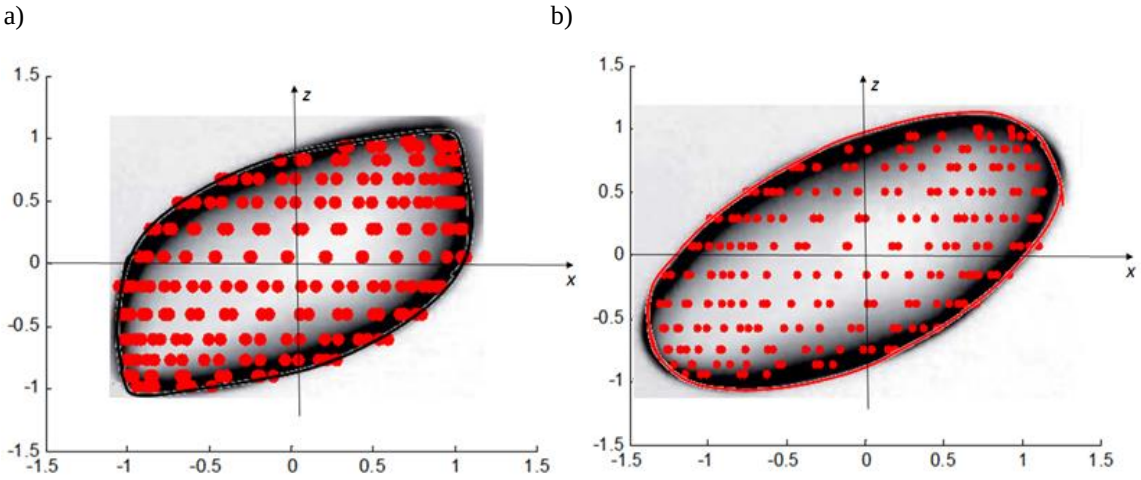

Figure 6-2 Spherical droplet deformation in shear flow at $\bar{t} = 1$: a) corresponding to shear rate 42.7 s^{-1}; b) corresponding to shear rate 14.53 s^{-1}. Photos of deformed droplet images are taken from [95].

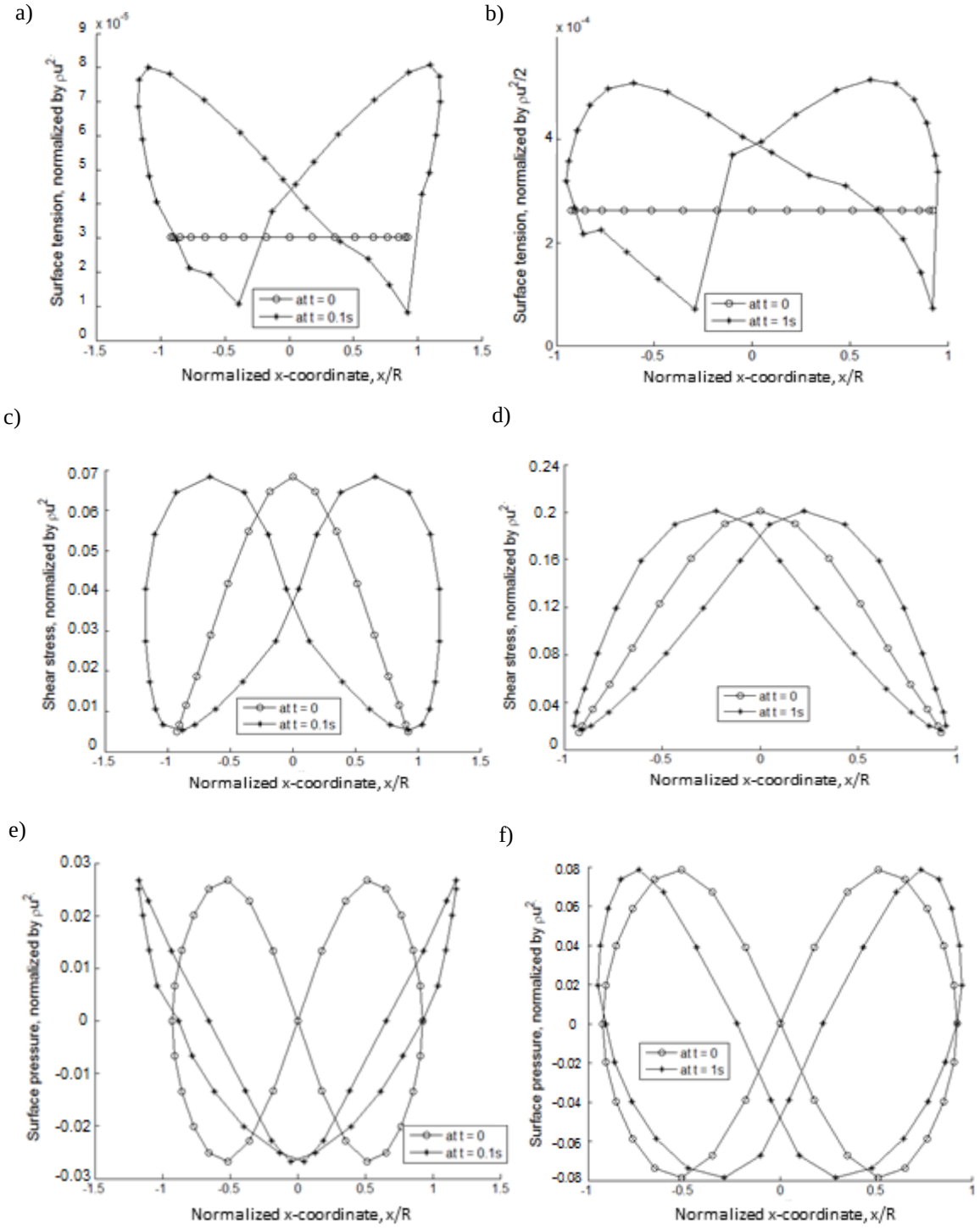

Figure 6-3 Surface stress components in the middle longitudinal section: a), b) surface tension, c), d) shear stress and e), f) pressure corresponding to air flow shear rate 42.74 s^{-1} b) surface tension, d) shear stress and f) pressure corresponding to air flow shear rate 14.53 s^{-1} at $\bar{t} = 0.1$ and $\bar{t} = 1$ respectively.

As it is shown in experiment in [95], the greater shear rates and smaller surface tension result in larger deformation with more intense surface reshaping (Figure 6-2). The shear stress for the purely shear flow about droplet during its' deformation does not differ by much (Figures 6-3c and 6-3d), while surface tension component changes significantly (Figure 6-3a and b).

According to formula (4-3), the maximum dimensionless time determined for simulations validity may be expressed in terms of stress components for pitch droplet was computed in Chapter IV and equal to $\bar{t} = 5$.

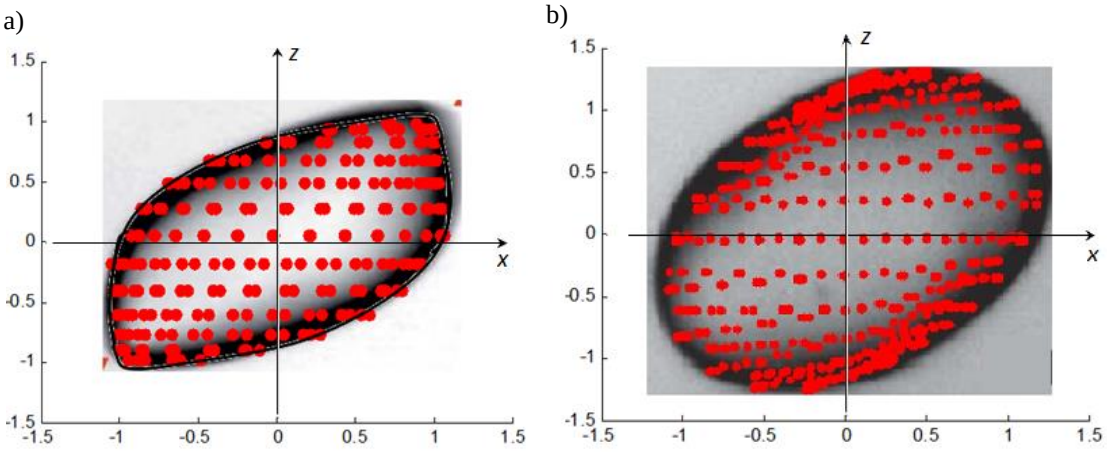

Figure 6-4 Comparison of BSM solution with the experimental data: a) BSM solution at $\bar{t} = 1$ and flow shear rate 42.74 s^{-1}; b) BSM solution at $\bar{t} = 0.1$ and flow shear rate 14.53 s^{-1}. Images of deformed droplet were taken from [95].

In order to determine maximum physical simulation time of viscous droplet deformation, von-Neumann boundary conditions at the interface has been used (6-6). This interface condition is used to evaluate qualitatively viscous deformation of a spherical droplet in shear flow and helps to validate BSM applicability.

Figures 6-2 and 6-4 represent comparison of the BSM numerical simulation and experimental results between droplet deformations at different time and shear rates in the Stokes flow.

From the principle of equality of shear stress between two media, the boundary condition at the air-pitch interface is:

$$-\mu_{air}\frac{\partial\overline{u}_{air}}{\partial\hat{n}}\Big|_{r=R} = -\mu_{pitch}\frac{\partial\overline{u}_{droplet}}{\partial\hat{n}}\Big|_{r=R} \tag{6-6}$$

and the principal deformation is determined by:

$$max|\Delta l| = \frac{max|\tau_f+\sigma|}{\mu_{pitch}}dt, \tag{6-7}$$

The assumption was made that the surface tension contributes to the shape of the deformed droplet and has no sufficient contribution to elongation at small deformation rates, which yields:

$$max|\Delta l| \cong R_{droplet}\frac{max|\tau_f|}{\mu_{pitch}}dt, \tag{6-8}$$

Then total droplet elongation will be:

$$\sum_{i=1}^{n} max|\Delta l| = \frac{R_{droplet}}{\mu_{pitch}}\sum_{i=1}^{n} max\left|\tau_f\right|dt, \tag{6-9}$$

here *n* is a number of time steps. Applying summation of (6-9) over the droplet boundary surface yields:

$$|\Delta l| = R_{droplet}\sum_{i=1}^{n} max\left|\dot{\gamma}_{pitch}\right|dt, \tag{6-10}$$

$$|\Delta l| = R_{droplet} \sum_{i=1}^{n} max \left| \frac{\mu_{air}}{\mu_{pitch}} \dot{\gamma}_{air} \right| dt = n \cdot R_{droplet} max \left| \frac{\mu_{air}}{\mu_{pitch}} \dot{\gamma}_{air} \right| dt =$$

$$R_{droplet} max \left| \frac{\mu_{air}}{\mu_{pitch}} \dot{\gamma}_{air} \right| t, \quad (6\text{-}11)$$

where Δl is a droplet elongation at time *t*.

Using molten mesophase pitch and air viscosity (Figure 4-7, [84] and [98]), the shear rate of the first can be obtained as follows:

$$\dot{\gamma}_{pitch} = \frac{\mu_{air}}{\mu_{pitch}} \dot{\gamma}_{air} = \frac{3.4 \cdot 10^{-5} Pa \cdot s}{100\ Pa \cdot s} \cdot \frac{6.6 \frac{m}{s}}{10^{-6} m} \cong 2.25 s^{-1}$$

In order to satisfy the condition $Re \leq 1$ for the following must be true:$|\Delta l| \leq \frac{L}{2}$, where L is a width of low-Reynolds number region. In the present case, $L = 51 \mu m$ and thus:

$$|\Delta l| \leq 2.55 \cdot 10^{-5} m;$$

Finally, the maximum physical droplet deformation time of 1 mm droplet at a 6.6 m/s before it leaves the region satisfying $Re \leq 1$ condition becomes:

$$t_{max} = \frac{max|\Delta l|}{R_{droplet} max \left| \frac{\mu_{air}}{\mu_{pitch}} \dot{\gamma}_{air} \right|} = .346\ s$$

It is interesting to compare the BSM solution with the numerical simulation results discussed in [99]. The collocation points placed at the 3-D droplet surface then would designate nanoparticles tracing viscous droplet deformations.

6.2 Boundary singularity method solution of 3-D flow for the range of inclinations of jet over the channel bottom

In continuation of the research, a family of 3-D multiphase Stokes flow problems with viscous droplet settling in the channel deformation is considered.

a)

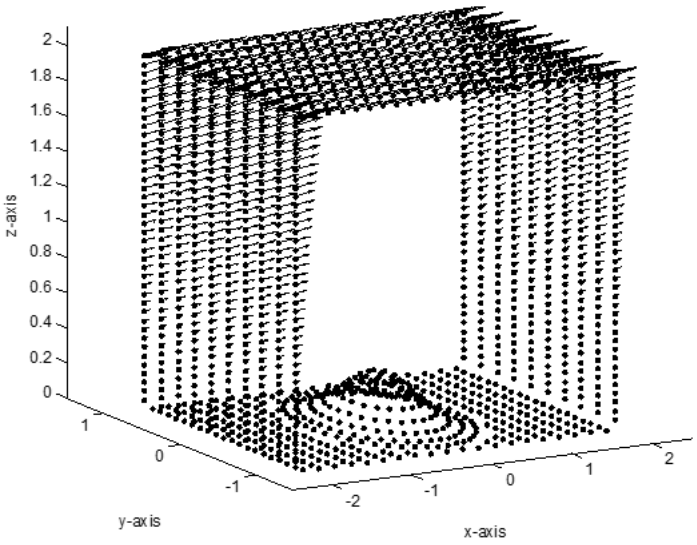

b)

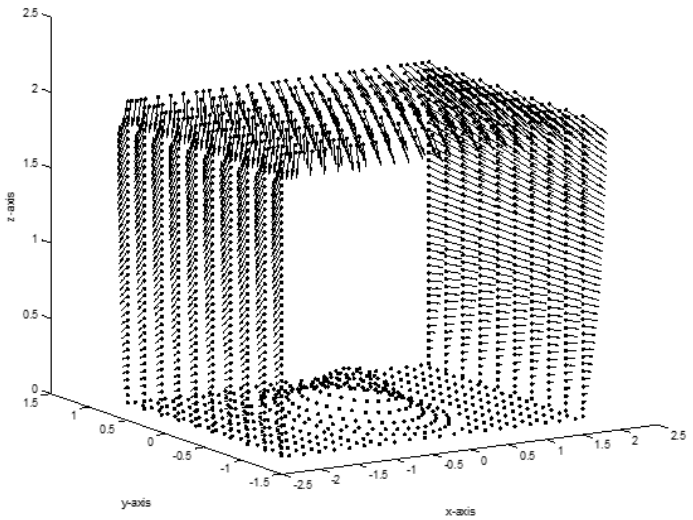

Figure 6-5 Uniform Stokeslets allocation scheme and velocity boundary conditions imported from ANSYS FLUENT (similar to 2-D problems) at different air jet orientation: a) 30 degrees; b) 45 degrees.

As in Chapter V, normalization of each of three coordinates of the Stokeslets and collocation points shown in Figure 6-5 was made by the size of the domain using (5-5). The number of Stokeslets was $N = 1521$ for both flow case problems, as depicted in Figure 6-5.

3-D parabolic droplet model was used in order to simulate smaller scattered pitch film surface perturbations exposed to the surface air flow and causing development of separate nanofiber "embryos".

In order to model 3-D flow over the droplet surface, the flow is considered to be uniform across the channel (in y-direction), therefore planar boundary conditions were imported from ANSYS Fluent solution (Section 5.3) for 2-D velocity vector field in XOZ coordinate plane and replicated into 10 layers generated along y-axis (see Figure 6-5).

The size of the domain was selected $4 \times 4 \times 2$ normalized by the length of the low-Reynolds number region ($L = 21\mu m$). To better represent the initial PDMS droplet shape in the experiment, another parabolic geometry described with the following equation describing the height of a droplet using polar coordinates was adopted:

$$\begin{cases} \bar{x}(\bar{r},\theta) = \bar{r}cos(\theta); \\ y(r,\theta) = \bar{r}sin(\theta); \\ \bar{z}(\bar{r},\theta) = m(1-\bar{r}^2)^3, \;\; \bar{x}^2+\bar{y}^2 < 1 \;\; and \; 0, \quad otherwise \end{cases} \tag{6-12}$$

where $m = 0.36$. $\bar{r}, \theta$ are polar coordinates first normalized by the size of the domain and introduced in (2-8) of Chapter II for regular and modified Cassini ovals.

The physical problem formulation is identical to 2-D case problems discussed in the Section above.

a)

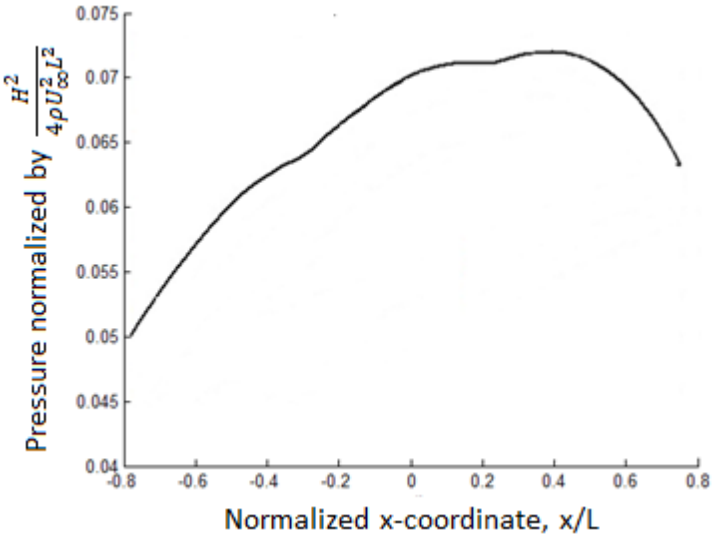

b)

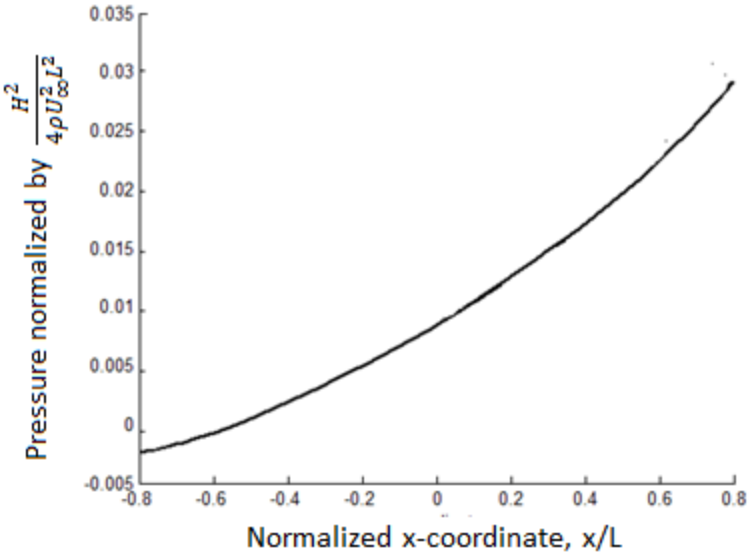

Figure 6-6 Pressure computed with BSM for Stokes flow about 3-D parabolic droplet: a) 45 degrees air flow; b) 30 degrees air flow

Following recommendation given in Chapter II, the Stokeslet allocation depth parameter was taken equal to $\overline{D} = 0.001$ for the domain boundary points based on the considered flow domain length, and $\overline{D} = 0.03$ is the Stokeslet allocation depth selected for the droplet based on its' radius.

a)

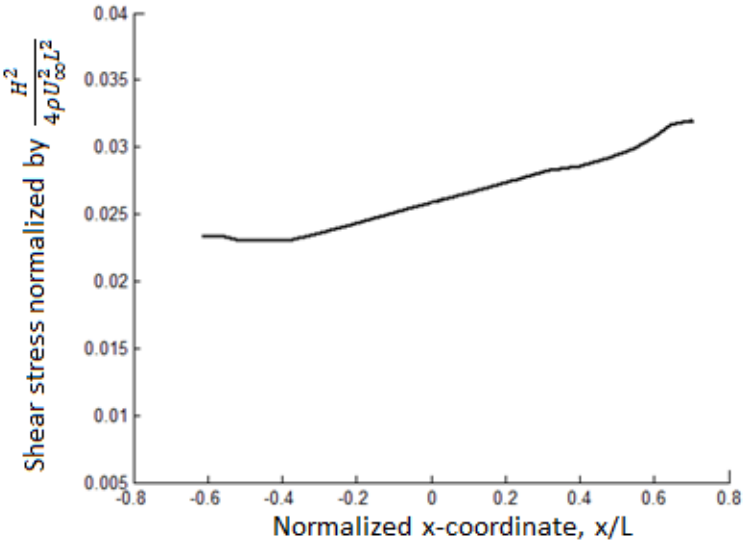

b)

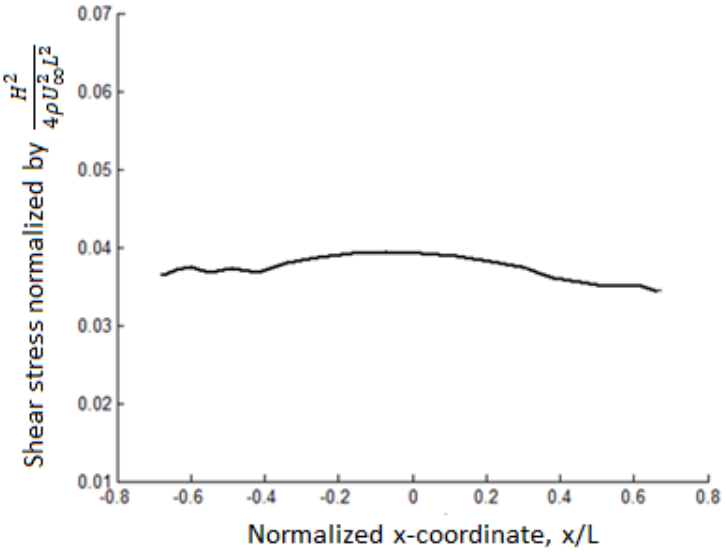

Figure 6-7 Shear stress computed with BSM for Stokes flow about 3-D parabolic droplet: a) 30 degrees air flow; b) 45 degrees air flow

Like in the previous cases, the solution includes the velocity vector field in the middle section of the specified microscale domain surface tension and shear stress.

The resulting middle section velocity vector fields for both 30 and 45 degrees flow cases look very similar to the ones computed for the respective 2-D flow cases (see Figure 5-22). For that reason they are omitted here assuming the domain and the droplet profiles are identical to the ones presented in 2-D model.

For the 30^o flow case one may notice larger pressure and stress magnitude changes along the surface. The smaller stress gradients about droplet surface for 45^o flow case result in less intensive deformations and shape changes.

a) b)

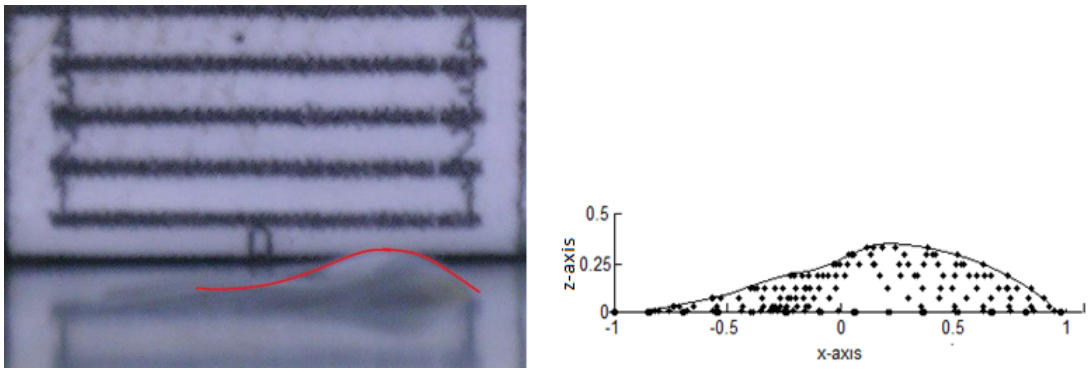

Figure 6-8 Deformation of PDMS droplet and BSM simulation results for 3-D parabolic droplet model in case of 30 degrees air flow at $\bar{t} = 1$.

This is also demonstrated with the experimental deformation profiles of 3-D droplet after $\bar{t} = 5$ (Figures 6-8a and 6-9a) and deformation simulation results for the parabolic

droplet after $\bar{t} = 1$ computed with BSM (Figures 6-8b and 6-9b). Normalization of coordinates was made by the size of the domain using (5-5).

a) b)

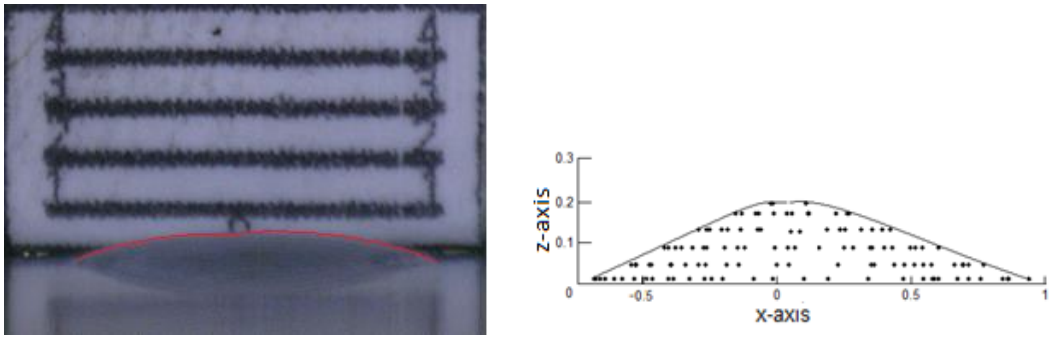

Figure 6-9 Deformation of PDMS droplet and BSM simulation results for 3-D parabolic droplet model in case of 45 degrees air flow $\bar{t} = 1$.

The scattered dots in Figures 6-8 and 6-9 depict collocation points that track respective displacement of the boundary points after droplet deformation. In Figure 6-8 one can see denser package of points in the trailing (left) part of the droplet along the flow and the leading part of the droplet, while middle part point distribution is rarified. It allows for tracking redistribution of liquid over the droplet and estimate relative deformation around droplet.

It is easy to see that pressure and shear stress components for the 2-D case shown in Figures 5-22 and 5-23 of the previous Chapter exhibit larger gradients over the track surface than those presented in Figures 6-6 and 6-7 for the 3-D droplet. This leads to smoother transitions of deformation profile in the case of droplet as it can be seen in Figures 6-8 and 6-9 compared to the Figures 5-25 and 5-26.

This effect can also be observed comparing the 3-D droplet and the 2-D PDMS track experimental deformation images and simulation results in case of 45 degrees air flow. The comparison of the droplet and track deformation profiles reveals the difference in deformation amplitude for the 3-D droplet and the 2-D track. The deformation of the 3-D droplet is smaller than it is observed for the 2-D track (see Figures 5-26 and 5-27). Total surface area of the latter and consequently drag induced by air stream is greater.

After BSM with a quasi-steady algorithm was applied and the resulting deformed surface 3-D coordinates are found, the following procedure to obtain FV solution can be used to compute further deformations at higher Reynolds number regions where BSM is not applicable:

1) The resulting surface 3-D coordinates are exported from Matlab BSM code to an AutoCAD-readable format data file;

2) File with coordinates is split into multiple files representing coordinates of cross-sections, with coordinates of each "slice" of the surface and finally constructing a 3D pitch wiggle surface and body;

3) Constructed AutoCAD 3D-model is exported as *.iges file, which is readable by ANSYS DesignModeler application;

4) Finally, obtained geometry *.iges data file was uploaded into ANSYS® FLUENT and the simulation were performed as described above.

The proposed 4-step procedure may be used to perform simulations of the liquid pitch surface perturbation propagation at higher Reynolds number when it leaves the stagnation

flow region. The new coordinates after the last iteration in BSM quasi-steady solution algorithm are used to generate surface 3-D model in ANSYS Fluent and perform respective flow simulations to simulate multiphase flow and trace fiber growth inside and nozzle.

Further extension of the problem both in 2-D and 3-D formulation is possible assuming high frequency pulsating flow and non-stationary flow field redistribution in vicinity of liquid surfaces in flow stagnation regions. This requires application of unsteady velocity and pressure fundamental solutions (Appendix B).

CHAPTER VII

CONCLUDING REMARKS

In the present Dissertation the Boundary Singularity Method (BSM) was optimized in terms of needed computational resources and convergence and then applied to problems of determination of drag force exerted on non-spherical particles and on particle interacting with fiber in filtration problem. BSM was combined with FVM for the first time and applied to deformation of liquid droplets in synthesis of submicron fibers.

Location of singularities is crucial for obtaining a Stokes flow solution using BSM with moderate number of singularities. Optimization of Stokeslets' allocation substantially reduces computational time for Stokes flows about geometrical shapes typical for merging particles in multi-phase flows.

First, allocation of Stokeslets was considered at submerged surfaces geometrically similar to the shapes of pairs of particles. Non-uniform and uniform distributions of Stokeslets and collocation points at these surfaces were compared. For non-uniform distributions the number of Stokeslets and collocation points per cross-section remains the same while for uniform distributions the number of singularities and collocation points per unit area remains the same. The former scheme is particularly simple in implementation while the latter shows convergence in terms of Stokes force for approximately halved number of Stokeslets.

To further reduce the needed number of Stokeslets, new Stokeslet allocation schemes were proposed and implemented to Stokes flows about merging particles. New Stokeslets' allocation method was denoted as the local normal scheme in which singularities are located at straight lines connecting the particle dividing line (symmetry line for symmetric particles) with the points at this surface. These lines are locally normal to the particle surface. The depth of submergence of Stokeslets along these lines serves as a parameter of the scheme.

To improve the efficiency of local normal scheme, combined scheme was proposed that uses the local normal approach for convex regions and similar shape scheme with uniform allocation of singularities for concave regions near inflexion points. The combined scheme allows for different depth of submergence of a surface formed with Stokeslets' for convex and concave regions.

For proposed Stokeslet allocation schemes (local normal and combined), the required CPU time to solve a Stokes flow reduces 6 to 30 times depending on the considered shape of cluster of particles, with a needed number of singularities reduced 4 to 6 times compared to traditional allocation of Stokeslets at geometrical surface similar to the particle surface.

To apply the proposed approach, Stokes flows were computed about pairs of particles ranging from longitudinal to transversal orientations with respect to flow. For pair of separated spherical particles, the solution was verified using computational and analytical results obtained in previous studies. The proposed approach is shown to be instrumental

to obtain Stokes force and flow field around fused particles at different stages of their merging using moderate number of Stokeslets.

In the future research the approach will be extended to efficient computation of Stokes force for transient 3-D problems of particles' dynamics with partial slip boundary conditions.

Simulation of a Stokes flow about droplet sticking to cylindrical fiber and about “peanut-shape” cluster of merging droplets was performed and comparison of traditional versus proposed Stokeslet allocation schemes was presented. Traditional Stokeslet allocation schemes combine non-uniform similar-shape scheme for spherical droplet and “peanut-shape” cluster and “equidistant” scheme for cylindrical fiber, while proposed scheme include “non-equidistant” (exponential) submergence depth for cylindrical fiber and uniform similar-shape scheme for spherical droplet and “peanut-shape” cluster. The large condition number of the computational matrix M and consequent inaccuracy in solution at the point of contact and adjacent areas has been cured with smaller Stokeslets allocation depth at those areas.

The resulting solution using BSM together with the proposed scheme of allocation of singularities shows growth of total drag with the increase of settling droplet radius. Evaluation of the results obtained for a Stokes flow about the droplet-fiber system shows that the maximum drag is achieved when the angle between the far-field flow vector and direction from the fiber axis to droplet center is 45^{o}.

In the simplified problem of air flow in the channel over viscous deformable surface describing one of processes inside NGJ nozzle, Stokes flow problem in stagnation regions has been solved using overall domain velocity vector field as the boundary conditions (BC). The BC velocity vector field was obtained by solving Navier-Stokes equations using FVM for the entire channel domain. The quasi-steady algorithm was introduced for a surface reshaping after each time step during viscous deformation derived from the sum of tangential stresses.

Simulation of 2-D tracks and 3-D parabolic droplet deformations show good qualitative correspondence with experimental results for PDMS tracks and droplets presented in Chapter IV. The experiment was attempted to physically model essential features of pitch deformation and elongation in particular locations of air-liquid reaction zone of NGJ nozzle in terms of geometry, air-liquid viscosity ratios and air flow Reynolds number in vicinity of liquid droplets and tracks.

Further BSM simulations of viscous deformation of liquids in low-Reynolds number flows are planned with application of complete solution of unsteady Stokes equation presented in Appendix B.

REFERENCES

[1] S. Zhao, A. Povitsky, Method of Fundamental Solutions for Partial-slip Fibrous Filtration Flows. Int. J. Numer. Methods Fluids, 61 (2009) 255–274.

[2] S. Zhao, A. Povitsky, A Hybrid Molecular and Continuum Method for Low-Reynolds-Number Flows. Nonlinear Analysis, 71 (2009) 2551–2564.

[3] S. Zhao, A. Povitsky, Method of Submerged Stokeslets for Slip Flow about Ensembles of Particles. J. Nanosci. Nanotechnol, 8:7 (2008) 3790–3801.

[4] S. Zhao, A. Povitsky, Three-dimensional Boundary Singularity Method for Partial-Slip Flows. Eng. Anal. Bound. Elem, 35 (2011) 114-122.

[5] S. Zhao, Development of Boundary Singularity Method for Partial-Slip and Transition Molecular-Continuum Flow Regimes with Application to Filtration. PhD dissertation, The University of Akron, 2009. Advisor: A. Povitsky http://etd.ohiolink.edu/view.cgi?acc_num=akron1247718304

[6] Y. Gu, W. Chen, X.-Q. He, Singular boundary method for steady-state heat conduction in three dimensional general anisotropic media, International Journal of Heat and Mass Transfer 55 (2012) 4837–4848.

[7] W. Chen, Y. Gu, An Improved Formulation of Singular Boundary Method, Advances in Applied Mathematics and Mechanics. 4:5 (2012) 543-558.

[8] Y. Aboelkassem, A.E. Staples, Stokeslets-meshfree computations and theory for flow in a collapsible micro-channel, Theor. Comput. Fluid Dyn, 27 (2012) 681-700.

[9] H. Zhou, C. Pozrikidis, Adaptive Singularity Method for Stokes Flow Past Particles. J. Comput. Phys, 117 (1995) 79–89.

[10] S. Hosseini, H. Tafreshi, Modeling particle-loaded single fiber efficiency and fiber drag using ANSYS–Fluent CFD code, Computers & Fluids 66 (2012) 157–166.

[11] R.J. Clarke, O.E. Jensen et al, Three-Dimensional Flow due to a Micro- Cantilever Oscillating near a Wall: an Unsteady Slender-body Analysis, Proc. R. Soc. A. 462 (2006) 913-933.

[12] A. Tornberg, M.J. Shelley, Simulating the Dynamics of Interactions of Flexible Fibers in Stokes Flows, Journal of Computational Physics 196 (2004) 8–40.

[13] S. Zhao, A. Povitsky, Coupled Continuum and Molecular Model of Flow through Fibrous Filter, Physics of Fluids, Vol 25:11(2013).

[14] S.K. Veerapaneni, A. Rahimian, G. Biros, D. Zorin, A fast algorithm for simulating vesicle flows in three dimensions, Journal of Computational Physics 230 (2011) 5610-5634.

[15] A. Rahiman et al, Petascale direct numerical simulation of blood flow on 200K cores and heterogeneous architectures. SC10 (2010) Proceedings of the 2010 ACM/IEEE International Conference for High Performance Computing, Networking, Storage and Analysis, (2010) 1-11.

[16] C. Pozrikidis, Boundary Integral and Singularity Methods for Linearized Viscous Flow. Cambridge University Press, New York, USA, 1992.

[17] C.C. Tsai, D.L. Young, C.W. Chen and C.M. Fan, The method of fundamental solutions for eigenproblems in domains with and without interior holes, Proceedings of the Royal Society A, 462 (2006) 1443-1466.

[18] G.K. Batchelor, Slender-body theory for particles of arbitrarily cross-section in Stokes flow, Journal of Fluid Mechanics, 44 (1970) 419-440.

[19] R.G. Cox, The Motion of Long Slender Bodies in a Viscous Fluid, Part 1. General theory, Journal of Fluid Mechanics, 44 (1970) 791-810.

[20] R.E. Johnson, C.J. Brokaw, Flagellar Hydrodynamics. A Comparison Between Resistive-Force Theory and Slender-Body Theory, Biophysical Society, 25:1 (1979) 113-127.

[21] R. Cortez, M. Nicholas, Slender Body Theory for Stokes Flows with Regularized Forces, Comm. App. Math. and Comp. Sci. 7:1 (2012) 33-62.

[22] O. Marin, Quadrature Rules for Boundary Integral Methods Applied to Stokes Flow, Licentiate Thesis in Numerical Analysis, KTH School of Computer Science and Communication, 2011 KTH/SCS/A-11/01-SE 928-91-2415-862-5.

[23] L. Elemi, F. Feuillebois, Green Function for a Stokes Flow near a Porous Slab, ZAMM. Angew. Math. Mech. 81:11 (2001) 743–752.

[24] J. Ainley et al, The method of Images for Regularized Stokeslets. Journal of Computational Physics, 227 (2008) 4600-4616.

[25] M.E. Staben, A.Z. Zinchenko, R.H. Davis. Motion of a Particle Between Two Parallel Walls in Low-Reynolds Number Poiseuille Flow. Phys. Fluids, 15 (2003) 1711–1733.

[26] M.E. Staben, Low-Reynolds-Number Particle Transport in Narrow Channels for Microfluidics and Other Applications, University of Colorado, In partial fulfillment of the requirement for the degree of Doctor of Philosophy, 2005.

[27] S. Bhattacharya, J. Blawzdziewicz, Image system for Stokes-flow singularity between two parallel planar walls, J. Math. Phys, 43:11 (2002) 5720-5732.

[28] G.E. Karniadakis, A. Beskok, Microflows: Fundamentals and Simulation, New York: Springer-Verlag, 2002.

[29] R. Cortez, L. Fauci, A. Medovikov, The Method of Regularized Stokeslets in Three Dimensions: Analysis, Validation, and Application to Helical Swimming, Physics of Fluids, 17:3 (2005) 031504-1-14.

[30] L. Nitsche, P. Parthasarathi, Cubically Regularized Stokeslets for Fast Particle Simulations of Low-Reynolds-Number Drop Flows, Chemical Engineering Communications, Taylor & Francis, 197:1 (2009) 18-38.

[31] E.J. Lobaton, A.M. Bayen, Modeling and Optimization Analysis of a Single-Flagellum Micro-Structure through the Method of Regularized Stokeslets, IEEE Transactions on Control Systems Technology, 17:4 (2009) 907-916.

[32] D.L. Young et al, Method of fundamental solutions for multidimensional Stokes equations by dual-potential formulation, European Journal of Mechanics - B/ Fluids 25:6 (2006) 877–893.

[33] D.J. Smith, A Boundary Element Regularized Stokeslet Method Applied to Cilia- and Flagella-Driven Flow, Proceedings of The Royal Society, UK, 465:2112 (2009) 3605-3626.

[34] R. Cortez. The Method of Regularized Stokeslets. SIAM J. Sci. Comput. 23:4 (2001) 1204–1225.

[35] J. Lin et al, A New Investigation into Regularization Techniques for the Method of Fundamental Solutions, Mathematics and Computers in Simulation, 81:6 (2011) 1144–1152.

[36] O. Gonzalez, J. Li, An Analysis of the Regularized Stokeslet Method. Department of Mathematics, Univ. of Texas, Austin. Preprint submitted to Applied Mathematics and Computation, 2011, 19 pages;
http://www.ma.utexas.edu/users/og/PUBLICATIONS/paper_StokesRegular.pdf

[37] C.S. Peskin, The Immersed Boundary Method, Acta Numerica, 11 (2002) 479-517.

[38] A.A. Hyman, C.A. Weber, F. Julicher, Liquid-Liquid Phase Separation in Biology, Annu. Rev. Cell Dev. Biol. 30 (2014) 39–58.

[39] D.L. Young, C. Chen, C.M. Fan, K. Murugesan, C.C. Tsai, The method of fundamental solutions for Stokes flow in a rectangular cavity with cylinders. Journal of Mechanics, 24:6 (2005) 703-716.

[40] C.W. Chen, D.L. Young, C.C. Tsai, K. Murugesan. The method of fundamental solutions for inverse 2D Stokes problems, Comput Mech, 37:1 (2005) 2–14.

[41] D.L. Young, S.J. Jane, C.M. Fan, K. Murugesan, C.C. Tsai, The method of fundamental solutions for 2D and 3D Stokes problems, Journal of Computational Physics, 211:1 (2005) 1-8.

[42] D.L. Young, C.W. Chen and C.M. Fan, The method of fundamental solutions for low Reynolds number flows with moving rigid body, In Y.S. Smyrlis, C.S. Chen, A. Karageorghis, editor, The Method of Fundamental Solutions – A Meshless Method, Dynamics Publishers Inc. USA, (2008) 181-206.

[43] C. Chen, A. Karageorghis, Y. Smyrlis, The Method of Fundamental Solutions – A Meshless Method, Dynamic Publishers Inc., USA, (2008), 338 pages.

[44] D.L. Young, Y.C. Lin, C.M. Fan, C.L. Chiu, The method of fundamental solutions for solving incompressible Navier–Stokes problems, Engineering Analysis with Boundary Elements, 33:8-9 (2009) 1031-1044.

[45] C.C. Tsai, D.L. Young, D. Lo, T. Wong, Method of Fundamental Solutions for Three-Dimensional Stokes Flow in Exterior Field, J. Eng. Mech, 132:3 (2006) 317–326.

[46] V. Meleshko, Steady Stokes Flow in a Rectangular Cavity, Proceedings Mathematical Physical and Engineering Sciences, 452:1952 (1996) 1999-2022.

[47] D.L. Young, J.T. Wu and C.L. Chiu, Method of Fundamental Solutions for Stokes Problems by the Pressure-Stream Function Formulation, Journal of Mechanics, 24:2 (2008) 137–144.

[48] C.S. Chen, M.A. Goldberg, R.S. Schaback, Recent developments in the dual reciprocity method using compactly supported radial basis functions, eds. Y.F. Rashed and C.A. Brebbia, Transformation of Domain Effects to the Boundary. Southampton, Boston: WIT Press, (2003) 183-225.

[49] C.C. Tsai, D.L. Young, C. Fan, M. Chen, MFS with Time-Dependent Fundamental Solutions for Unsteady Stokes Equations, Engineering Analysis with Boundary Elements, 30:10 (2006) 897–908.

[50] H.Y.Wang, F. Dong, A Method for Bubble Volume Calculating in Vertical Two-Phase Flow, Journal of Physics: Conference Series 147 (2009) 012018.

[51] A.L. Yarin, S. Sinha-Ray, B.Pourdeyhimi, Meltblowing: Multiple polymer jets and fiber-size distribution and lay-down patterns, Polymer 52 (2011) 2929e2938.

[52] R. Benavides, "Gas Jet Process for Production of Sub-micron Fibers." Electronic Thesis or Dissertation. University of Akron, 2013. OhioLINK Electronic Theses and Dissertations Center. 2014.

[53] A.J. Kassab et al, BEM/FVM conjugate heat transfer analysis of a three-dimensional film cooled turbine blade, Int. Jour. of Num. M. for Heat & Fluid Flow, 13:5(2003)581-610.

[54] H. Li, A.J. Kassab, 1994, "A Coupled FVM/BEM Approach to Conjugate Heat Transfer in Turbine Blades," AIAA/ASME Sixth Joint Thermophysics Conference, Colorado Springs, CO, June 20–23, AIAA Paper No. 94-1981.

[55] S. C. Chapra, Applied Numerical Methods with MATLAB for Engineers and Scientists, Third Edition, McGraw Hill, 2012 p. 266.

[56] H. Schlichting, Boundary-layer Theory, McGraw Hill, 1979, 817 pages.

[57] H.Hasimoto, O.Sano, Stokeslets and Eddied in Creeping Flow, Fluid Mechanics, 12 (1980) 335–363.

[58] T. Ruberg, M. Schanz, An Alternative Collocation Boundary Element Method for Static and Dynamic Problems, Comput Mech, 44 (2009) 247–26.

[59] M.A. Goldberg, C.S. Chen, The Method of Fundamental Solution for Potential and Helmholtz and Diffusion Problems In Boundary Integral Methods –Numerical and Mathematical Aspects (ed. Goldberg MA), CMP, 1998, 76-103.

[60] L. Elasmi, M. Berzig, F. Feuillebois, Stokes Flow for the Axisymmetric Motion of Several Spherical Particles Perpendicular to a Plane Wall, ZAMP, 54:2 (2003) 304-327.

[61] A.M. Ardekani, R.H. Rangel, Unsteady Motion of Two Solid Spheres in Stokes Flow, Physics of Fluids, 18:10 (2006) 103306-1-14.

[62] A.B. Basset, An Elementary Treatise on Cubic and Quartic Curves. London: Deighton Bell and Co, 1901.

[63] J.D. Lawrence, A Catalog of Special Plane Curves, New York, Dover, 1972, 218 pages.

[64] E. Lorenceau, C. Clanet, and D. Quere, Capturing Drops with a Thin Fiber, Journal of Colloid and Interface Science, 279 (2004) 192-197.

[65] L.V. Wijngaarden, Hydrodynamic interaction between gas bubbles in liquid, J. Fluid Mech. 77:1 (1976) 27-44**.**

[66] A. Moshfegh et al, A Novel Slip Correction Factor for Spherical Aerosol Particles, World Academy of Science, Engineering and Technology, 27 (2009) 709-715.

[67] A.G. Goldman, R.G. Cox, H. Brenner, The Slow Motion of Two Identical Arbitrarily Oriented Spheres Through a Viscous Fluid, Chemical Engineering Science, 21 (1966) 1151-1170.

[68] M. Zabarankin, Asymmetric Three-Dimensional Stokes Flow about Two Fused Equal Spheres, Proc. R. Soc. A, 463 (2007) 2329-2350.

[69] C.J. Lin, K.J. Lee, N.F. Sather, Slow Motion of Two Spheres in a Shear Field, J. Fluid Mech. 43 (1970) 35–47.

[70] M.S. Ingber, A. Zinchenko, Semi-analytic Solution of the Motion of Two Spheres in Arbitrarily Shear Flow. International Journal of Multiphase Flow, 43 (2012) 152-163

[71] B.J. Kirby, Micro- and Nanoscale Fluid Mechanics: Transport in Microfluidic Devices, Cambridge University Press, New York, USA, 2010.

[72] A. Haider, O. Levenspiel, Drag Coefficient and Terminal Velocity of Spherical and Nonspherical Particles, Powder Technology, 58 (1989) 63-70.

[73] M. Hartman, V. Havlin, O. Trnka, M. Carsky, Predicting the free-fall velocities of spheres, Chem.Eng.Sci., 44:8 (1989)1743-1745.

[74] L.C. Wrobel, The Boundary Element Method, John Wiley & Sons Ltd., 2002, vol.1, 468p.

[75] M.A. Mikhaylenko, A. Povitsky, Optimal Allocation of Boundary Singularities for Stokes Flows About Pairs of Particles, Engineering Analysis with Boundary Elements, 41 (2014) 122-138.

[76] S.A. Hosseini, H.V. Tafreshi, Modeling droplet-loaded single fiber efficiency and fiber drag using ANSYS–Fluent CFD code, Computers & Fluids 66, pp. 157–166, 2012.

[77] G. Viswanadam, G.G. Chase, Contact angles of drops on curved super-hydrophobic surfaces, Journal of Colloid and Interface Science, 367(1), pp. 472-477, 2012.

[78] P. Kulkarni, S.U. Patel, G.G. Chase, Layered Hydrophilic/ Hydrophobic Fiber Media for Water-in-Oil Coalescence, Sep Pur Tech, 85, pp. 157-164, 2012.

[79] D. Winkler, K. Kissling, S. Schütz, A. Werfl, M. Piesche, Numerical simulation of droplet-fiber-interactions in water/diesel coalescence filters, Proceedings of AFS 2010 Annual Conference & Exposition, 2010, San Antonio, TX USA.

[80] J.A. Fay, Introduction to Fluid Mechanics, MIT Press, 1994, p.474.

[81] M. Mikhaylenko, A. Povitsky, Boundary Singularity Method for Droplet-Fiber Interaction, Boundary Elements and Other Mesh Reduction Methods XXXV, New Forest, UK; 01/2013.

[82] A.L. Yarin, G.G. Chase, Liquid Drop Growth on a Fiber, AIChE Journal, 52(1), pp. 217-227, 2006.

[83] Silicone Fluids: Stable Inert Media, Gelest, Inc., 1998, 25pp. http://www.gelest.com/goods/pdf/siliconefluids.pdf.

[84] M. Dumont, M.A. Dourges, R. Pailler, X. Bourrat, Mesophase pitches for 3-D carbon fibre preform densification: rheology and processability, Fuel, 82(2003)1523-1529.

[85] Z.Z. Tian, M.D. Kyte, C.J. Messer, Parallax Error in Video-Image Systems, Journal of Transportation Engineering, 128(2002)218-223.

[86] Z.Z. Tian, M.D. Kyte, C.J. Messer, Parallax Error in Video-Image Systems, Journal of Transportation Engineering, 128(2002)218-223.

[87] R. Benavides, Gas Jet Process for Production of Sub-Micron Fibers, Doctoral Dissertation, The University of Akron, 2013.

[88] H. Fry, A study of Droplet Deformation, PhD Dissertation, University College London, 2011, 205pp.

[89] S.C. Chapra, Applied Numerical Methods with MATLAB, 2nd edition, McGraw Hill, 2008, 588pp.

[90] D.P. Gaver, S.M. Kute, A Theoretical Model Study of the Influence of Fluid Stresses on a Cell Adhering to a Microchannel Wall, Biophysical Journal, 75, pp.721-733, 1998.

[91] M.A. Biot, Mechanics of Incremental Deformations, John Wiley & Sons, Inc., New York/London/Sydney,1965, pp.86-88.

[92] P. Dimitrakopoulos, Deformation of a Droplet Adhering to a Solid Surface in Shear Flow Onset of Interfacial Sliding, J. Fluid Mechanics, 580 (2007) 451-466.

[93] H. Hua et al, Effect of confinement on droplet deformation in shear flow, International Journal of Computational Fluid Dynamics, 27 (2013) 8–10, p.p.317–331.

[94] A.E. Komrakova, O. Shardt, D. Eskin, J.J. Derksen, Lattice Boltzmann simulations of drop deformation and breakup in shear flow, International Journal of Multiphase Flow, 59 (2014) 24-43.

[95] I. Koleva, H. Rehage, Deformation and orientation dynamics of polysiloxane microcapsules in linear shear flow, Soft Matter, 8 (2012) 3681-3693.

[96] L. Changzhi, G. Liejin, Experimental Study of Drop Deformation and Breakup in Simple Shear Flows, Chin. J. Chem. Eng., 15 (2007) 1, pp.1-5.

[97] A.W. Adamson, A.P. Gast, Physical chemistry of surfaces, 6^{th} edition, Wiley, 1997.

[98] K. Kadoya, N. Matsunaga, A. Nagashima, Viscosity and Thermal Condictivity of Dry Air in the Gaseous Phase, J.Phys.Chem.Ref.Data, Vol.14, No.4, 1985.

[99] S. Frijters, F. Gunther, J. Harting, Effects of nanoparticles and surfactant on droplets in shear flow, Soft Matter, 8(2012)24.

[100] I.G. Currie, Fundamental Mechanics of Fluids, 2nd Ed., McGraw-Hill, Boston (1993).

APPENDICES

APPENDIX A

BASIC RELATIONS IN STOKES FLOW PROBLEMS USED IN THE RESEARCH

Analytical solution for the Stokes force about the sphere with radius *R* is well known:

$$F_{Stokes} = 6\pi\mu R U_{\infty} \tag{A-1}$$

where μ is a dynamic viscosity of the flow media and U_{∞} is a far-field uniform velocity. For normalized values of $\mu, R,$ and U_{∞} equal to unity, the $F_{Stokes} = 6\pi$. Here F_{Stokes} is a force exerted at the sphere surface exposed to the uniform by φ flow (see Figure A-1b) and can be calculated a sum of surface integrals of normal stress and shear stress:

$$\begin{gathered} \tau = -\mu\left(r\frac{d}{dr}\left(\frac{u_\theta}{r}\right)+\frac{1}{r}\frac{du_r}{dr}\right) = \frac{3}{2}\frac{\mu U_\infty sin\theta}{R}, \quad F_{shear} = 2\pi\int_0^\pi \tau\cdot sin\theta\cdot R^2 sin\theta d\theta \\ -p+2\mu\frac{du_r}{dr} = \frac{3}{2}\frac{\mu U_\infty cos\theta}{R}, \; F_{normal} = 2\pi\int_0^\pi \sigma\cdot cos\theta\cdot R^2 sin\theta d\theta \end{gathered} \tag{A-2}$$

where r is a radial coordinate and θ is an angular coordinate of the spherical coordinate system (Figure A - 1), u_θ and u_r are velocity vector components, τ is a shear stress and σ is a normal stress at the sphere surface.

Flow field velocity is given by:

$$\begin{cases} u_r = U_\infty \cos\theta\cdot\left(1-\frac{3R}{2r}+\frac{R^3}{2r^3}\right) \\ u_\theta = U_\infty \sin\theta\cdot\left(1-\frac{3R}{4r}-\frac{R^3}{4r^3}\right) \end{cases}, \tag{A-3}$$

where u_r and u_θ are radial and tangential velocity vector components in spherical coordinate system (Figure A-1).

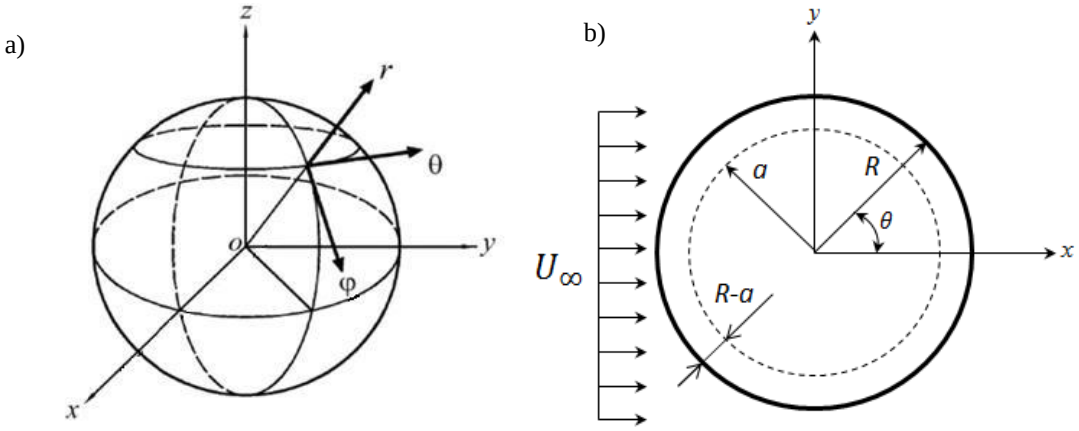

Figure A-1 Stokes flow problem: a) spherical coordinate system and b) geometrical formulation of flow about sphere.

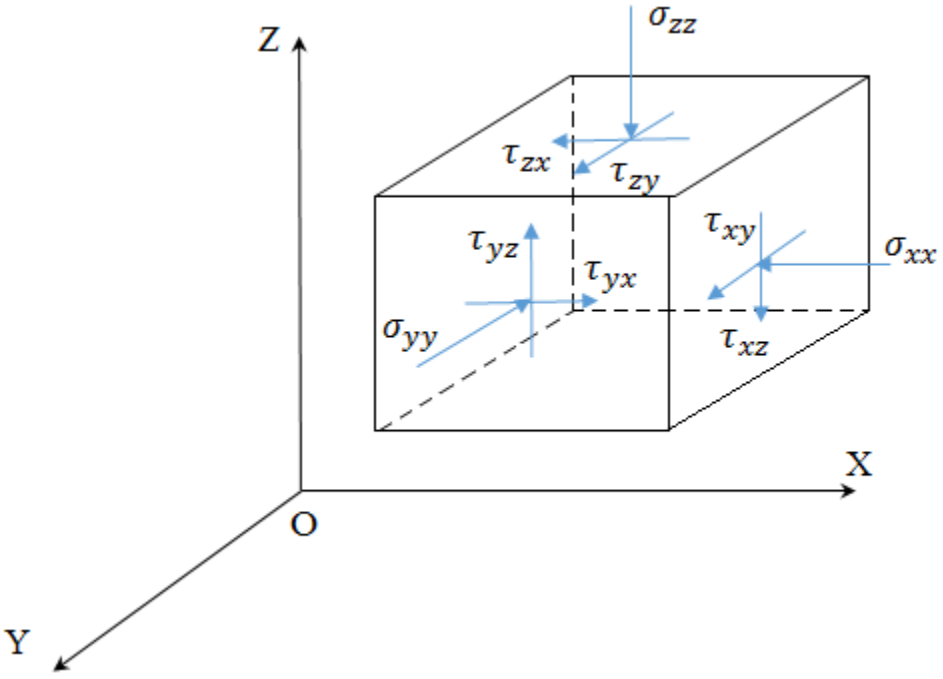

Figure A-2 Stress tensor components on infinitesimal cube

APPENDIX B

COMPLETE FUNDAMENTAL SOLUTION OF THE UNSTEADY STOKES EQUATION

Appendix B introduces derivation of a complete solution of the system of 3-D unsteady Stokes and a continuity equations and its' validation with 2-D and 3-D Stokes first problem.

B-1 Derivation of 3-D Steady-state Stokeslets

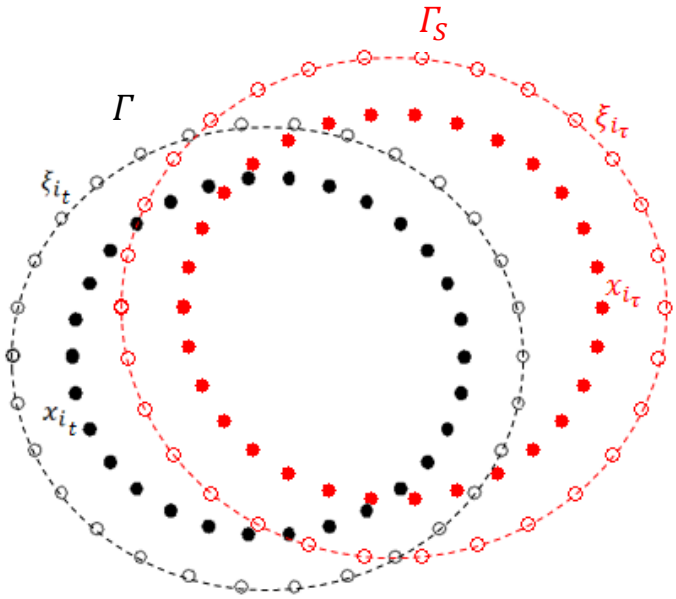

Figure B-1 Stokeslets and collocation points in unsteady circular domain

Consider Cauchy problem for unsteady Stokes equation in $\mathcal{R}^3$. The solution of the problem represents generalized solution of the partial differential equation with invariable RHS, which nulls at $t < 0$,

$$\begin{cases} \frac{1}{\rho}\frac{\partial u^k(x,\xi;t,\tau)}{\partial t} - \nu\nabla^2 u^k(x,\xi;t,\tau) = -\frac{1}{\rho} grad\ p^k(u(x,\xi;t,\tau)) \\ div(u^k) = 0; \end{cases}, \qquad \text{(B-1)}$$

where x, ξ designate spatial coordinates and t, τ are time variables associated with Stokeslets and collocation points respectively (Figure B-1). u^k and p^k represent velocity and pressure components and ρ is a fluid density. u^k and p^k are taken such that $u^k, p^k \to 0$ as $x \to \infty$, k denotes a dimension index of the spatial coordinate.

Tsai, Young, Fan and Chen have presented unsteady Stokeslets for both 2-D and 3-D cases in [2]. They, however, only represent unsteady parts of unsteady Stokes and continuity equations solutions (or the case of steady-state component identically equal to zero).

The analysis of (B-1) shows that a complete fundamental solution to this system of equations is constituted from:

1) unsteady solution - fundamental solution of diffusion equation;
2) steady-state solution of Laplace equation, which represents a limit the solution tends to.

After Fourier transform, representing pressure gradient in a pressure driven flow with delta functions, governing equations (B-1) can be written as follows:

$$\begin{cases} i\frac{\partial}{\partial t}\tilde{u}^k + \mu\alpha^2\tilde{u}^k = [\delta(x_k - \xi_k)\cdot\delta(t-\tau) + \delta(x_k - \xi_k)] \\ i\alpha_j\tilde{u}^k = 0; \end{cases} \tag{B-1a}$$

where α and α_j designate spatial components of Stokeslet strength.

A complete solution for the velocity also satisfies continuity equation. The general and complete solutions of (B-1) can then be written in the form:

$$\Phi_{complete}(x,\xi;t,\tau) = \Phi_H(x,\xi;t,\tau) + \Phi_P(x,\xi;t,\tau) + \Phi_{SS}(x,\xi), \tag{B-2}$$

where $\Phi_H(x,\xi;t,\tau)$ is a homogeneous solution and $\Phi_P(x,\xi;t,\tau)$ are particular unsteady solutions of the equations (B-1) without RHS and $\Phi_{SS}(x,\xi)$ is a solution to a steady-state Stokes equations and $H(t-\tau)$ is a Heaviside step function. One can easily prove that by removing time derivative from unsteady Stokes equation (time derivative of steady-state Stokes equation is identically zero), the steady-state solution component is:

$$\begin{gathered} \Phi_{SS}(x,\xi) = u_j^k(x,\xi) = -\frac{1}{8\pi\nu}\left[\frac{\delta_j^k}{|x-\xi|} + \frac{(x_j-\xi_j)(x_k-\xi_k)}{|x-\xi|^3}\right], \\ and \\ p_j^k(x,\xi) = -\frac{x_k-\xi_k}{4\pi|x-\xi|^3}, \end{gathered} \tag{B-3}$$

Applying Fourier $\mathcal{F}_x$ transform to the unsteady Stokes equation, one obtains:

$$\mathcal{F}_x\left[\frac{\partial u^k}{\partial t}\right] - \nu\mathcal{F}_x[\Delta u^k] = \mathcal{F}_x[\delta(x-\xi)\cdot\delta(t-\tau)], \tag{B-4}$$

$$u^k(x,\xi) = \frac{1}{(4\pi)^{\frac{3}{2}}}\int_{-\infty}^{\infty}\tilde{u}^k\left(\tilde{x},\tilde{\xi}\right)d|\tilde{x}-\tilde{\xi}|;$$

$\tilde{u}^k(t,\tau) = \theta(\tau)e^{-\nu\tilde{t}}$ is a fundamental solution of diffusion-type operator $L(D) = \frac{\partial}{\partial t} - \nu\Delta$. Applying Fourier transform operator to the function $u^k(x,\xi,t,\tau)$,

$$u^k(x,\xi;t,\tau) = -\nu\frac{1}{(4\pi)^{\frac{3}{2}}}\int_0^{(t-\tau)}\int_0^{|x-\xi|}\theta(\tau)e^{-\nu\tilde{t}}\tilde{u}^k(x,\xi)d|\tilde{x}-\tilde{\xi}|d(\tilde{t}-\tilde{\tau})\,. \quad \text{(B-5)}$$

Setting $\theta(\tilde{\tau}) = e^{\nu\tilde{\tau}}$, the homogeneous solution by definition:

$$\widetilde{\Phi}_H(x,\xi;t,\tau) = \tilde{u}^k(x,\xi;t,\tau) = \frac{e^{-\frac{|\tilde{x}-\tilde{\xi}|^2}{4\nu(\tilde{t}-\tilde{\tau})}}}{(4\pi\nu(\tilde{t}-\tilde{\tau}))^{\frac{3}{2}}}, \quad \text{(B-6)}$$

In [4] (§4, p.94) Ladyzhenskaya used fundamental singular solutions of Laplace and heat equation to obtain expression of the velocity Laplacian:

$$\Delta u_0^k(x,\xi;t,\tau) = -\frac{1}{(4\pi\nu(t-\tau))^{\frac{3}{2}}}e^{-\frac{|x-\xi|^2}{4\nu(t-\tau)}}\mathrm{e}^k, \quad \text{(B-7)}$$

where e^k is a respective unity-vector defining the basis of coordinate system.

Taking Cauchy integral of Laplacian over the surface Ω [3] and changing variables, one obtains the expression for the unsteady solution:

$$\begin{aligned} u_0^k(x,\xi,t,\tau) &= \frac{1}{4\pi(4\pi\nu(\tilde{t}-\tilde{\tau}))^{\frac{3}{2}}}\int_\Omega \frac{1}{|\tilde{x}-\tilde{\psi}|}e^{-\frac{|\tilde{\psi}-\tilde{\xi}|^2}{4\nu(\tilde{t}-\tilde{\tau})}}d\psi\cdot\mathrm{e}^k = \\ &= \frac{1}{4\pi^{\frac{3}{2}}\sqrt{\nu(\tilde{t}-\tilde{\tau})}|\tilde{x}-\tilde{\xi}|}\int_0^{|\tilde{x}-\tilde{\xi}|}e^{-\frac{|r|^2}{4\nu(t-\tau)}}dr\cdot\mathrm{e}^k \end{aligned} \quad \text{(B-8)}$$

One may now introduce a new variable: $\eta = \frac{|x-\xi|}{2\sqrt{\nu(t-\tau)}}$,

The derivative of error function yields:

$$\frac{d}{d\eta}\operatorname{erf}(\eta) = \frac{2}{\sqrt{\pi}} e^{-\eta^2}, \tag{B-9}$$

Moving square root in the denominator under the derivative in the integrand:

$$\Phi_P(x,\xi;t,\tau) = u_0^k(x,\xi,t,\tau) = \frac{1}{2\pi^{\frac{3}{2}}|\tilde{x}-\tilde{\xi}|}\int_0^{|\tilde{x}-\tilde{\xi}|} e^{-\frac{|r|^2}{4\nu(\tilde{t}-\tilde{\tau})}} d\frac{r}{2\sqrt{\nu(\tilde{t}-\tilde{\tau})}} \cdot \mathrm{e}^k =$$

$$= \frac{\operatorname{erf}\left(\frac{|x-\xi|}{2\sqrt{\nu(t-\tau)}}\right)}{4\pi|x-\xi|} \cdot \mathrm{e}^k \tag{B-10}$$

The expression above represents kernel of the unsteady part of the diffusion-type equation solution. The general solution for the Stokes equation includes unsteady diffusion equation and continuity equations, together with the steady state part:

$$L(D)[u_0(x,\xi;t,\tau) + u(x,\xi)\cdot H(t-\tau)] =$$

$$= L(D)u(x,\xi)\cdot H(t-\tau) + L(D)u_0(x,\xi,t,\tau) = 0; \tag{B-11}$$

Introducing diffusion operator 3-D system of Stokes equations. That is using (B-10) it is possible to write down time derivative:

$$\frac{\partial}{\partial t}u^k(x,\xi,t,\tau) = \frac{\partial}{\partial t}\left[\frac{1}{(4\pi\nu(t-\tau))^{\frac{3}{2}}} e^{-\frac{|x-\xi|^2}{4\nu(t-\tau)}}\right] =$$

$$-\frac{3}{(4\pi\nu(t-\tau))^{\frac{3}{2}}\cdot 2(t-\tau)} e^{-\frac{|x-\xi|^2}{4\nu(t-\tau)}} + \frac{|x-\xi|^2}{4\nu(t-\tau)^2}\frac{1}{(4\pi\nu(t-\tau))^{\frac{3}{2}}} e^{-\frac{|x-\xi|^2}{4\nu(t-\tau)}} =$$

$$-\frac{3}{(4\pi\nu(t-\tau))^{\frac{3}{2}}\cdot 2(t-\tau)} e^{-\frac{|x-\xi|^2}{4\nu(t-\tau)}} + \frac{|x-\xi|^2}{4\nu(t-\tau)^2}\frac{1}{(4\pi\nu(t-\tau))^{\frac{3}{2}}} e^{-\frac{|x-\xi|^2}{4\nu(t-\tau)}} = -\frac{3}{2(t-\tau)}u^k(x,\xi,t,\tau) +$$

$$\frac{|x-\xi|^2}{4\nu(t-\tau)^2}u^k(x,\xi,t,\tau) = \left[\frac{|x-\xi|^2}{4\nu(t-\tau)^2} - \frac{3}{2(t-\tau)}\right]u^k(x,\xi,t,\tau) \tag{B-12}$$

and Laplacian:

$$\frac{\partial^2}{\partial^2 x_k}u^k(x,\xi,t,\tau)=\frac{\partial^2}{\partial^2 x_k}\left[\frac{1}{\left(4\pi\nu(t-\tau)\right)^{\frac{3}{2}}}e^{-\frac{|x-\xi|^2}{4\nu(t-\tau)}}\right]=\frac{\partial}{\partial x_i}\left[\frac{-2|x_k-\xi_k|}{4\nu(t-\tau)\cdot\left(4\pi\nu(t-\tau)\right)^{\frac{3}{2}}}e^{-\frac{|x-\xi|^2}{4\nu(t-\tau)}}\right]=$$

$$\left[-\frac{2}{4\nu(t-\tau)\cdot\left(4\pi\nu(t-\tau)\right)^{\frac{3}{2}}}+\frac{2|x_k-\xi_k|\cdot 2|x_k-\xi_k||x-\xi|}{16\nu^2(t-\tau)^2\cdot\left(4\pi\nu(t-\tau)\right)^{\frac{3}{2}}}\right]e^{-\frac{|x-\xi|^2}{4\nu(t-\tau)}}=$$

$$\left[\frac{|x_k-\xi_k|^2}{4\nu^2(t-\tau)^2}-\frac{1}{2\nu(t-\tau)}\right]\frac{1}{\left(4\pi\nu(t-\tau)\right)^{\frac{3}{2}}}e^{-\frac{|x-\xi|^2}{4\nu(t-\tau)}}=\left[\frac{|x_k-\xi_k|^2}{4\nu^2(t-\tau)^2}-\frac{1}{2\nu(t-\tau)}\right]u^k(x,\xi,t,\tau) \qquad \text{(B-13)}$$

$$\Delta u^k=\frac{\partial^2 u^1}{\partial x_1^2}+\frac{\partial^2 u^2}{\partial x_2^2}+\frac{\partial^2 u^3}{\partial x_3^2}=\left(\frac{(x-\xi)_1^2}{4\nu^2(t-\tau)^2}-\frac{1}{2\nu(t-\tau)}\right)u^1+\left(\frac{(x-\xi)_2^2}{4\nu^2(t-\tau)^2}-\frac{1}{2\nu(t-\tau)}\right)u^2+$$

$$+\left(\frac{(x-\xi)_3^2}{4\nu^2(t-\tau)^2}-\frac{1}{2\nu(t-\tau)}\right)u^3, \qquad \text{(B-14)}$$

where

$$(x_1-\xi_1)^2+(x_2-\xi_2)^2+(x_3-\xi_3)^2=|x-\xi|^2=|r|^2, u^k=\{u^1,u^2,u^3\} \qquad \text{(B-15)}$$

Summing up (B-13) and (B-14) to obtain Laplacian, one ends up with:

$$\Delta u=\left(\frac{|x-\xi|^2}{4\nu(t-\tau)^2}-\frac{3}{2(t-\tau)}\right)u \qquad \text{(B-16)}$$

and therefore:

$$\frac{\partial u}{\partial t}-\nu\Delta u=\left(\frac{|x-\xi|^2}{4\nu(t-\tau)^2}-\frac{3}{2(t-\tau)}\right)u-\left(\frac{|x-\xi|^2}{4\nu(t-\tau)^2}-\frac{3}{2(t-\tau)}\right)u=0, \qquad \text{(B-17)}$$

which proves that $u^k(x,\xi;t,\tau)$ satisfies diffusion equation and gives identical zero.

Using the same principle, one may obtain the derivatives of the unsteady solution u_0 using kernel (B-10) of the equation with the RHS representing product of delta functions of time and space.

Taking time and partial derivatives of the error function, it is possible to apply chain rule to (B-9), which yields:

$$\frac{\partial}{\partial|x-\xi|}F\big(\eta(x,\xi;t,\tau)\big)=\frac{\partial F(\eta)}{\partial\eta}\frac{\partial\eta(x,\xi;t,\tau)}{\partial|x-\xi|}, \tag{B-18}$$

$$\frac{\partial}{\partial t}u_0(x,\xi;t,\tau)=\frac{\partial}{\partial t}\frac{erf\left(\frac{|x-\xi|}{2\sqrt{\nu(t-\tau)}}\right)}{4\pi|x-\xi|}=-\frac{1}{4\pi|x-\xi|}\frac{|x-\xi|}{2\sqrt{\nu(t-\tau)}\cdot 2(t-\tau)}e^{-\frac{|x-\xi|^2}{4\nu(t-\tau)}}\frac{2}{\sqrt{\pi}}=$$

$$=-\frac{1}{\nu^{\frac{1}{2}}\big(4\pi(t-\tau)\big)^{\frac{3}{2}}}e^{-\frac{|x-\xi|^2}{4\nu(t-\tau)}}, \tag{B-19}$$

$$\frac{\partial^2}{\partial x_k^2}u_0^k(x,\xi;t,\tau)=\frac{\partial^2}{\partial x_k^2}\frac{erf\left(\frac{|x-\xi|}{2\sqrt{\nu(t-\tau)}}\right)}{4\pi|x-\xi|}=$$

$$\frac{\partial}{\partial x_k}\left[-\frac{|x_k-\xi_k|}{4\pi|x-\xi|^3}erf\left(\frac{|x-\xi|}{2\sqrt{\nu(t-\tau)}}\right)+\frac{|x_k-\xi_k|}{4\pi|x-\xi|^2}\frac{1}{2\sqrt{\nu(t-\tau)}}\frac{2}{\sqrt{\pi}}e^{-\frac{|x-\xi|^2}{4\nu(t-\tau)}}\right]=$$

$$-\frac{1}{4\pi|x-\xi|^3}erf\left(\frac{|x-\xi|}{2\sqrt{\nu(t-\tau)}}\right)++\frac{3|x_k-\xi_k||x_k-\xi_k|}{4\pi|x-\xi|^5}erf\left(\frac{|x-\xi|}{2\sqrt{\nu(t-\tau)}}\right)-\frac{|x_k-\xi_k||x_k-\xi_k|e^{-\frac{|x-\xi|^2}{4\nu(t-\tau)}}}{4\pi|x-\xi|^4\cdot 2\sqrt{\nu\pi(t-\tau)}}+$$

$$\frac{1}{4\pi|x-\xi|^2\sqrt{\pi\nu(t-\tau)}}e^{-\frac{|x-\xi|^2}{4\nu(t-\tau)}}-\frac{2|x_k-\xi_k||x_k-\xi_k|e^{-\frac{|x-\xi|^2}{4\nu(t-\tau)}}}{4\pi|x-\xi|^4\sqrt{\nu\pi(t-\tau)}}-\frac{2|x_k-\xi_k||x_k-\xi_k|e^{-\frac{|x-\xi|^2}{4\nu(t-\tau)}}}{4\pi|x-\xi|^2\sqrt{\nu\pi(t-\tau)}\,4\pi(t-\tau)}. \tag{B-20}$$

In order to derive components of the resulting fundamental solution matrix, Kroneker delta definition is helpful:

$$x_j=x_k\delta_j^k, \tag{B-21}$$

Combining terms in (B-20), multiplying by Kroneker delta and applying (B-21):

$$\frac{\partial^2}{\partial x_j^2} U_0^k(x,\xi;t,\tau) =$$

$$\frac{\delta_j^k - 3|x_j-\xi_j||x_k-\xi_k|}{4\pi|x-\xi|^3} erf\left(\frac{|x-\xi|}{2\sqrt{\nu(t-\tau)}}\right) + \frac{e^{-\frac{|x-\xi|^2}{4\nu(t-\tau)}}}{4\pi\sqrt{\pi}|x-\xi|^2\sqrt{\nu(t-\tau)}} - \frac{3|x_j-\xi_j||x_k-\xi_k|e^{-\frac{|x-\xi|^2}{4\nu(t-\tau)}}}{4\pi\sqrt{\pi}|x-\xi|^4\cdot 2\sqrt{\nu(t-\tau)}} -$$

$$- \frac{|x_j-\xi_j||x_k-\xi_k|e^{-\frac{|x-\xi|^2}{4\nu(t-\tau)}}}{8(\pi\nu(t-\tau))^{\frac{3}{2}}|x-\xi|^2} = \frac{|x-\xi|^2 - 3|x_j-\xi_j||x_k-\xi_k|}{4\pi|x-\xi|^3} erf\left(\frac{|x-\xi|}{2\sqrt{\nu(t-\tau)}}\right) +$$

$$+ \frac{2\nu(t-\tau)(|x-\xi|^2 - 3|x_j-\xi_j||x_k-\xi_k|) - |x_k-\xi_k||x_k-\xi_k||x-\xi|^2}{8(\pi\nu(t-\tau))^{\frac{3}{2}}|x-\xi|^4} e^{-\frac{|x-\xi|^2}{4\nu(t-\tau)}} \qquad \text{(B-22)}$$

Finally, evaluating $\left(-\frac{1}{\nu}\frac{\partial}{\partial t} + \Delta\right) U_0^k(x,\xi;t,\tau)$ diffusion-type operator:

$$\frac{\delta_j^k}{(4\pi\nu(t-\tau))^{\frac{3}{2}}} e^{-\frac{|x-\xi|^2}{4\nu(t-\tau)}} - \frac{\delta_j^k|x-\xi|^2 - 3|x_j-\xi_j||x_k-\xi_k|}{4\pi|x-\xi|^3} erf\left(\frac{|x-\xi|}{2\sqrt{\nu(t-\tau)}}\right) +$$

$$\frac{2\nu(t-\tau)(|x-\xi|^2\delta_j^k - 3|x_j-\xi_j||x_k-\xi_k|) - |x_j-\xi_j||x_k-\xi_k||x-\xi|^2}{8(\pi\nu(t-\tau))^{\frac{3}{2}}|x-\xi|^4} e^{-\frac{|x-\xi|^2}{4\nu(t-\tau)}} =$$

$$- \frac{|x-\xi|^2\delta_j^k - 3|x_j-\xi_j||x_k-\xi_k|}{4\pi|x-\xi|^3} erf\left(\frac{|x-\xi|}{2\sqrt{\nu(t-\tau)}}\right) +$$

$$\frac{2\nu(t-\tau)(|x-\xi|^2\delta_j^k - 3|x_j-\xi_j||x_k-\xi_k|) - |x_j-\xi_j||x_k-\xi_k||x-\xi|^2 + |x-\xi|^4\delta_j^k}{8(\pi\nu(t-\tau))^{\frac{3}{2}}|x-\xi|^4} e^{-\frac{|x-\xi|^2}{4\nu(t-\tau)}}; \qquad \text{(B-23)}$$

or substituting $(x_k - \xi_k)$ with x_k, $(x_j - \xi_j)$ with x_j, $x - \xi$ with r and $(t - \tau)$ with t, it is possible to obtain simplified form of unsteady solution in the matrix form described in [2]:

$$\left(-\frac{1}{\nu}\frac{\partial}{\partial t} + \Delta\right) U_0^k(x;t) = \frac{2\nu t(r^2\delta_j^k - 3x_j x_k) - x_j x_k r^2 + r^4\delta_j^k}{8(\pi\nu t)^{\frac{3}{2}} r^4} e^{-\frac{r^2}{4\nu t}} -$$

$$-\frac{r^2\delta_j^k-3x_jx_k}{4\pi r^3}erf\left(\frac{r}{2\sqrt{\nu t}}\right) \tag{B-24}$$

Accounting for Kroneker delta factor and applying j and k indices, matrix structure looks as follows:

$$\begin{Bmatrix} u^* \\ v^* \\ w^* \\ p^* \end{Bmatrix} = \frac{1}{4\pi\rho}\begin{bmatrix} B_{11} & B_{12} & B_{13} \\ B_{21} & B_{22} & B_{23} \\ B_{31} & B_{32} & B_{33} \\ B_{41} & B_{42} & B_{43} \end{bmatrix}\begin{Bmatrix} \mathrm{e}^1 \\ \mathrm{e}^2 \\ \mathrm{e}^3 \end{Bmatrix}, \tag{B-25}$$

where:

$$\begin{gathered} B_{11} = \frac{e^{-\frac{|r|^2}{4\nu t}}}{2\sqrt{\pi}(t\nu)^{\frac{3}{2}}r^4}(6\nu t + r^2)(r^2 - x_1^2) - 4\nu t r^2) - \frac{(r^2-3x_1^2)erf\left(\frac{r}{2\sqrt{\nu t}}\right)}{r^5} \\ B_{22} = \frac{e^{-\frac{|r|^2}{4\nu t}}}{2\sqrt{\pi}(t\nu)^{\frac{3}{2}}r^4}(6\nu t + r^2)(r^2 - x_2^2) - 4\nu t r^2) - \frac{(r^2-3x_2^2)erf\left(\frac{r}{2\sqrt{\nu t}}\right)}{r^5} \\ B_{33} = \frac{e^{-\frac{|r|^2}{4\nu t}}}{2\sqrt{\pi}(t\nu)^{\frac{3}{2}}r^4}(6\nu t + r^2)(r^2 - x_3^2) - 4\nu t r^2) - \frac{(r^2-3x_3^2)erf\left(\frac{r}{2\sqrt{\nu t}}\right)}{r^5} \\ B_{12} = B_{21} = -\frac{e^{-\frac{|r|^2}{4\nu t}}}{2\sqrt{\pi}(t\nu)^{\frac{3}{2}}r^4}x_1x_2(6\nu t + r^2) + \frac{(3x_1x_2)erf\left(\frac{r}{2\sqrt{\nu t}}\right)}{r^5} \\ B_{13} = B_{31} = -\frac{e^{-\frac{|r|^2}{4\nu t}}}{2\sqrt{\pi}(t\nu)^{\frac{3}{2}}r^4}x_1x_3(6\nu t + r^2) + \frac{(3x_1x_3)erf\left(\frac{r}{2\sqrt{\nu t}}\right)}{r^5} \\ B_{23} = B_{32} = -\frac{e^{-\frac{|r|^2}{4\nu t}}}{2\sqrt{\pi}(t\nu)^{\frac{3}{2}}r^4}x_2x_3(6\nu t + r^2) + \frac{(3x_2x_3)erf\left(\frac{r}{2\sqrt{\nu t}}\right)}{r^5} \\ B_{41} = \rho\frac{x_1}{r^3}\delta(t) \\ B_{42} = \rho\frac{x_2}{r^3}\delta(t) \\ B_{43} = \rho\frac{x_3}{r^3}\delta(t) \end{gathered} \tag{B-26}$$

and ρ is a fluid density.

Applying elementary matrix multiplication of (B-26) and writing the resulting unsteady fundamental solution in matrix form:

$$u_u(r,t) = \frac{1}{4\pi\rho}\left[\left(\frac{e^{-\frac{|r|^2}{4\nu t}}}{2\sqrt{\pi\nu t}|r|^2} - \frac{erf\left(\frac{r}{2\sqrt{\nu t}}\right)}{|r|^3}\right)\left(I - 3\frac{r\otimes r}{|r|^2}\right) + \frac{e^{-\frac{|r|^2}{4\nu t}}}{2\pi^{\frac{1}{2}}(\nu t)^{\frac{3}{2}}}\left(I - \frac{r\otimes r}{|r|^2}\right)\right] \tag{B-27}$$

$$p_u(r,t) = \frac{r}{4\pi|r|^3}\delta(t)$$

The steady-state solution in 3-D notation has been presented in Chapter III (2-2).

Finally, coming back to a complete solution form (B-2) and putting both unsteady (B-27) and steady-state (B-3) solutions together, it becomes possible to write a complete velocity Stokeslet solution as:

$$u_c(r,t) = \frac{1}{4\pi\rho}\left[\left(\frac{e^{-\frac{|r|^2}{4\nu t}}}{2\sqrt{\pi\nu t}|r|^2} - \frac{erf\left(\frac{r}{2\sqrt{\nu t}}\right)}{|r|^3}\right)\left(I - 3\frac{r\otimes r}{|r|^2}\right) + \frac{e^{-\frac{|r|^2}{4\nu t}}}{2\pi^{\frac{1}{2}}(\nu t)^{\frac{3}{2}}}\left(I - \frac{r\otimes r}{|r|^2}\right) + \frac{1}{2\nu}\left(\frac{I}{|r|} + \frac{r\otimes r}{|r|^3}\right)\right]$$

$$p_c(r,t) = \frac{r}{4\pi|r|^3}(\delta(\nu t) - 1); \tag{B-28}$$

B-3 Uniqueness of the complete unsteady solution

In order to prove the uniqueness of the proposed complete unsteady solution, we can do Dirichlet proof for the unsteady Stokes equations. Assume we have two solutions to (B-1) with specified Cauchy and Dirichlet data. Then the following conditions are true:

$$\begin{cases} w_t - \nu w_{rr} = -\frac{1}{\rho}\text{grad}q, (t,r) \in [0,R] \times [0,\infty], \\ w(0,t) = 0, w(R,t) = 0\ x \in [0,R], \\ w(r,0) = 0, w(r,\infty) = 0, t \in [0,\infty]. \end{cases} \tag{B-29}$$

here $w(r,t)$ and $q(r,t)$ will designate the difference between complete and unsteady solutions of the unsteady Stokes equations: $w_1(r,t) = u_c(r,t) - u_u(r,t)$ and $q_1(r,t) = p_c(r,t) - p_u(r,t)$ (from B-27 and B-28). Then:

$$\begin{cases} w_1(r) = \frac{1}{8\pi\nu\rho}\left(\frac{I}{|r|} + \frac{r \otimes r}{|r|^3}\right), \\ q_1(r) = \frac{r}{4\pi|r|^3} \end{cases} \tag{B-30}$$

It is important now to show that $w(r,t) = 0$ at $(r,t) \in [0,R] \times [0,\infty]$. Multiplying both sided of the first equation in (B-29) and integrating them r on $[0,R]$, we obtain:

$$\int_{[0,R]} w w_t dr - \nu \int_{[0,R]} w w_{rr} dr = -\frac{1}{\rho}\int_{[0,R]} w grad(q) dr \tag{B-31}$$

For the first integral in (B-31) we have:

$$\int_{[0,R]} w w_t dr = \frac{1}{2}\frac{d}{dt}\int_{[0,R]} w^2 dr \tag{B-32}$$

The second integral can be expressed in the following way applying integration by parts:

$$-\int_{[0,R]} w w_{rr} dr = -w w_r|_{r=0}^{r=R} + \int_{[0,R]} w_r^2 dr \tag{B-33}$$

Combining all terms and substituting them into the first condition in (B-29):

$$\frac{1}{2}\frac{d}{dt}\int_{[0,R]} w^2 dr + \nu \int_{[0,R]} w_r^2 dr - \nu w w_r|_{r=0}^{r=R} = -\frac{1}{\rho}\int_{[0,R]} w grad(q) dr, \tag{B-34}$$

Now, it can be noticed that for the specified spatial boundary conditions $w w_r|_{r=0}^{r=R} = 0$.

We end up with the following integral expression to be satisfied according to (B-29):

$$\frac{1}{2}\frac{d}{dt}\int_{[0,R]} w^2 dr + \nu \int_{[0,R]} w_r^2 dr = -\frac{1}{\rho}\int_{[0,R]} w grad(q) dr \tag{B-35}$$

We now have:

$$\frac{1}{2}\frac{d}{dt}\int_{[0,R]} w^2 dr + \nu \int_{[0,R]} w_r^2 dr = -\frac{1}{\rho}\int_{[0,R]} w grad(q) dr, \qquad \text{(B-36)}$$

to be satisfied for the selected boundary conditions. Now introducing $w_r^2 = (ww_r)_r - ww_{rr}$ into the first integral of (B-36) yields:

$$\frac{1}{2}\frac{d}{dt}\int_{[0,R]} w^2 dr + \int_{[0,R]}[(ww_r)_r - ww_{rr}]dr = -\frac{1}{\mu}\int_{[0,R]} w grad(q) dr, \qquad \text{(B-37)}$$

or moving $\frac{1}{2}\frac{d}{dt}\int_{[0,R]} w^2 dr - ww_{rr}$ to the right-hand side (RHS) of (B-37) yileds:

$$\int_{[0,R]}(ww_r)_r dr = -\int_{[0,R]} w\left[\frac{d}{dt}w - w_{rr} + \frac{1}{\mu} grad(q)\right] dr \qquad \text{(B-38)}$$

It is now easy to notice that the factor $\left[\frac{d}{dt}w - w_{rr} + \frac{1}{\mu} grad(q)\right]$ of the integrand in the RHS is equal to zero, since it represents the initial governing unsteady Stokes equation in (B-1). Therefore:

$$\int_{[0,R]}(ww_r)_r dr = 0,$$

$$ww_r|_{r=0}^{r=R} = C, \qquad \text{(B-39)}$$

Finally, from (B-34) it was already shown that $ww_r|_{r=0}^{r=R} = 0$. Then $C = 0$, $w(r,t) = 0$ and this proves the uniqueness of the proposed complete solution under arbitrary Dirichlet boundary conditions.

B-3 Validation of 3-D unsteady complete Stokeslet for a Stokes flow over flat plate

The simplest problem with analytical solution available to validate BSM solution of unsteady Stokes flow problem is a viscous flow over the flat plate, also known as Stokes first problem [100].

The resulting solution of the 2-D Stokes flow problem in the semi-infinite domain about stationary infinitely long flat plate with the following boundary conditions:

1) no-slip ($u_x|_{y=0} = 0$),
2) no-penetrating ($u_y\big|_{y=0} = 0$),

and the impulse strength is unity at the moment of time $t = 0$,

where u_x and u_y are horizontal and vertical velocity vector components; $|t - \tau|$ is the time moment defined with the t and τ time coordinates associated with the collocation points and Stokeslets respectively.

After $t = 0$ the flow is assumed to be self-propagating until it reached steady-state flow, which yields $U|_{r=\infty} = const = 1$ for continuously moving plate.

The analytical velocity solution presented in Figure B-2 is as follows:

$$U(z) = U_\infty \left(1 - \text{erfc}\left(\frac{|z-z_0|}{2\sqrt{\nu t}}\right)\right) = U_\infty \,\text{erf}\left(\frac{|z-z_0|}{2\sqrt{\nu t}}\right), \tag{B-40}$$

where $|z - z_0|$ designate vertical distance from the plate.

The flow field and velocity magnitude obtained with BSM though the complete solution of 3-D Stokes equations (B-29) for a flow past a long parallelepiped, was

compared to the 2-D Stokes first problem solution. The resulting velocity vector filed and distribution obtained with BSM was taken in the section plane passing through the middle of parallelepiped.

The initial far-field velocity was taken $U_\infty = 1$. Stokeslet spatial allocation depth was $\overline{D} = 0.02 \div 0.05$, while time allocation lag following [48] was equal to $|t - \tau| = \frac{\Delta x^2}{\nu}$.

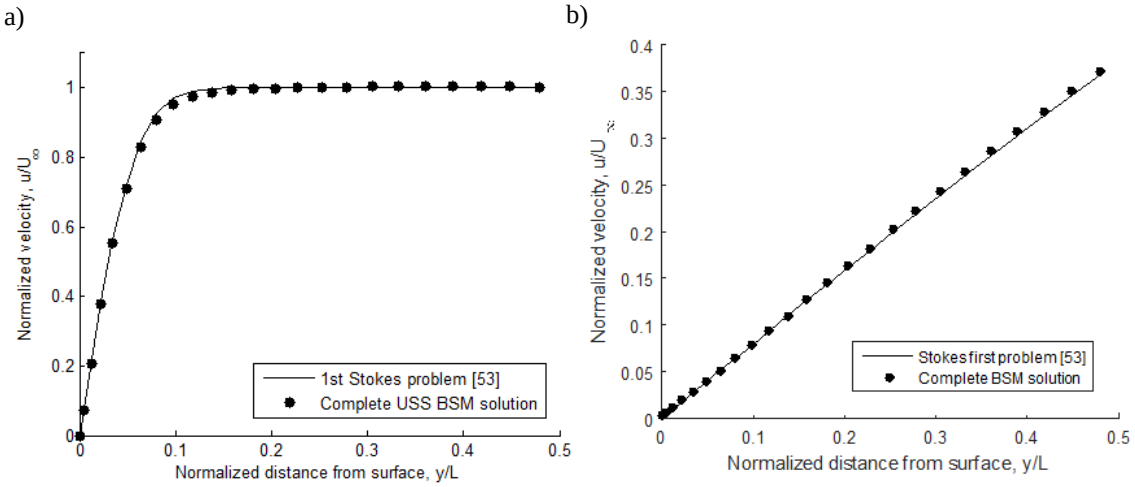

Figure B-2 Velocity magnitude distribution versus distance from the plate surface at: a) $t = 0.02s, \nu = 0.1\frac{m^2}{s}$; b) $t = 1s, \nu = 0.5\frac{m^2}{s}$.

Comparing Stokes first problem solution (B-40) and proposed full (unsteady plus steady-state) Stokes flow problem solution (B-28) presented in Figures B-2 and B-3, one may observe good correspondence of both velocity profiles and magnitude over the time.

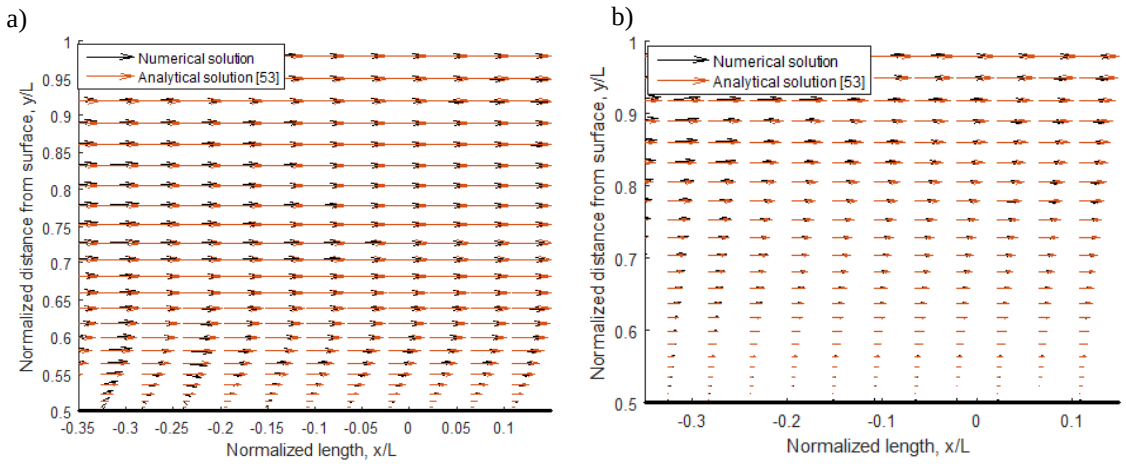

Figure B-3 Velocity vector field over the plate. Complete solution as per (B-28) at: a) $t = 0.02s, \nu = 0.1\frac{m^2}{s}$; b) $t = 1s, \nu = 0.5\frac{m^2}{s}$.

The complete solution (B-28) for unsteady Stokes equation in the form (B-29) converges to the steady-state solution together with the sum of Stokeslets converging to the steady-state Stokes force. This topic is interesting for further application to unsteady multiphase microfluidic problems, unsteady particulate flow in microscale filtration systems and problems of viscoelastic surface deformation in Stokes flow to name a few.

APPENDIX C

NOMENCLATURE

$\mathrm{A}-$ view area

$\mathrm{A}_{\mathrm{mid}_{\parallel}}, \mathrm{A}_{\mathrm{mid}_{\perp}} =$ middle section of non-spherical body: longitudinal, transversal orientation

$\mathrm{A}_{\mathrm{mid}_{\perp}} =$ middle section of transversally oriented non-spherical body

$a =$ Stokeslet allocation radius

$\overrightarrow{a_i} =$ i-th component of collocation point location radius-vector

$C_D =$ total drag coefficient

$c, d =$ Cassinian shape parameters

$D =$ Stokeslet allocation depth

$\overline{D} =$ Stokeslet allocation depth near inflexion points and in concave regions

$d_i = \{h, h_1, h_1', h_2, h_2', l_1, l_2, t_0, t_1\} =$ uncertainty spatial and time contributing parameters

$e =$ modified Cassinian shape factor

$\mathrm{e}^{\mathrm{k}} =$ unit direction vector in 2-D or 3-D Cartesian coordinate basis

$\vec{F} =$ Stokeslet vector = $\left(F^{(1)}, F^{(2)}, F^{(3)}\right)^T$ in 3-D space or $\left(F^{(1)}, F^{(2)}\right)^T$ in 2-D space

$F_i^{(k)} =$ i-th Stokeslet strength

$F_{\mathrm{SC}} =$ Stokes force about cylindrical fiber

$F_{SS} =$ Stokes force about spherical droplet or pair of merging droplets

$F_{shear} =$ shear force

$F_{normal} =$ normal force

F_{Σ} = Sum of total drag (Stokes force) about two merging particles/droplets

$F_{2spheres}$ = total drag (Stokes force) about two spheres contacting at a single point

F_{Stokes} = Stokes force = total loaded fiber drag

f_+, f_- = Cassinian stretching coefficient for positive and negative abscissa direction

G_{ij} = first fundamental form tensor component

h = depth of view at the droplet-fiber system

h_1, h_1' = droplet/track initial height - calculated and parallax reading values

h_2, h_2' = droplet/track height after deformation- calculated and parallax reading values

L – distance between centers of two spherical particles

l_1 = distance from camera to an observation plane crossing droplet/track surface

l_2 = distance from observation plane to the scale

Δl = local droplet elongation after Δt.

M = Stokeslet computational matrix of size 3N × 3N in 3-D space, 2N × 2N in 2-D space

N = number of Stokeslets = number of collocation points

n = number of space dimensions

p = pressure

p_ϵ = pressure regularized solution

q = difference of pressure fundamental solutions of the unsteady Stokes equation

$R = R_{droplet}$ = radius of spherical particle or droplet

$R_i = r_i$ = flow field point location radius

R_{SC} = radius of Stokeslet allocation for a cylinder

R_{SS} = radius of Stokeslet allocation for a sphere

Re_D = Reynolds number based on characteristic dimension

$Re =$ Reynolds number based on radius

$r =$ radius-vector in polar, cylindrical or spherical coordinates

$\widetilde{r_{ij}}^{k} =$ k-th component of normalized radius-vector between i-th Stokeslet and j-th collocation point = $\vec{r_j} - \vec{a_i}$

$\vec{r_j} =$ j-th component of Stokeslet location radius-vector

$\left|\widetilde{r_{ij}}\right| =$distance between i-th Stokeslet and j-th collocation point = $\sqrt{\sum_{k=1}^{n}\left(\widetilde{r_{ij}}^{k}\right)^2}$

$S_{body} =$ surface area of a non-spherical body

$S_i =$ elementary surface area

$s_{sph} =$ sphere surface area

$t =$ time

$t_0, t_1 =$ time reading before and after droplet/track deformation experiment

$\Delta t =$ time step

$T =$ temperature

$U =$ velocity solution vector = $\left(U^{(1)}, U^{(2)}, U^{(3)}\right)^T$ in 3-D or $\left(U^{(1)}, U^{(2)}\right)^T$ in 2-D space

$U_\infty =$ particle velocity or free stream velocity

$\vec{u} =$ velocity vector

$u_j^{(k)} = u_{kj} =$ j-th velocity component

$u_{\epsilon_j}^{(k)} =$ j-th regularized solution velocity component

$u_r, u_\theta, u_\varphi =$ radial, polar and azimuthal velocity components in spherical coordinates

$u_{r_i} =$ horizontal velocity in the point at distance r_i away from a surface in 2-D

$V_p =$ volume of a single droplet

$v_{r_i} =$ vertical velocity in the point at distance r_i away from a surface in 2-D

$w =$ difference of velocity fundamental solutions of the unsteady Stokes equation

x_j^{old}, x_j^{new} = old and new coordinate of deformable viscous surface

α = volume fraction (Chapter III); Fourier transform of spatial coordinate (Appendix B)

α_t = Fourier transform of time coordinate (Appendix B)

β = inlet channel direction angle

Γ, Γ_S = Stokeslet and collocation points surfaces

γ_f = surface tension coefficient

$\dot{\gamma}$ = shear rate

$\delta = \delta_j^k$ = delta-Dirac function

$\epsilon -$ regularization parameter

$\varepsilon, \varepsilon', \varepsilon_{d_i}, \varepsilon_\Sigma$ = uncertainties (Appendix C)

θ, φ = polar and azimuthal angles in spherical coordinates

κ_i = local surface curvature

λ = differentiation coefficient

μ = dynamic viscosity

ν = kinematic viscosity

ξ_i = Stokeslet spatial coordinate

ρ = density

$\sigma -$ surface tension

τ = shear stress; time component associated with Stokeslet (Appendix B)

ϕ = sphericity factor

$\Phi_{\mathrm{H}}, \widetilde{\Phi}_{\mathrm{H}}$ = homogeneous solution of unsteady Stokes equation and its' Fourier transform

$\Phi_{\mathrm{P}}, \widetilde{\Phi}_{\mathrm{P}}$ = particular solution of unsteady Stokes equation and its' Fourier transform

Φ_{SS} = steady-state solution of Stokes equation